

LIQUID CRYSTAL MATERIALS AND LIQUID CRYSTAL DISPLAYS

Martin Schadt

ROLIC Ltd., Grenzacherstrasse 124, 4002 Basel Switzerland

KEY WORDS: LPP, FLC, LCD, supertwisted nematic

ABSTRACT

Since the early 1970s, three major prerequisites have brought the success of the liquid crystal display (LCD) technology to its key role of today. Namely, the discovery of electro-optical field-effects on which the displays are based, the successful search for liquid crystals (LCs) with material properties that meet the complex requirements of electro-optical effects and render the effects applicable in displays, and last but not least, the development of the technological tools required for manufacturing displays.

Virtually all of today's commercial LCDs are based on the twisted nematic (TN) or on various supertwisted nematic (STN) effects whose extensive development and improvement over the past 25 years is still rapidly progressing. Those liquid crystal material properties and electro-optical effects that essentially determine the performance of nematic displays are reviewed. Correlations between molecular functional structural groups, LC material properties, and their electro-optical relevance for TN and STN displays are outlined. Included are dual-frequency addressing phenomena in liquid crystal materials, in situ dielectric heating of displays, and conductivity phenomena that are related and that may either hamper or improve the performance of high-information content LCDs. Moreover, we review some recent developments made in our laboratories on novel electro-optical devices and device-specific functional organic materials, e.g. optical alignment of monomeric and polymeric liquid crystals by linearly polarized light; the generation of photo-patterned multidomain twisted nematic displays with broad field of view; the operation of displays with circularly polarized light, as well as compact and bright cholesteric LCD projection optics whose polarizers, filters, and modulators are all based on liquid crystal elements.

INTRODUCTION

To approach the complex and diverse field of liquid crystal displays and liquid crystal materials necessitates an interdisciplinary research approach between physics, chemistry, and display technology. In the early 1970s, we began to investigate, develop, and correlate molecular structures with material properties and electro-optical effects with the aim of finding and developing new electro-optical effects and liquid crystals that would lead to improved displays. Today we are continuing this work, in close collaboration with liquid crystal display manufacturers, at the recently founded interdisciplinary research and development company ROLIC Ltd.

To establish and to improve the increasingly sophisticated interactions between humans and machines requires suitable displays. The displays must be compatible with integrated, low-power consuming electronics. Moreover, they should be flat and of low weight, and they must be capable of rapidly transforming the electronic output signals of a multitude of electronic equipment into high-quality optical images. Because the LCD technology has become the only display technology that is capable of displaying equally well the simple time information of a digital wristwatch and the complex color images of computers and television sets, it has become a key technology.

With the advancement of the LCD technology, spin-offs are created that open up new applications within the field as well as in nondisplay-related areas. Examples of spin-offs are the development of the thin film transistor (TFT) technology, required for addressing high-information content displays; the design of novel, non-centrosymmetrically ordered organic materials for integrated optics devices; the optical generation and patterning of liquid crystal alignment; optically patterned retarders with spatially adjustable orientation of the optical axes for integration into displays; a novel copy-proof imaging technology that has recently become feasible with our linearly photopolymerizable (LPP) technology; and the development of ferroelectric liquid crystal (FLC) displays.

To illustrate the rapid progress and the interdependence of the display and the liquid crystal materials technologies it is interesting to note the simplicity of the first commercial twisted nematic liquid crystal mixture, which was developed in our laboratories in 1971 after the discovery of the twisted nematic (TN) effect (1). The mixture called Ro-TN-200 consists of just two types of molecules (Schiff's bases) with almost identical structures (2). Despite its simplicity, the mixture properties were sufficient to realize the first $3\frac{1}{2}$ digit TN-LCDs for watches, which comprised twenty-four picture elements (pixels) (3). Today's most advanced LC materials, which are used for realizing high-information content, TFT-addressed TN displays, as well as time multiplexed supertwisted displays, frequently consist of more than twenty liquid crystal components with

very different molecular structures. The complexity of modern LC mixtures is a consequence of the many, often contradictory material parameters that have to be designed into the liquid crystal molecules to meet the demanding display performance. Most of the liquid crystals used in high-information content displays have been designed and manufactured only during the past ten years. These modern LC materials combined with the advanced TFT-TN-displays result in color displays with more than one million pixels. This is an increase in the number of pixels by more than a factor of 40,000 since the first $3\frac{1}{2}$ digit, black-and-white TN-LCDs in the early 1970s.

Because every electro-optical effect has limitations, the search for new effects that require new LC materials is an ongoing research and development process. Examples are electro-optical effects that exhibit steeper transmission-voltage characteristics than TN displays, such as those required to realize STN configurations (4–6). Although STN displays compromise field-of-view, response time, and color reproduction, STN-LCDs based on alkenyl liquid crystals with their advanced elastic properties have made STN displays highly multiplexible. This has led to improved contrast and a reduced number of pixel connections, drivers, and costs (7).

The versatility of LCDs allows their use not only as direct-view displays but also as light modulators in large-area projectors. Because state of the art direct-view TFT-TN-displays are costly and have restricted fields of view (single domain TFT-TN-LCDs), they are still restricted in size to about 14-inch diagonal. Thus LCD projectors are crucial to display large-area video images. This can be achieved by front or rear projection and depends on the progress made in producing flat, low weight and bright LCD projector concepts and materials.

The liquid crystal material properties reviewed in the following essentially determine the operability of nematic displays. Examples of some modern liquid crystal structures and correlations between structures and material properties are given. Those field-effects, which are the basis of today's commercial (nematic) displays, are reviewed. The performance of TN-LCDs and STN-LCDs, both operated with linearly as well as with circularly polarized light, and their dependence on LC material properties are shown. Recent progress in photo-aligning liquid crystals by our LPP technology is outlined (8). LPP alignment allows generation of high-resolution azimuthal LC director patterns with defined bias tilt angles in displays and, in combination with liquid crystal polymers, the generation of optically patterned optical retarders on single substrates (9). LPP photo-alignment also makes possible multidomain TN displays that exhibit much broader fields of view than today's single-domain TN-LCDs (8). Even broader fields of view result from deformed helix ferroelectric (DHF)-LCDs with their very short response times and video compatibility over broad operating temperature ranges (10). Also reviewed is a LCD projection concept

whose functional elements, i.e. polarizers, color filters, and modulators, consist entirely of liquid crystal elements such as cholesteric polarizers and color filters (11). Cholesteric optical concepts require new cholesteric LC materials; they lead to bright, compact, and light-weight LCD projectors and more efficient LCD reflectors.

LIQUID CRYSTAL MATERIAL PROPERTIES

Mesomorphic Properties

The unique anisotropic properties of liquid crystals, such as birefringence, dielectric, and diamagnetic anisotropies, their viscosity coefficients, and elastic constants are essential for any type of liquid crystal display. Liquid crystalline anisotropies are a consequence of inter- and intramolecular-specific electronic and steric interactions. These interactions lead to the liquid crystalline long-range order, which distinguishes liquid crystals from ordinary isotropic liquids (12–14). The continuum theories quantifying the anisotropic material properties of liquid crystals were detailed by de Gennes (15).

Figure 1 presents an example of a modern nematic liquid crystal molecule with a difluorinated three-ring rigid core and a (flexible) alkenyl side chain, i.e. a hydrocarbon side chain, with a C=C-double bond d in 3-position from the rigid core, i.e. a d_3 -double bond (16). We have shown that alkenyls considerably extend the range of material properties of liquid crystals (7, 16–18). Shifting alkenyl double bonds into different side chain positions strongly affects all

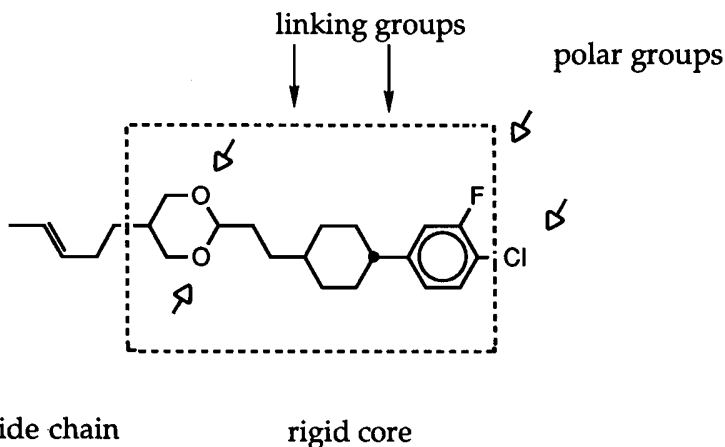


Figure 1 Positive dielectric halogenated alkenyl liquid crystal molecule 1d₃D₂CP_FCL of ROLIC Ltd. with alkenyl double bond d in 3-position from the rigid core. (see text) (37).

display relevant material properties (7, 17). Because of their unique and diverse material properties, alkenyls have become the key liquid crystals in all high information content STN-LCDs (18).

The long-range intermolecular interactions that characterize liquid crystalline mesophases cause the long molecular axes to align preferentially parallel over microscopic distances. The temperature-dependent preferred direction of the long molecular axes defines the direction of the nematic director \hat{n} . This preferred orientation is characterized by an order parameter S (12)

$$S = 1/2\langle 3 \cos^2 \beta - 1 \rangle, \quad 1.$$

where the brackets denote the average over the orientation of all molecules; β is the angle between \hat{n} and the long molecular axes. S decreases with increasing temperature and undergoes a first-order phase transition at the nematic-isotropic transition temperature T_c . In the isotropic phase, where the long-range interactions cease to exist, $S(T \geq T_c) = 0$ holds and, except for pretransitional effects such as the Kerr effect (19, 20), the anisotropies that characterize liquid crystals disappear. Therefore, a prerequisite for the applicability of any liquid crystal in a display is the design of molecules with broad enough mesomorphic phases to cover the temperature range required by a specific LCD application. Because there is no single liquid crystal compound that meets this requirement, practical liquid crystal materials are always more or less eutectic mixtures, comprising up to thirty different molecular structures. By proper selection, nematic phases result from -40°C to well over 120°C in mixtures (for example, see Reference 18).

From molecular modeling we have shown that it is possible to determine not only the most probable equilibrium configuration of actual liquid crystal molecules but also the equilibrium configuration of ensembles of actual molecules (7). Figure 2 shows such a configuration for a pair of antiparallel, aligned difluoro alkenyl molecules $1d_3\text{CCP}_F\text{F}$ of the type depicted in Figure 1, which we developed for TFT-TN LCDs. The heavy segments in the side chains represent the alkenyl double bonds, whereas the van der Waals electron radii of the difluoro substituted benzene rings are indicated (*arrow*) at the benzene rings. The dotted van der Waals representation of the antiparallel aligned molecules shows the typical all-*trans*, rod-shaped structure of thermotropic liquid crystals.

Static Dielectric Properties

Because the material properties of liquid crystals are the result of their molecular properties amplified by their long-range molecular interactions, the proper design of liquid crystals for a specific electro-optical effect and its different applications is crucial. Reliable techniques are required to determine the material parameters that can be related to the performance of the liquid crystal in a display (3).

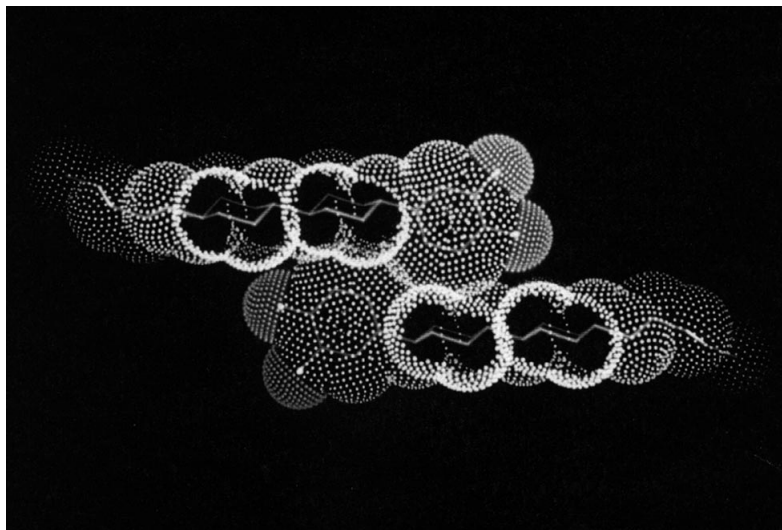


Figure 2 van der Waal representation of the equilibrium configuration of a pair of antiparallel aligned di-fluoro alkenyl liquid crystals $1,3\text{-CCPF}$ determined from interactive molecular modeling (7).

Figure 3 shows different nematic liquid crystal molecules (7, 16) of ROLIC. To achieve dielectric anisotropy requires the introduction of polar groups with permanent dipole moments $\hat{\mu}_i$. Polar groups such as $\text{C}\equiv\text{N}$ or $\text{C}-\text{F}$ lead to positive dielectric anisotropic compounds for which $\Delta\varepsilon = (\varepsilon_{\parallel} - \varepsilon_{\perp}) > 0$ holds; ε_{\parallel} and ε_{\perp} are the respective dielectric constants parallel and perpendicular to the nematic director \hat{n} . The four structures at the bottom of Figure 3 are examples of positive dielectric anisotropic liquid crystals. Their dielectric and optical anisotropies $\Delta\varepsilon$ and $\Delta n = (n_{\parallel} - n_{\perp})$, determined at constant reduced temperature $T/T_c = 0.9$, follow from Figure 3.

If antiparallel pair aggregation of molecules is neglected (21, 22) two mechanisms remain that contribute to the dielectric anisotropy of liquid crystals, namely induced and permanent dipolar contributions. The contribution of permanent molecular dipole moments $\hat{\mu}_i$ depends on their absolute values, their angles with respect to \hat{n} , and on the temperature-dependent Boltzmann distribution (23–25). The field-induced molecular polarizabilities $\hat{\alpha}_i$ depend on the position and the strength of functional molecular elements that are electronically conjugated, i.e. essentially on the number of aromatic rings in the rigid cores of the molecules and on the type of linkage. Because of the highly conjugated and elongated π -electron system along biphenyl cores, the cyanobiphenyls 5PP (26) in Figure 3 exhibit large polarizabilities α_{\parallel} along their long

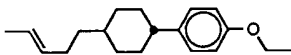
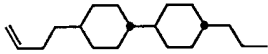
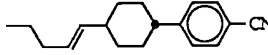
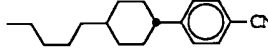

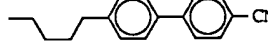
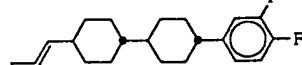
Nomenclature	Structure	T_m [°C]	T_c [°C]	$\Delta\epsilon$	Δn
1d ₃ CPO2		42	57	-0.27	0.09
0d ₃ CC3		18	77	0.15	0.04
3d ₁ CP		16	58	11.0	0.12
5CP		30	55	10.3	0.10
1d ₃ CC		79	100	4.4	0.05
5PP		24	35	13.3	0.18
1d ₃ CCP _F F		49	159	3.22	0.11

Figure 3 Melting (T_m) and nematic-isotropic transition temperatures (T_c) of nonpolar (1d₃CPO2, 0d₃CC3); polar (3d₁CP, 5CP, 1d₃CC, 5PP), and weakly polar (1d₃CCP_FF) nematic liquid crystals. Their dielectric ($\Delta\epsilon$) and optical (Δn) anisotropies are determined at $T/T_c = 0.9$

axes. Therefore, and due to the strong longitudinal permanent dipole moment $\hat{\mu}_{\parallel}$ (C \equiv N), larger dielectric anisotropies result for 5PP compared, for instance, with 5CP (27) (Figure 3).

Quantitatively the static dielectric anisotropy $\Delta\epsilon$ follows from the dielectric theory of Maier & Meier (24), who applied Onsager's theory of isotropic dielectrics to liquid crystals:

$$\Delta\epsilon = NhF/\epsilon_0[\Delta\alpha - F\mu^2/kT(1 - 3\cos^2\xi)]S, \quad 2.$$

where $h = 3\bar{\epsilon}/(2\bar{\epsilon} + 1)$, $\bar{\epsilon} = (\epsilon_{\parallel} + 2\epsilon_{\perp})/3$, $\Delta\alpha = (\alpha_{\parallel} - \alpha_{\perp})$, F = cavity reaction field, ξ = angle between $\hat{\mu}_{\parallel}$ and the long molecular axis, and N = number of molecules per unit volume. From Equation 2 follows the dependence of $\Delta\epsilon$ on the order parameter S . The first term in the brackets of Equation 2 describes the contribution of the molecular polarizability to $\Delta\epsilon$, whereas the second term

accounts for the permanent dipolar contribution. It is interesting to note that the induced polarization varies with temperature as S , whereas the temperature dependence of the orientational polarization varies as S/T . As a result, the temperature dependency of $\Delta\epsilon(T)$ of dielectrically strongly anisotropic liquid crystals basically follows S/T . This causes $|\Delta\epsilon|$ to increase with decreasing temperature. Meaningful comparisons of the dielectric, as well as of the optical and the elastic properties of liquid crystals, with different nematic-isotropic transition temperatures T_c can therefore be made only at constant reduced temperature T/T_c .

Examples of the temperature dependence of the static dielectric anisotropy of strongly positive dielectric anisotropic pyrimidine liquid crystals in their nematic and isotropic phases are shown in Figure 4 (28), which also shows the crucial influence of the position of the permanent nitrogen dipole moments on $\Delta\epsilon$. In the case of XP_1P , the pyrimidine moments and the terminal cyano moment are additive and lead to large dielectric anisotropies. On the other hand, and because of subtractive permanent molecular moments, small $\Delta\epsilon$ values result for XPP_2 (Figure 4). Also shown in Figure 4 is the abrupt transition of the dielectric anisotropy from $\Delta\epsilon(T < T_c) \gg 0 \rightarrow \Delta\epsilon(T > T_c) = 0$ at the first-order nematic-isotropic transition $T/T_c = 1$. Above T_c , a single isotropic dielectric constant ϵ_{is} exists (Figure 4).

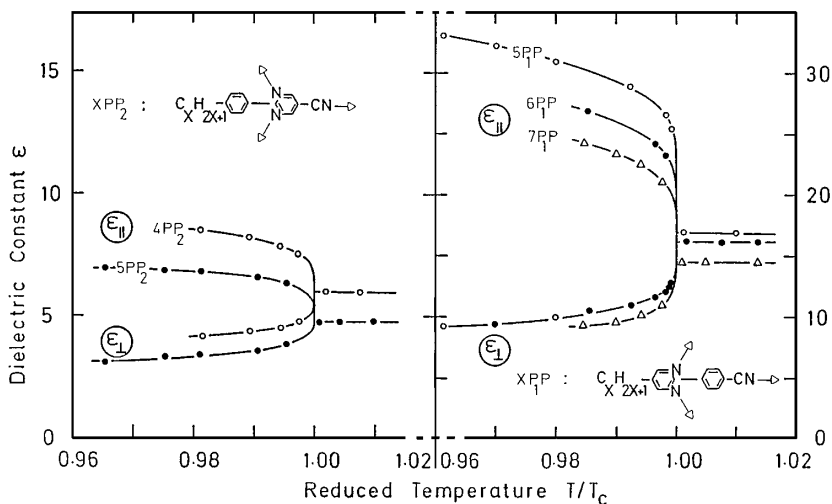


Figure 4 Temperature dependence of the dielectric constants ϵ_{\perp} and ϵ_{\parallel} of the nematic pyrimidines XP_2 and XP_1P . X denotes the number of carbon atoms in the alkyl side chains; the index y in the pyrimidine rings P_y denotes the position of the nitrogens (28).

Refractive Indices

The molecular polarizabilities α_i in Equation 2 not only contribute to the low-frequency dielectric constants of liquid crystals, they also determine their high-frequency dielectric properties, i.e. the ordinary and extraordinary refractive indices n_o and n_e (29). The Lorentz-Lorenz relation (25, 29) correlates the mean polarizability $\bar{\alpha} = (\alpha_{\parallel} + 2\alpha_{\perp})/3$ of a liquid crystal with its mean refractive index \bar{n} via:

$$(\bar{n}^2 - 1)/(\bar{n}^2 + 2) = N\bar{\alpha}/3\epsilon_0, \quad 3.$$

where $\bar{n}^2 = (n_e^2 + 2n_o^2)/3$. From Equation 3 follows qualitatively the great differences among the optical anisotropies $\Delta n = (n_e - n_o)$ of the different molecular structures depicted in Figure 3. SPP (26) in Figure 3, with the large polarizability of its highly conjugated π -electron system parallel to its long molecular axis, exhibits a much larger birefringence than Δn of the virtually non-aromatic alkenyl $\text{Ød}_3\text{CC3}$ (16).

Rotational Viscosity

Apart from their optical and dielectric anisotropies, liquid crystals exhibit anisotropic flow patterns that give rise to six different viscosity coefficients (15, 30). Among these, the rotational viscosity γ_1 is of practical importance. γ_1 describes the flow that results from an axial rotation of the nematic director \hat{n} . Since all field-effects on which LCDs are based make use of the optical changes associated with the field-induced realignment of the director pattern of macroscopically configured liquid crystal layers, the electro-optical response times of displays are strongly affected by the rotational viscosity (7, 31). A magneto-capacitive technique to determine γ_1 in displays requiring only a few milligrams of LC material is described in Reference 32. However, because the bulk or flow viscosity η is much easier to determine than γ_1 or the other viscosity coefficients, the somewhat ambiguous bulk viscosity is frequently used to characterize the viscosity of liquid crystals instead of γ_1 .

Elastic Constants

Because uniaxially aligned liquid crystals can be deformed in a defined manner by external mechanical forces and/or by magnetic and electric fields, different director deformation patterns can be achieved. These director deformations are described by the continuum theory developed by Oseen (33), Ericksen (34), and Leslie (35). For a general deformation of a nematic liquid crystal, the distortion free-energy density F_d of the nematic director \hat{n} follows from de Gennes (15):

$$F_d = k_1/2 \cdot (\text{div } \hat{n})^2 + k_2/2 \cdot (\hat{n} \cdot \text{curl } \hat{n})^2 + k_3/2 \cdot (\hat{n} \times \text{curl } \hat{n})^2. \quad 4.$$

The LC-specific material constants k_i in Equation 4 describe the elastic restoring forces in the three deformation states; namely splay (k_1), twist (k_2), and

bend (k_3). Like the above LC material parameters, these three main elastic constants are crucial for the operability and the performance of liquid crystal displays. Techniques to determine all three elastic constants (k_1 , k_2 , and k_3) in a single, parallel-aligned liquid crystal sample, using magnetic or electric field deformation and optical or capacitive detection of the deformation pattern, were developed by Gerber & Schadt (36).

We show below that the elastic constant ratio k_3/k_1 strongly affects the static and the dynamic performance of TN and STN displays. Because different electro-optical effects and display applications require liquid crystals not only with different optical and dielectric properties but also with different elastic constants, molecular structures were designed to cover a wide range of elastic properties. Figure 5 shows the temperature dependence of the bend/splay elastic constant ratio k_3/k_1 of a number of two-ring nematic liquid crystals with (a) different polar end groups, (b) different rigid cores, and (c) different alkyl and alkenyl side chains (7, 16, 17, 27). The molecules from References 7, 16, 17 were designed in our laboratories such that the combination of different structural elements leads either to very large or to very low bend/splay elastic constant ratios k_3/k_1 . An example for synergies that lead to low k_3/k_1 ratios is the combination of a heterocyclic dioxane ring D in the $\emptyset d_4$ DPO2 alkenyl liquid crystal (bottom row of Figure 5), which exhibits an even positioned ($\emptyset d_4$) double bond in its side chain and an overall small molecular polarity. This combination leads to one of the smallest elastic constant ratios $k_3/k_1 \sim 0.5$ in nematic liquid crystals (Figure 5). On the other hand, we have shown that exceptionally large elastic constant ratios result in alkenyl liquid crystals with double bonds in odd positions (17); see k_3/k_1 (1d₃CP) ~ 2.5 compared with k_3/k_1 (5CP) ~ 1.7 in Figure 5. The impact of these molecular and material parameters on the performance of STN-LCDs are outlined below.

The few examples of different liquid crystal structures in Figures 3–5 illustrate the strong synergies that can be achieved by properly incorporating different functional elements in liquid crystal molecules, which allow the tuning of mesomorphic, dielectric, optical, elastic, and other LC material parameters to the requirements of specific displays and their applications. More details on correlations between molecular structures, molecular ensembles, material properties, and electro-optical performance of different nematic liquid crystals are given below and in References 3, 7, 37, 38.

Dielectric Dispersion

In the nematic phase, the rotation of liquid crystal molecules around their short axes is strongly hindered by a rotational potential whose height depends on molecular structural elements and on temperature (21, 24, 39). This hindered rotation leads to a dispersion of the parallel dielectric constant $\varepsilon_{\parallel}(\omega)$,

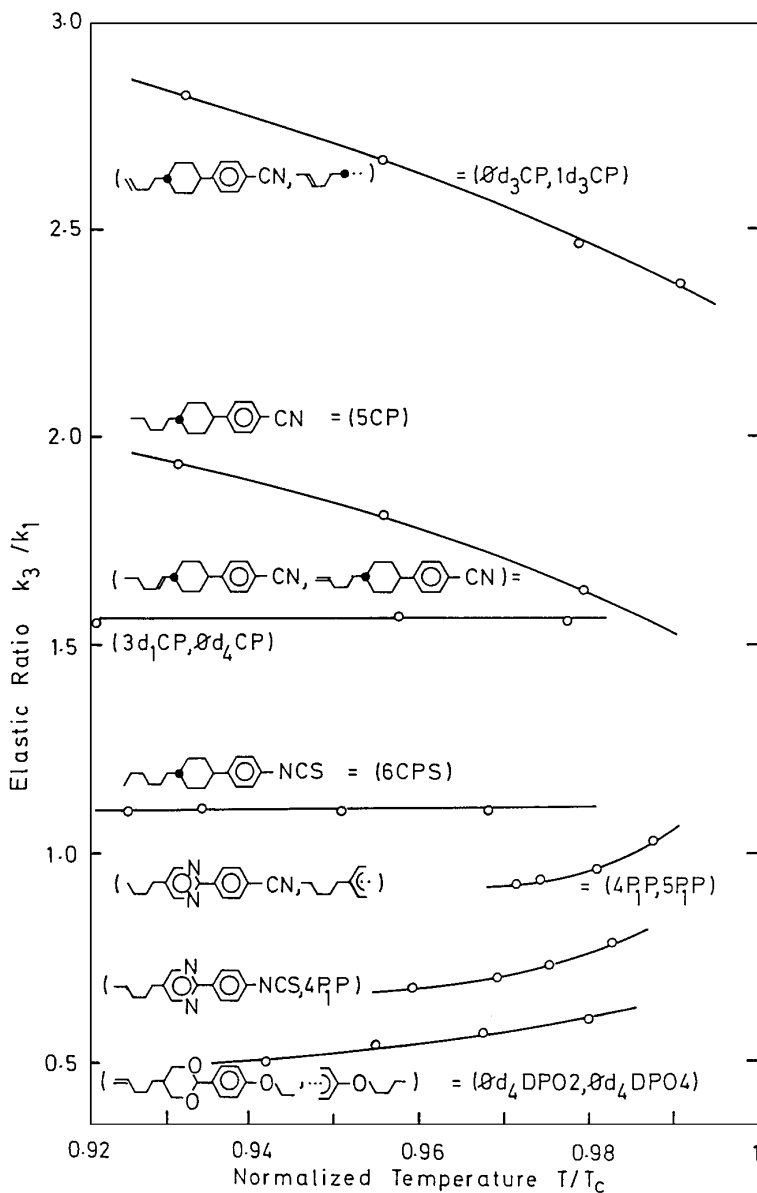


Figure 5 Dependence of the bend/splay elastic constant ratio k_3/k_1 on molecular structure and temperature (76).

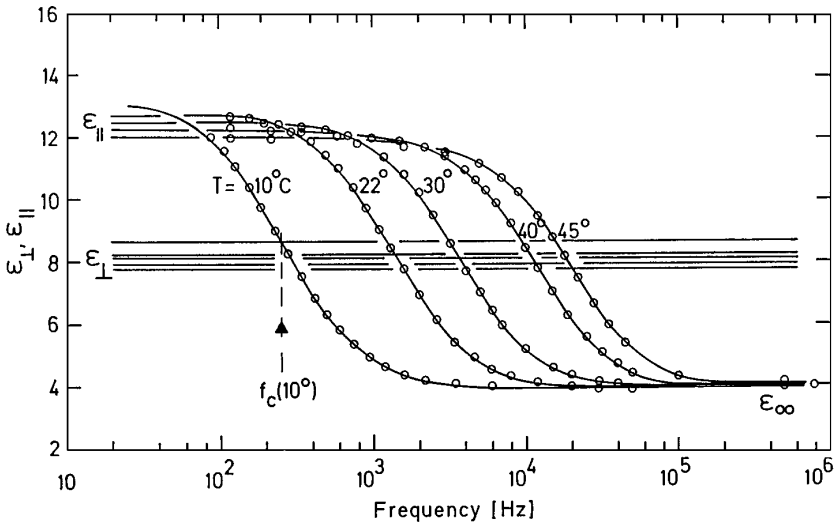


Figure 6 Frequency and temperature dependence of the dielectric constants ε_{\perp} and ε_{\parallel} of the dual-frequency addressable nematic liquid crystal mixture 3333 of ROLIC Ltd; f_c = dielectric cross-over frequency for which $\varepsilon_{\parallel}(f_c) = \varepsilon_{\perp}(f_c)$ holds (42).

which becomes for most liquid crystals effective only above 100 kHz at room temperature (21, 40). Therefore, and except for low temperatures, the electro-optical performance of displays is usually not affected by dielectric dispersion. However, for specially designed nematics we have shown that a strong frequency dependence $\varepsilon_{\parallel}(\omega)$ already can be generated at low-audio frequencies (42). The dispersion at low frequencies of $\varepsilon_{\parallel}(\omega)$ of such LCs, in combination with $\varepsilon_{\perp}(\omega) \simeq \text{constant}$ up to GHz frequencies, leads to a strong frequency dependence $\Delta\varepsilon(\omega)$ of the dielectric anisotropy in the low-audio frequency range (40). Moreover, for dedicated liquid crystals, $\Delta\varepsilon$ may even change sign at a cross-over frequency ω_c , where ω_c is defined by $\varepsilon_{\parallel}(\omega_c) = \varepsilon_{\perp}$ (42, 43). Figure 6 shows the frequency and the temperature dependence of ε_{\parallel} and ε_{\perp} of a nematic mixture whose dielectric dispersion lies in the audio frequency range. We developed such liquid crystals around 1980 for dual-frequency addressable light shutters with the aim to achieve short response times and/or steep transmission-voltage characteristics in twisted nematics displays (42). Because of the strong temperature dependence of the cross-over frequency ω_c , the application of dual-frequency addressable liquid crystal materials is limited to relatively narrow temperature ranges. Despite this restriction, dual-frequency addressable LCs have again become of interest for reducing the cross-talk of active matrix addressed displays (44).

Apart from temperature, the low-frequency dispersion $\varepsilon_{\parallel}(\omega)$ strongly depends on molecular structural properties such as polarity, rigidity, molecular length and, in the case of mixtures, on the mixture composition. For a single, Debye type of relaxation, the frequency dependence of $\varepsilon_{\parallel}(\omega)$ was shown to be (40)

$$\varepsilon_{\parallel}(\omega) = \varepsilon_{\infty} + \frac{(\varepsilon_{\parallel} - \varepsilon_{\infty})}{1 + \omega^2 \tau^2}, \quad \tau \propto \exp(E/kT); \quad 5.$$

where $\varepsilon_{\parallel} = \varepsilon_{\parallel}(\omega = 0)$ and $\varepsilon_{\infty} = \varepsilon_{\parallel}(\omega = \infty)$ are the static and the high-frequency parallel dielectric constants, respectively. The relaxation time $\tau = 1/\omega_0$ in Equation 5 is defined by the frequency where $\varepsilon_{\parallel}(\omega_0) = (\varepsilon_{\parallel} - \varepsilon_{\infty})/2$. According to Maier & Meier (24), the dispersion step $(\varepsilon_{\parallel} - \varepsilon_{\infty})$ increases for molecules with large longitudinal permanent dipole moments $\hat{\mu}_{\parallel}$ like:

$$(\varepsilon_{\parallel} - \varepsilon_{\infty}) = \frac{4\pi N h F^2}{3kT} \hat{\mu}_{\parallel}^2 (1 + 2S). \quad 6.$$

Equation 6 holds if $\hat{\mu}_{\parallel}$ coincides with the nematic director \hat{n} .

From Equation 6 it follows that the dispersion step $(\varepsilon_{\parallel} - \varepsilon_{\infty})$ depends, as does ε_{\parallel} , on $\hat{\mu}_{\parallel}$. Therefore, the dispersion anisotropy $(\varepsilon_{\parallel} - \varepsilon_{\infty})$ and ε_{\parallel} are interdependent parameters. On the other hand ε_{\perp} does not depend on the parallel dielectric properties of the liquid crystal, i.e. ε_{\perp} is independent of ε_{\parallel} and $(\varepsilon_{\parallel} - \varepsilon_{\infty})$. As a consequence, it is generally not possible with a single liquid crystal component to achieve (a) a large dispersion step and (b) independently adjustable low- as well as high-frequency dielectric anisotropies $\Delta\varepsilon_{\perp} = \Delta\varepsilon(\omega \ll \omega_c)$ and $\Delta\varepsilon_{\parallel} = \Delta\varepsilon(\omega \gg \omega_c)$ (42). However, because the dielectric anisotropy $\Delta\varepsilon$ of a binary mixture follows from $\Delta\varepsilon^A$ and $\Delta\varepsilon^B$ of its components A and B (42),

$$\Delta\varepsilon = m_A \Delta\varepsilon^A + m_B \Delta\varepsilon^B; \quad m_A + m_B = 1, \quad 7.$$

where m_A and m_B are the molar amounts of the two components, both conditions (a) and (b), as well as the requirement of low-frequency dielectric dispersion, can be realized with at least two properly designed LC components A and B (42).

To render component A suitable in the above sense, it must exhibit a large positive static dielectric anisotropy $\Delta\varepsilon_{\perp}^A \gg 0$ and a low cross-over frequency f_c^A . On the other hand, component B must meet the requirements $\Delta\varepsilon_{\perp}^B < 0$ and $f_c^B \gg f_c^A$. Then, from $\Delta\varepsilon_{\perp}^A \gg 0$ and from Equations 6 and 7, it follows that the dispersion step $(\varepsilon_{\parallel} - \varepsilon_{\infty})$ of the mixture can be made large enough to cause its dielectric anisotropy $\Delta\varepsilon(\omega)$ to change sign at f_c . As a consequence, the director \hat{n} of the mixture will align parallel to an applied electric field at frequencies $f < f_c$ ($\hat{n} \parallel \hat{E}$), whereas for $f > f_c$ ($\hat{n} \perp \hat{E}$) realignment from the homeotropic into the planar state occurs. Because $f_c^B \gg f_c^A$, the low-frequency dispersion

of $\varepsilon_{\parallel}(\omega)$ of the mixture and the height of the dispersion step are essentially determined by the relaxation of the A-type molecules in the mixture. However, via viscous coupling, molecules B also affect the onset of dispersion. Since $\varepsilon_{\perp} = \text{constant}$ holds up to microwave frequencies (20), we have shown from Equations 5 and 7 that the frequency dependency of the dielectric anisotropy of a binary mixture comprising the above specified components A and B becomes (42)

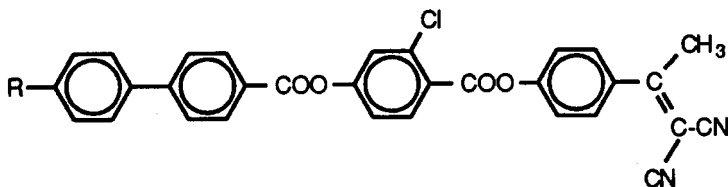
$$\Delta\varepsilon(\omega) = m_A \left[\varepsilon_{\infty}^A + \frac{(\varepsilon_{\parallel}^A - \varepsilon_{\infty}^A)}{1 + \omega^2\tau^2} \right] + m_B \Delta\varepsilon^B - m_A \varepsilon_{\perp}^A. \quad 8.$$

In the static limit, the low-frequency dielectric anisotropy $\Delta\varepsilon_L$ of a dual frequency addressable mixture follows from Equation 6, i.e. $\Delta\varepsilon(\omega \ll \omega_o) = \Delta\varepsilon_L$ holds. In the high-frequency limit, Equation 8 becomes

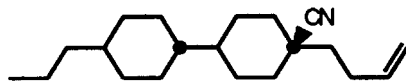
$$\Delta\varepsilon(\omega \gg \omega_c) = \Delta\varepsilon_H = m_A(\varepsilon_{\parallel}^A - \varepsilon_{\perp}^A) + m_B \Delta\varepsilon^B. \quad 9.$$

From Equations 7, 8, and 9 it follows that both dielectric anisotropies $\Delta\varepsilon_L$ and $\Delta\varepsilon_H$ of a binary mixture can be independently adjusted by choosing m_A and m_B appropriately (42). Analogous equations hold for multicomponent mixtures if their components meet the above requirements. Figure 6 depicts the dielectric dispersion of a dual-frequency addressable multicomponent mixture developed in our laboratories along the above criteria (42).

The dual-frequency addressable mixture depicted in Figure 6 comprises the following components A (42):



which determine its low-frequency dispersion. To achieve its large negative dielectric anisotropy at high frequencies, axially substituted alkenyl liquid crystals of the type



were used as components B (37).

We have shown that dual-frequency addressing leads (a) to steep transmission voltage characteristics in TN-displays, (b) to short turn-off times, and (c) to in

situ heating of LCDs (42, 43). Moreover, dielectric dispersion may adversely affect the performance of displays. In the following, these aspects are further detailed.

Dual-Frequency Addressing of Displays

If a high-frequency voltage $V(f \gg f_c) = V_H$ is superimposed on the usual, low-frequency display driving voltage $V(f \ll f_c) = V_L$ of a TN display, the field-induced energy in the liquid crystal layer, which corresponds to a display transmission of $x\%$, was shown to follow from (42):

$$\Delta\varepsilon_L V_x^2(V_H) - |\Delta\varepsilon_H| V_H^2 = \Delta\varepsilon_L V_x^2(V_H = 0). \quad 10.$$

Because liquid crystals with low-threshold voltages are desirable, $|\Delta\varepsilon| \gg 0$ holds for most TN displays. Therefore, and because the dielectric displacement $D = \varepsilon_0 \varepsilon \hat{E}$ is constant in the display, the electric field \hat{E} cannot be assumed to remain constant across the liquid crystal layer for voltages exceeding the threshold voltage V_c of the field-induced mechanical deformation of the TN helix. Equation 10 is therefore only correct for voltages $V \leq V_c$. However, to a first approximation and to obtain analytical expressions, it can be assumed that Equation 10 also holds for voltages that slightly exceed V_c . Then, from the definition of the slope parameter $\alpha = (V_{50} - V_{10})/V_{10}$, which defines the steepness of the voltage-transmission dependence of the display at 50% transmission and from Equation 10, one obtains (42)

$$V_{10}^2(V_H) \simeq V_{10}^2(V_H = 0) + \frac{|\Delta\varepsilon_H|}{\Delta\varepsilon_L} V_H^2 = \frac{V_{50}^2(V_H = 0)}{(1 + \alpha_L)^2} + \frac{|\Delta\varepsilon_H|}{\Delta\varepsilon_L} V_H^2; \quad 11.$$

where V_{10} and V_{50} are the voltages corresponding to 10 and 50% display transmission respectively; $\alpha_L = \alpha(V_H = 0)$. As a consequence of the superposition of V_H on V_L , Equation 11 predicts a shift of the voltage-transmission characteristics of the display toward higher voltages.

To determine quantitatively the multiplexibility of a dual-frequency addressed TN display versus superimposed high-frequency voltage V_H and versus LC material parameters, the dependence of the slope parameter $\alpha_H = \alpha(V_H, \Delta\varepsilon_L, \Delta\varepsilon_H)$ was derived, where the maximum number N_{\max} of multiplexible lines follows from (45, 46)

$$N_{\max} = \left[\frac{(1 + \alpha)^2 + 1}{(1 + \alpha)^2 - 1} \right]^2. \quad 12.$$

Because an expression analogous to Equation 11 holds for $V_{50}(V_H)$, we have shown from the definition of α and from Equation 11 that the slope of the voltage-transmission dependence of a display driven with a superimposed high

frequency voltage is (42)

$$\alpha_H \cong \left[\frac{(\alpha_L + 1)^2 + \frac{|\Delta\varepsilon_H|}{\Delta\varepsilon_L} \left(\frac{V_H}{V_{10,L}} \right)^2}{1 + \frac{|\Delta\varepsilon_H|}{\Delta\varepsilon_L} \left(\frac{V_H}{V_{10,L}} \right)^2} \right]^{1/2} - 1, \quad 13.$$

where $V_{10,L} = V_{10}(V_H = 0)$. From Equation 13 it follows that the high-frequency slope parameter α_H decreases for increasing dielectric ratio $|\Delta\varepsilon_H/\Delta\varepsilon_L|$ and/or for increasing voltage ratio $V_H/V_{10,L}$. Therefore, the superposition of a high-frequency voltage to the display causes α_H to decrease and, as a consequence, the number of multiplexible lines increases. We have quantified the multiplexing improvement that results from dual-frequency addressing versus conventional low-frequency driving by the ratio (42)

$$\frac{N_{\max}^H}{N_{\max}^L} \cong \left\{ \frac{[(1 + \alpha_H)^2 + 1][(1 + \alpha_L)^2 - 1]}{[(1 + \alpha_H)^2 - 1][(1 + \alpha_L)^2 + 1]} \right\}^2, \quad 14.$$

which follows from Equations 11, 12, and 13. In Equation 14, $N_{\max}^L = N_{\max}(V_H = 0)$ and $N_{\max}^H = N_{\max}(V_H)$, denoting the maximum number of multiplexible lines for conventional and dual-frequency addressing, respectively.

The validity of Equations 11–14, whose low-frequency transmission parameters α_L , V_{10} , and V_{50} implicitly contain the liquid crystal material constants that govern the static electro-optical performance of a specific field-effect, is not restricted to TN displays. The approximations also are applicable to other field effects as long as Equation 10 holds. In the case of TN displays operated at vertical light incidence in their second transmission minimum (cf Equation 30 below), we derived the following LC material-dependent analytical approximations for V_{50} and α_L (38) which, when inserted into Equation 11, lead to

$$V_{50}(V_H = 0) \cong V_c \left[2.044 - \frac{1.044}{1 + k_3/k_1} \right] \cdot \{1 + 0.12[(\Delta\varepsilon/\varepsilon_\perp)^{0.6} - 1]\} \\ \cdot \left[1 + 0.132 \ln \frac{\Delta nd}{2\lambda} \right], \quad 15.$$

$$\alpha_L = (V_{50} - V_{10})/V_{10} \cong 0.133 + 0.0266(k_3/k_1 - 1) + 0.0443 \left(\ln \frac{\Delta nd}{2\lambda} \right)^2; \quad 16.$$

where $V_{10}(V_H = 0)$ in Equation 11 follows from the definition of α_L and from Equations 15 and 16:

$$V_{10}(V_H = 0) \cong V_{50}(V_H = 0) \cdot \left[0.88 - 0.024 \frac{\Delta\varepsilon}{\varepsilon_\perp} - 0.04 \left(\ln \frac{\Delta nd}{2\lambda} \right)^2 \right]. \quad 17.$$

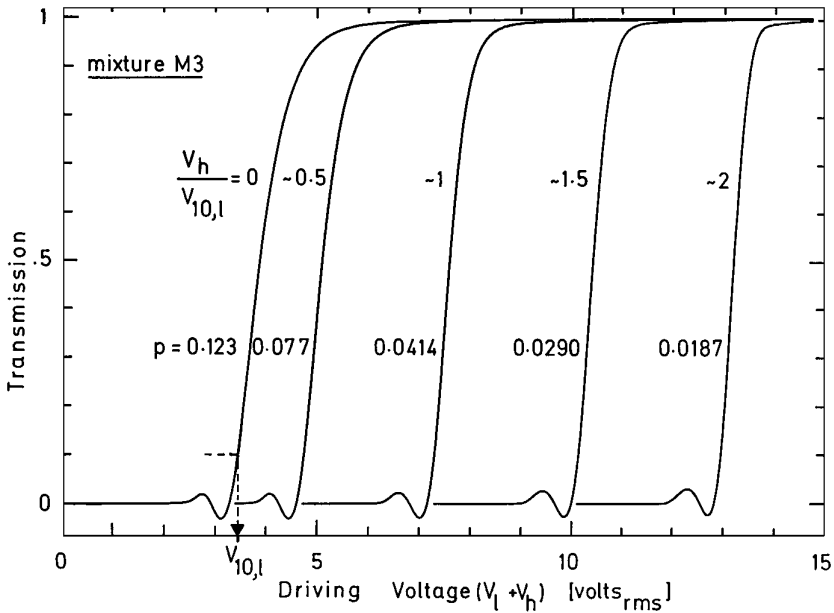


Figure 7 Transmission versus voltage dependence of TN-LCDs comprising the dual-frequency addressable mixture 3333 of ROLIC Ltd., determined at 22°C with driving frequencies $f_L = 80$ Hz and $f_H = 10$ kHz, respectively. The superimposed high-frequency driving voltages V_H , which correspond to the different graphs, follow from the respective voltage ratios $V_H/V_{10,L} = 0, 0.560, 1.123, 1.684, 2.245$, and from $V_{10,L} = 3.46$ V (42).

In Equations 15–17 the LC material parameters are $\Delta n = (n_e - n_o)$, d = electrode spacing, and λ = wavelength of transmitted light. V_c in Equation 15 is the threshold voltage for the field-induced mechanical deformation of a 90° twisted TN display (1):

$$V_c = \pi \left[\frac{1}{\epsilon_o \Delta \epsilon_L} \left(k_{11} + \frac{k_{33} - 2k_{22}}{4} \right) \right]^{1/2} = \pi \left[\frac{\kappa}{\epsilon_o \Delta \epsilon_L} \right]^{1/2} \quad 18.$$

Equations 11–17 show the dependence of the voltage-transmission characteristics of a TN display on its dielectric, optical, and elastic liquid crystal material parameters, as well as on the superimposed high-frequency voltage V_H under dual-frequency addressing conditions at vertical light incidence in the second transmission minimum (38, 42).

Figure 7 shows the transmission-voltage dependence of a dual-frequency addressed TN display (42). For each graph a different high-frequency voltage V_H , defined by the ratio $V_H/V_{10,L} = \text{constant}$, was superimposed on the display,

where $V_{10,L} = V_{10}(V_H = 0)$ designates the conventional low-frequency driving voltage at 10% transmission. The values of $V_{10,L}$ follow from the first graph on the left for which $V_H/V_{10,L} = 0$. Figure 7 confirms the above, namely that dual-frequency addressing increases the multiplexibility of TN-LCDs and causes the threshold voltage to increase (42, 47). To prevent detrimental voltage variations in high-information content thin film transistor addressed TN-displays from spurious dual frequency addressing effects, liquid crystals with cross-over frequencies $f_c > 100$ kHz are required (see below). The significant reduction of the turn-off-time of TN-LCDs resulting from dual-frequency addressing (42) was used to improve the response times of early LCD line-printers (48).

Dielectric Heating of Displays

We have shown that dielectric dispersion in liquid crystals can cause remarkable temperature increases in displays due to dielectric heating (43). Dielectric heating needs to be taken into account when addressing high-information content LCDs and/or when using liquid crystals whose range of dielectric dispersion extends into the driving frequency range of the display (41).

The frequency dependence of the complex dielectric constant $\varepsilon^*(\omega)$ of a liquid crystal, which leads to dielectric losses, follows from (43)

$$\varepsilon^*(\omega) = \varepsilon'(\omega) + j\varepsilon''(\omega), \quad \text{where}$$

$$\varepsilon'(\omega) = \frac{(\varepsilon_s - \varepsilon_\infty)}{(1 + \omega^2\tau_n^2)} + \varepsilon_\infty, \quad \text{and}$$

$$\varepsilon''(\omega) = \frac{(\varepsilon_s - \varepsilon_\infty)\omega\tau_n}{(1 + \omega^2\tau_n^2)}. \quad 19.$$

In Equations 19, $\varepsilon'(\omega)$ and $\varepsilon''(\omega)$ are the real and the imaginary parts of the Debye-type of molecular relaxation (49). ε_s and ε_∞ are the low-(static) and the high-frequency dielectric constants of the respective dispersion region. The relaxation time $\tau_n = 1/\omega_n = 1/2\pi f_n$ can be determined from measurements of $\varepsilon'(\omega_n) = (\varepsilon_s + \varepsilon_\infty)/2$ in the n th dispersion region of $\varepsilon'(\omega)$. The dielectric dissipation, which generates heat in the liquid crystal layer, follows from $\varepsilon''(\omega)$ in Equations 19. Maximum losses occur at the angular frequency ω_n . If one assumes the relaxation to be hindered by an activation energy E_n , and if τ_n depends exponentially on temperature, τ_n becomes

$$\tau_n = \tau_o \exp\left(\frac{E_n}{k_T}\right) \quad 20.$$

There are essentially two heat sources determining the actual temperature $T = (T_e + \Delta T)$ in the nematic layer of a display, namely the external cell temperature

T_e and the dielectric relaxation process, which causes the display temperature to increase by ΔT above T_e . For the power P dissipated in the LC layer due to dielectric losses, it follows from Equations 19 and 20 (43)

$$P = \left[\frac{V^2 A \varepsilon_o (\varepsilon_s - \varepsilon_\infty)}{d} \right] \cdot \left[\frac{\omega^2 \tau_n}{(1 + \omega^2 \tau_n^2)} \right], \quad 21.$$

where A = electrode area, d = thickness of the nematic layer, and V = cell voltage (rms). If the heat losses through the display substrates are Q_1 , one obtains for the approximate heat Q_o stored in the display:

$$Q_o \approx Pt - Q_1 \approx c\Delta T, \quad 22.$$

where c is the average heat capacity of the cell. c is primarily determined by the glass plates and by the LC layer; t = dielectric heating time. If linear heat losses $Q_1 \propto \Delta T$ are assumed, Q_1 becomes:

$$Q_1 \approx q_1 \Delta T t;$$

where q_1 is the specific heat conductivity of the display substrates. For temperature increases $\Delta T \ll kT_e^2/E_n$, a condition that always holds in reality, it follows from Q_1 and from Equations 21 and 22

$$\Delta T = \left[\frac{V^2 A \varepsilon_o (\varepsilon_s - \varepsilon_\infty)}{d(C + q_1 t)} \right] \cdot \left[\frac{\tau_n \omega^2 t}{(1 + \omega^2 \tau_n^2)} \right]. \quad 23.$$

Equation 23 describes the increase of the display temperature ΔT above T_e due to dielectric heating (43). Heat losses due to radiation are neglected. Also neglected is lateral heat diffusion from dielectrically heated into nonheated display regions (segmented electrodes).

From Equation 23 it follows that for extended periods of dielectric heating, stationary temperatures $T = (T_e + \Delta T)$ are established in the nematic layer. Two different frequency regions are of special interest in the stationary state $t \rightarrow \infty$; namely (43):

$$\Delta T \left(\omega \ll \frac{1}{\tau_n} \right) = \left[\frac{V^2 A \varepsilon_o (\varepsilon_s - \varepsilon_\infty)}{q_1 d} \right] \cdot \omega^2 \tau_n \quad \text{and} \quad 24.$$

$$\Delta T \left(\omega \gg \frac{1}{\tau_n} \right) = \left[\frac{V^2 A \varepsilon_o (\varepsilon_s - \varepsilon_\infty)}{q_1 d} \right] \cdot \tau_n^{-1}. \quad 25.$$

From Equation 24 it follows that at low frequencies, the temperature $\Delta T \propto \omega^2 \tau_n$ increases quadratically with frequency; whereas Equation 25 shows that for $\omega \rightarrow \infty$ the increase ΔT becomes independent of frequency and reaches a maximum stationary value that increases with decreasing relaxation time

τ_n . Therefore, the efficiency of dielectric heating increases in liquid crystals that exhibit high-frequency dispersion. Conversely, because the dispersion frequency range of liquid crystals decreases with decreasing temperature due to increasing viscosity (Figure 6), the efficiency of dielectric heating diminishes at low temperatures. At low and high frequencies it follows from Equations 24 and 25 that ΔT depends on the square of the applied voltage and that ΔT increases linearly with decreasing electrode spacing d and increasing dielectric dispersion height $(\epsilon_s - \epsilon_\infty)$. Reducing heat losses through the electrodes and/or reducing the heat capacity of the electrode substrates increases the stationary temperature $T = (T_c + \Delta T)$ of the LC layer. Within seconds, temperature changes as great as 60°C can be generated in displays by dielectric heating (43).

Influence of Charge Carriers on the Performance of Passively and Actively Addressed Displays

Recently we have shown that charge transport in liquid crystals and the complex impedance of liquid crystal displays not only strongly affect the electro-optical performance of active matrix-addressed TN displays, but also the frequency dependence of the optical appearance of passively addressed TN and STN displays (41). Because modern, halogenated liquid crystals can be purified to the extent that their residual resistivity reaches values of high-quality insulators, the investigation of charge transport mechanisms in liquid crystal layers over a broad range of resistivities has become possible by selectively doping liquid crystals with ionic impurities (41).

Figure 8 shows the equivalent circuit of a liquid crystal display picture element from which the single exponential current decay $I(t)$ with time constant

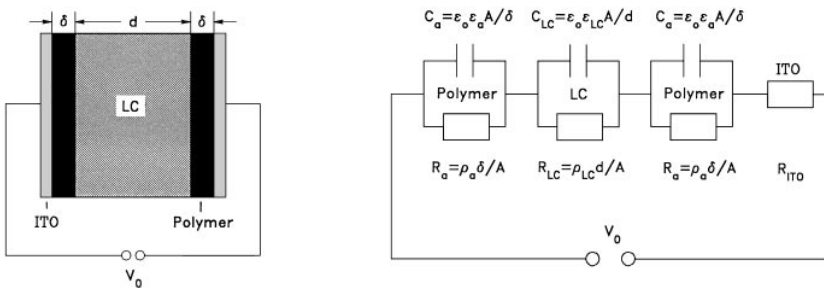


Figure 8 (Left) Schematic of a picture element (pixel) of a TN cell. (Right) Equivalent circuit of a TN-LCD pixel (41).

τ follows upon applying a voltage V_0 (41)

$$I(t) = I_\infty + I_0 \exp(-t/\tau), \quad \tau = \varepsilon_0 \frac{\varepsilon_{ad} + 2\varepsilon_{LC}\delta}{d/\rho_a + 2\delta/\rho_{LC}}, \quad 26.$$

$$I_\infty = I(t = \infty) = V_0/(R_{LC} + 2R_a + R_{ITO}).$$

From the complex liquid crystal display impedance of the circuit in Figure 8, the frequency dependence of the actual voltage V_{LC} across the liquid crystal layer becomes (41)

$$V_{LC}^2 = \frac{R_{LC}^2 ab^2 V_0}{(2R_a a + R_{LC} b + R_{ITO} ab)^2 + \omega^2 (2R_a^2 C_a a + R_{LC}^2 C_{LC}^b)^2}, \quad 27.$$

where

$$a = 1 + (\omega R_{LC} C_{LC})^2; \quad b = 1 + (\omega R_a C_a)^2; \quad \omega = 2\pi f.$$

As a consequence of the frequency dependence of $V_{LC}(\omega)$, the electro-optical appearance of the display also must depend on the frequency and circuit parameters depicted in Figure 8. From Equation 27 it follows that at low (<10 Hz) and high frequencies ($>10^4$ Hz) the effective voltage V_{LC} across the LC layer decreases. To keep $V_{LC} = \text{constant}$, the external driving voltage V_0 , which must be applied to maintain constant display transmission, has to increase. At low frequencies, V_{LC} decreases for decreasing ρ_{LC} or increasing polymer aligning layer thickness δ (Equation 27), whereas large ITO-electrode resistivities cause V_{LC} to decrease at high frequencies (Equation 27). Figure 9 depicts the frequency dependence $V_{10}(f)$ of the threshold voltage of a TN display at 10% transmission calculated from Equation 27 (41). Because frequency-dependent variations of V_{10} reduce the contrast of time-multiplexed liquid crystal displays, the display parameters, the LC material constants and the driving conditions must be chosen such that no frequency dependence occurs within the operating bandwidth of the display.

Gruler & Cheung showed that the LC conductivity σ , which is caused by spurious ionic impurities, may also contribute to the director deformation and thus affect the electro-optics. For the voltage $V_{LC}(\phi)$ required to induce a defined director deformation ϕ_m in the center of a conducting, parallel aligned LC-layer, they derived (50)

$$V_{LC}(\phi) \cong (1 + \phi_m^2 (k_3/k_1 + c)/4) V_c, \quad 28.$$

where

$$c = \frac{\frac{\sigma_{\parallel} - \sigma_{\perp}}{\sigma_{\perp}} + \left(\frac{\omega}{\omega_0}\right)^2 \frac{\varepsilon_{\parallel} - \varepsilon_{\perp}}{\varepsilon_{\perp}}}{1 + (\omega/\omega_0)^2}; \quad \omega_0 = \frac{\sigma_{\perp}}{\varepsilon_0 \varepsilon_{\perp}} \quad \text{and} \quad \omega = 2\pi f.$$

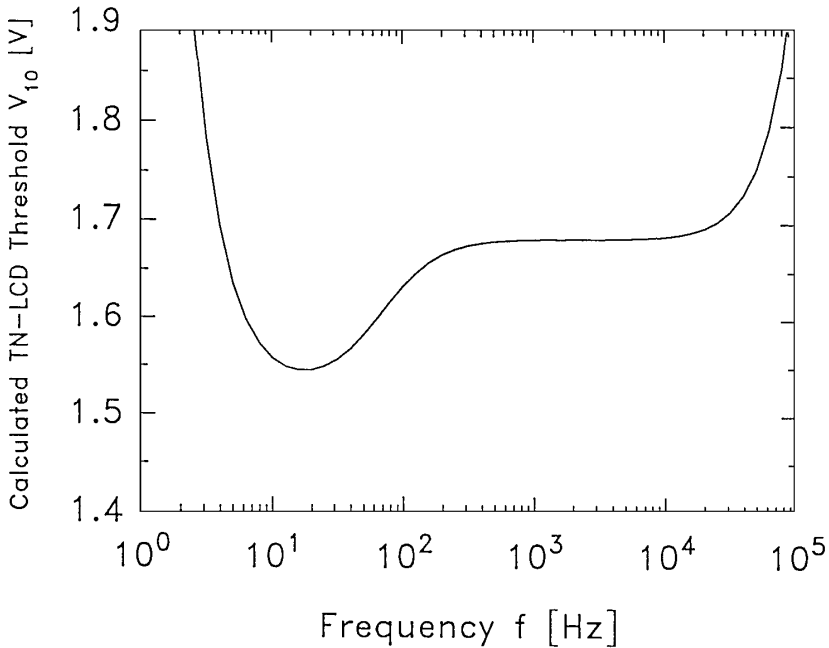


Figure 9 Calculated frequency dependence $V_{10}(f)$ of TN-LCD threshold voltage at 10% transmission. The LC material parameters of mixture 3825 of ROLIC Ltd. are $\rho_{LC} = 5 \times 10^7 \Omega\text{m}$, $\epsilon_{\perp} = 5.3$, $\Delta\epsilon = 10.5$, $\epsilon_a = 3$, $\sigma_{\parallel}/\sigma_{\perp} = 1.3$, $k_{33}/k_{11} = 1.5$, $\phi_m = 30^\circ$, $V_{th} = 1.32$. The LCD parameters: $\rho_a = 10^{10} \Omega\text{m}$, $R_{ITO} = 5 \text{ k}\Omega$, $d = 8 \mu\text{m}$, $\delta = 0.1 \mu\text{m}$ (41).

V_c is the threshold voltage for mechanical deformation of the LC layer. For highly resistive liquid crystals for which $\sigma = 0$ holds, Equation 28 reduces to the purely field-induced case for which no current-induced frequency dependence occurs, i.e. $c = 0$ in Equation 28. In this case, Equation 27 does not have to be modified.

Because the frequency-dependent coefficient c in Equation 28 does not depend on the elastic properties of the liquid crystal, the frequency dependency of $V_{LC}(\phi)$ of a parallel aligned display should be identical to that of a TN display. However, because the elastic constants affect the maximum change of $V_{LC}(\phi)$ versus frequency, the dynamic range of $V_{LC}(\phi)$ of a TN-display is only partly described by Equation 28. Despite this restriction, it is interesting to estimate (from Equations 27 and 28) the combined frequency influence of the LC conductivity and the equivalent circuit parameters on the optical TN display threshold voltage. If one inserts the angle ϕ_m corresponding to 10% TN display transmission for the angle of the director deformation, the voltage V_0 , which has to be applied to the display, follows from the equality of Equations 27 and

28. Figure 9 shows the frequency dependence $V_{10}(f)$, which we calculated for a TN display (41). A similar dependence holds for STN displays. The calculation is based on the LC material and display parameters depicted in the legend of Figure 9. The calculated frequency dependence of V_{10} in Figure 9, which follows from the equivalent circuit in Figure 8 and from Equations 27 and 28, was experimentally confirmed (41).

Unlike the low- and the high-frequency dependencies of $V_{10}(f)$, the dip of the threshold voltage that occurred at around 200 Hz (Figure 9) cannot be explained solely by field-induced phenomena. The dip can only be explained if one also takes current-induced director deformations in the LC layer into account. Indeed, we have shown that the dip of $V_{10}(f)$ in Figure 9 can be modeled if the current-induced deformation mechanism following from Equation 28 is included in Equation 27 (41).

The frequency-independent plateau of V_{10} in Figure 9 is the range within which proper display operation is possible. The frequency independence of V_{10} in this range follows from the equivalent circuit in Figure 8 and from Equation 27. Here the effective voltage V_{LC} across the LC layer in the frequency range of the plateau becomes

$$V_{LC} = \frac{C_a}{C_a + 2C_{LC}} V_0 = \frac{\varepsilon_a d}{\varepsilon_a d + 2\varepsilon_{LC} \delta} V_0. \quad 29.$$

From Equation 29 follows $V_{LC} = V_0$ for $\varepsilon_a d \gg 2\varepsilon_{LC} \delta$. Within the region of the plateau, V_{10} depends on only the elastic, dielectric, and optical LC material properties. In the case of TN displays, Equation 31 describes V_{LC} in this frequency range. For highly resistive LC materials ($\rho_{LC} > 10^{10} \Omega\text{m}$), the frequency-independent plateau extends below 10 Hz, thus extending the bandwidth within which the display can be operated without cross talk (41).

It should be noted that TN displays with very low threshold voltages ($V_{10} \lesssim 1$ V) comprise liquid crystals with large dielectric anisotropies such as those exhibited by cyano-pyrimidines (Figure 4). Therefore, and because appreciable field-induced director alignment occurs at 10% transmission in a TN display (51), the above condition $\varepsilon_a d \gg 2\varepsilon_{LC} \delta \sim 2\varepsilon_{\parallel} \delta$ may no longer hold. As a consequence, a rather strong influence of the aligning layer thickness δ on the optical threshold V_{10} results for large $\Delta\varepsilon_s$. This causes the V_{10} plateau in Figure 9 to rise with increasing δ (Equation 29), i.e. larger driving voltages are required to achieve a given display transmission.

Apart from the cell technology-dependent increase of V_{10} at high frequencies (Figure 9, and as shown above), dielectric dispersion in the LC material may also cause V_{10} to increase at high frequencies. However, this can be avoided by designing (low viscous) liquid crystal molecules that are not rotationally hindered within the operating frequency range of the display, i.e. below 100 kHz.

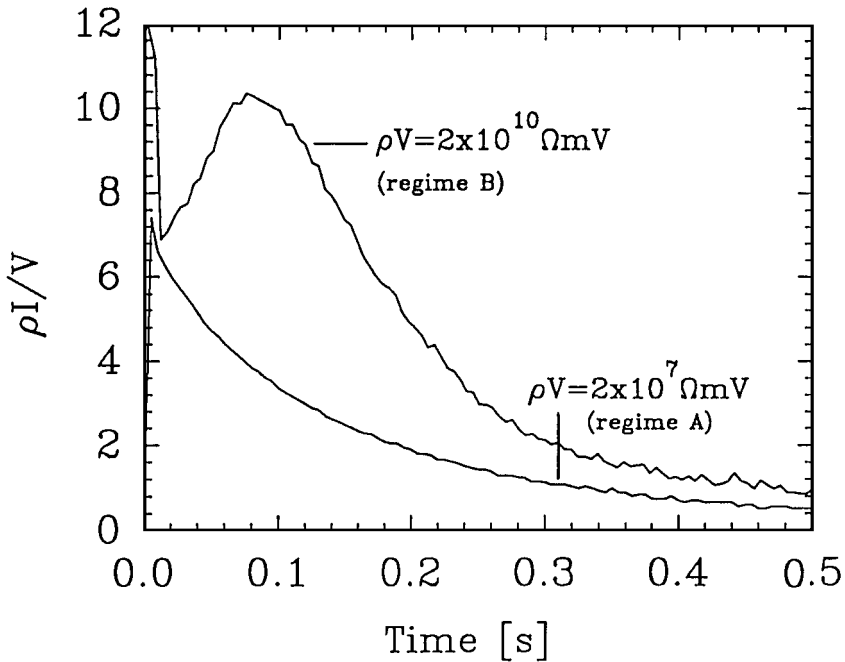


Figure 10 Normalized TN-LCD currents in regimes A and B recorded at 22°C using mixtures 3825 (regime A) and 7380 (regime B) of ROLIC Ltd. The respective driving voltages are 0.2 and 1.8 V, which are both below the mechanical thresholds of the respective mixtures (41).

For various aligning layer resistivities ρ_a and layer thicknesses δ (Figure 8), as well as for six decades of LC resistivities, $10^6 \Omega\text{m} \leq \rho_{\text{LC}} \leq 10^{12} \Omega\text{m}$, we have shown that the simple exponential decay of Equation 26 is valid only within a conductivity regime A, which is characterized by the product $\rho_{\text{LC}} V < 10^9 \Omega\text{mV}$. In a second regime, B, where this product becomes $\rho_{\text{LC}} V > 10^9 \Omega\text{mV}$, space-charge limited currents occur that do not follow from the linear equivalent circuit in Figure 8 (41). As a consequence of space-charge effects, markedly different time dependences of the pixel current result in the two regimes, A and B, upon applying a voltage V_0 to the display (41). This is shown in Figure 10 where the normalized pixel current follows the single exponential decay of Equation 26 only in regime A. In the highly resistive regime B, a transient current peak occurs from the build-up of space-charge within the liquid crystal layer. This space-charge formation, depicted in Figure 11, is caused by the rapid depletion of the charge carrier density in the center of the low conductivity liquid crystal layer upon application of V_0 to the display. Because highly resistive LC materials are crucial for realizing active-matrix-addressed displays, time-dependent

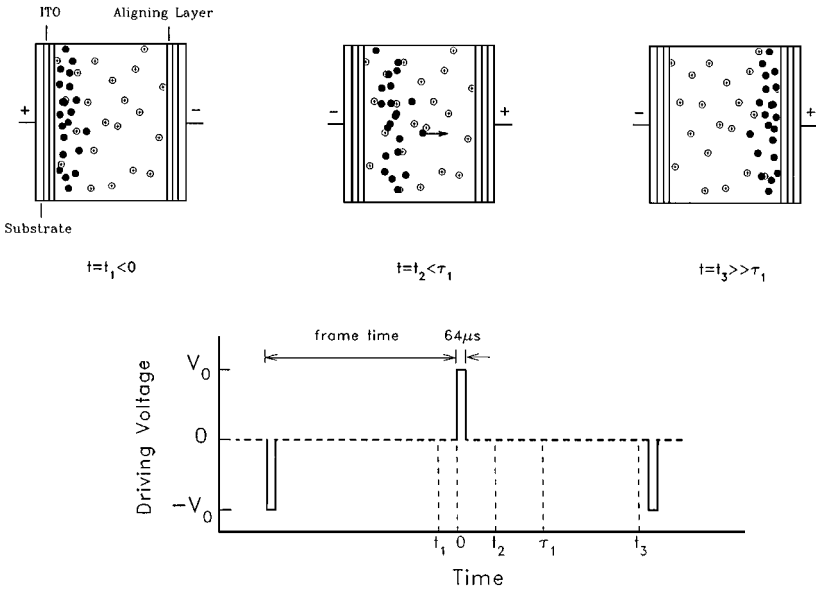


Figure 11 Upper panels: Time-dependent build-up of space charge in an LCD in regime B due to highly mobile residual ions. The low mobile (positive) counter ions are assumed to be stationary within the time frame (lower panel) of the LCD-driving scheme (41).

space-charge effects have to be taken into account when evaluating the electro-optical response and the effective LC resistivity of TFT displays (18, 41).

Figure 12 schematically shows an active matrix addressed TN display (upper left) and the schematic time response $V(t)$ of the voltage across one of its pixels upon application of a pulse V_0 to the LC layer via the source of a thin film transistor (upper right) (18, 37, 41). The video frame rate after which the optical information is refreshed is $T/2 = 20$ ms. The prerequisite for ideal conservation of the optical TN signal during the entire frame time is a constant voltage-holding ratio, $HR = V(T/2)/V_0 = 1$, which corresponds to $\rho_{LC} = \infty$ in Figure 8. However, in actual displays with finite values of ρ_{LC} , and because of the different conductivity regimes A and B, not only the current response differs in the two regimes, but also the time dependence of the holding ratio $V(t)/V_0$ differs (bottom panel). As seen in Figure 12, the holding ratio in regime A obeys the same single exponential decay as the current in Equation 26. However, in the highly resistive TFT regime B, the holding ratio exhibits a biexponential decay. The fast initial decay in Figure 12 is caused by the fast build-up of space-charge in the LC layer (peak in graph B of Figure 10). After the most mobile

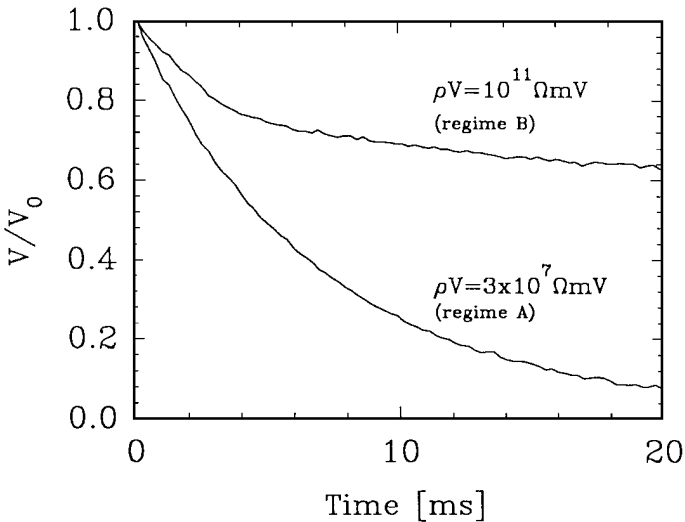
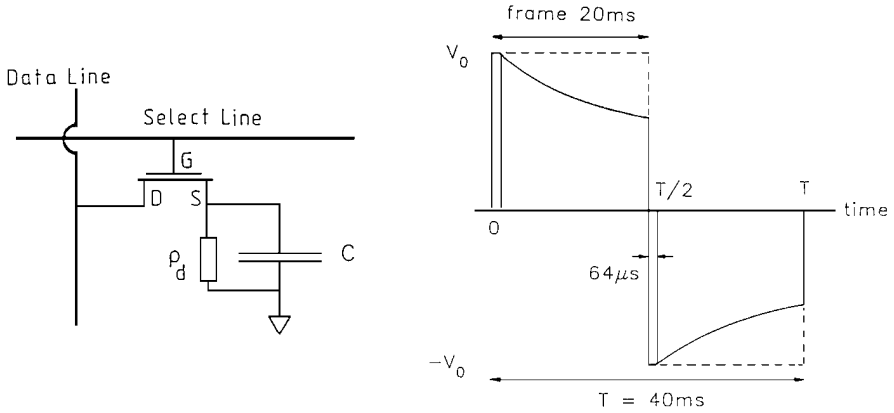


Figure 12 Upper left: Thin film transistor addressed TN display pixel represented by parallel ρ_{LC} and C_{LC} . Upper right: schematic time response of the voltage across C_{LC} during the TV frame time $T/2$ upon application of a voltage pulse V_0 for $64 \mu s$. Bottom: time dependence of the pixel holding ratio V/V_0 in the respective conductivity regimes A and B (18, 41).

residual ions have been removed from the bulk of the LC layer, i.e. the build-up of space-charge is essentially completed, HR decays much more slowly (41). Therefore, the decay of the holding ratio in regime B is less pronounced within the frame time T than in regime A. As a consequence, the decay of the optical signal of the TN display is also less pronounced. From Figure 12 and from the dependence of the holding ratio on specific resistivity and voltage in the product $\rho_{LC}V$, it is seen that large holding ratios in TFT-TN-displays require highly resistive LC materials and that HR also increases with increasing TFT-driving voltage V_0 . Conversely, in LC materials with low-operating voltages requiring large dielectric anisotropies, HR not only decreases because of increasing ion solubility (therefore increased ion contamination of the liquid crystal by the display surfaces), it also decreases because of the decrease of V_0 .

ELECTRO-OPTICAL FIELD-EFFECTS FOR NEMATIC DISPLAYS

Liquid Crystal Field-Effects

An electro-optical liquid crystal field-effect must have the potential to be broadly applicable in displays, to be manufacturable, and to pave the route to new applications. The usefulness of the effect is determined by its own performance and the ability to design liquid crystal materials that fully exploit it. Some applications may require displays based on different effects that require different liquid crystals. Moreover, LCDs have to be competitive with alternative technologies, such as with light-emitting diodes (LEDs), vacuum fluorescent displays (VFDs), plasma display (PLDs), or with cathode ray tubes (CRTs). Therefore, a specific electro-optical effect has to offer competitive advantages such as large contrast between off- and on-state, broad field-of-view, full gray scale and color reproducibility, large design flexibility, compatibility with low power and low-voltage integrated driving circuits, flat design, low weight, reliability, fast response, and operability in transmission as well as in reflection.

Since the beginning of today's nematic field-effect display technology in 1971, a remarkable number of potentially applicable liquid crystal field-effects have been discovered. They are chronologically listed in Table 1 (3).

Until recently, the electro-optical effects used almost exclusively in LCDs are the twisted nematic (TN) effect by Schadt & Helfrich (1), as well as various supertwisted nematic (STN) effects (4–6, 52, 53). The work on STN effects in the 1980s was spurred by the high bias tilt superbirefringence (SBF) effect of Scheffer & Nehring (4). Until recently, the main advantage of STN displays was their considerably lower manufacturing costs compared with TFT-TN-displays. The lower costs were due to the improved multiplexibility of supertwisted

Table 1 Chronology of the discovery of liquid crystal field-effects since 1970

Year	Liquid crystal	Field effect	Reference
1971	TN-LCD	Twisted nematic	1
1971	DAP-LCD	Deformation aufgerichteter Phasen (DAP)	110
1974	GH-LCD	Guest-host	111
1980	SSF-LCD	Surface-stabilized ferroelectrics	112
1983	π -LCD	Pi-cell	113
1984	SBE-LCD	Superbirefringence twisted nematic	4
1985	STN-LCD	Supertwisted nematic	5
1986	PELCs	Polymer encapsulated LCs	114,115
1987	OMI-LCD	Optical mode interference	6
1987	DSTN-LCD	Double-layer supertwisted nematic	52
1987	BW-STN-LCDs	Film-compensated (black- white) supertwisted nematic	53
1988	DHF-LCD	Deformed helix ferroelectrics	116
1988	TSF-LCD	Tristable switching ferroelectrics	117
1989	NSB-LCD	Nematic surface bistability	118
1990	SBF-LCD	Shortpitch bistable ferroelectrics	119
1992		Twisted FLCs	120
1992	IPS-LCD	In-plane switching	121

nematic configurations that renders TFT substrates unnecessary. However, STN displays are slower compared with TN displays; they exhibit a lower contrast, and gray scale is difficult to achieve at high multiplexing rates (18). Although not yet optimal with respect to field-of-view and low-temperature response, thin film transistor addressed TN displays still exhibit the best overall electro-optical performance of all high-information content LCDs. However, because of the nonplanar optics of conventional twisted nematic configurations, which is the cause for their strongly angular dependent viewing properties, there is room for improved displays with more optically planar molecular configurations.

In the following, the principles of twisted nematic and supertwisted nematic displays are reviewed in parallel with their specific LC material requirements, under linearly as well as circularly polarized operating conditions.

Wave-Guiding Operation of Twisted Nematic Liquid Crystal Displays

Today the twisted nematic effect is predominantly used in three display categories: (a) low information content, directly addressed displays such as in car

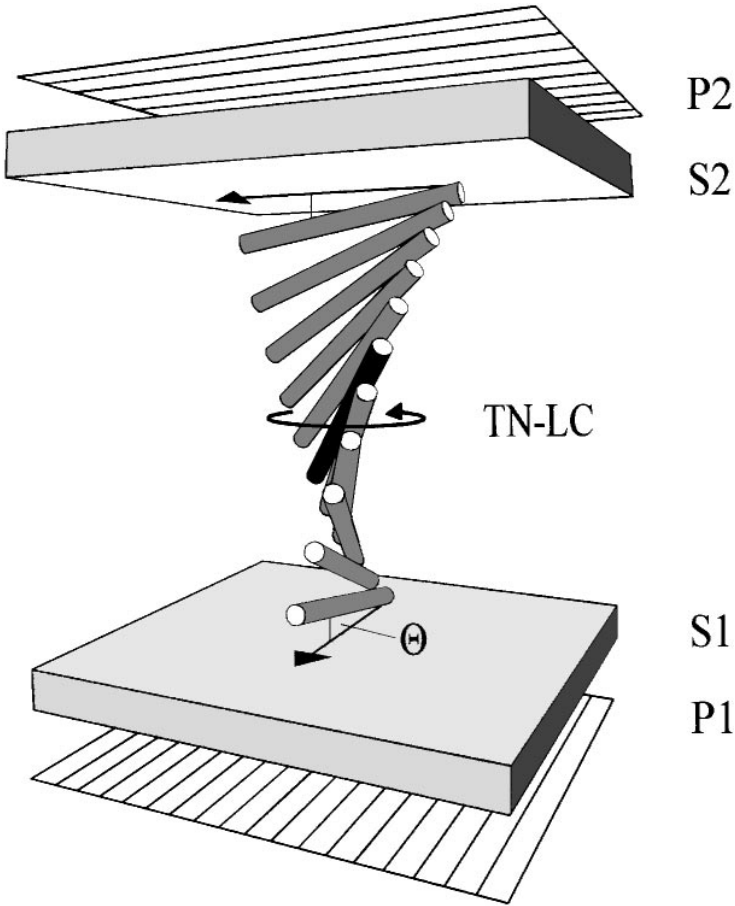


Figure 13 Right-handed twisted nematic liquid crystal director configuration of a partially switched-on TN-LC with crossed linear polarizers P_1 , P_2 at 80% transmission. θ = bias tilt angle at the substrate boundaries S.

dashboards, watches, instrument panels, etc; (b) medium information content, time-multiplexed displays with multiplexing ratios $N \lesssim 32:1$ for calculators, etc; and (c) TFT-addressed, full color, high-end displays with very high information content for direct-view and projection television, computer graphics, etc. At present, virtually all TN displays are operated in their original wave-guiding modes, i.e. with linear input and output polarizers (1).

Figure 13 schematically shows the director configuration of a partially switched-on, conventional, single domain, positive contrast TN display operated in

transmission under wave-guiding conditions (1). Incident, unpolarized light, which is linearly polarized by the entrance polarizer P_1 , is rotated in the off-state by the 90° twisted nematic molecular configuration such that its polarization direction at the upper glass substrate parallels the (crossed) exit polarizer P_2 . In the crossed polarizer configuration of Figure 13, the TN display is transmissive in its off-state. A prerequisite for optimal wave-guiding of linearly polarized light to occur in twisted nematic displays is (1, 38, 54–58)

$$\delta = \Delta n d / 2\lambda = 0.5, 1, 1.5, \dots, \quad 30.$$

where δ is the optical retardation, which the birefringence Δn of the liquid crystal induces over the cell gap d of the TN-LCD; λ = wavelength of incident light.

The voltage-induced change of the transmission between off- and on-state of a TN display results from the combination of the twisted nematic molecular configuration imposed by the display boundaries (Figure 13) and from TN-specific liquid crystal material parameters. Apart from viscosity, crucial LC material parameters are the birefringence, which has to meet Equation 30, the positive dielectric anisotropy $\Delta\varepsilon > 0$, and appropriate elastic restoring forces. Because $\Delta\varepsilon > 0$, the nematic director in the center of the twisted nematic configuration of Figure 13 gradually aligns parallel to the electric field above the threshold voltage $V > V_c$ of the TN display, i.e. perpendicular to the transparent electrode surfaces. Depending on the dielectric anisotropy and the elastic constants of the liquid crystal, the field-induced realignment of the helix typically requires 1–3 V. Realignment only starts above the threshold voltage V_c for mechanical deformation (cf Equation 18), where the elastic restoring forces that stabilize the helical off-state configuration are compensated for by the torque the electric field exerts on the helix. At voltages far above mechanical threshold, pronounced out-of-plane director alignment occurs (Figure 13) that ceases to act as a wave-guide. As a consequence, the crossed polarizer TN configuration in Figure 13 becomes nontransmissive (positive contrast configuration). Aligning the two polarizers in Figure 13 parallel reverses the contrast of the TN display from positive to negative, i.e. the off-state becomes nontransmissive and the on-state becomes transmissive. TN displays are also operable in reflection.

Figure 14 depicts the static transmission-voltage dependence of a positive contrast TN display for different angles ψ of incident light; $\psi = 0^\circ$ = vertical light incidence. The angular dependence of the TN transmission is a consequence of the angular-dependent optical retardation between incident light and TN helix. With a 4×4 matrix approach, Berreman first derived the numerical formalism to determine the transmission-voltage characteristics of TN displays (54). For the special case of vertical light incidence, Schadt & Gerber have shown that the optical threshold voltage V_{90} for 90% transmission of a positive contrast TN display, operated in its second transmission minimum ($\Delta n d / 2\lambda = 1$

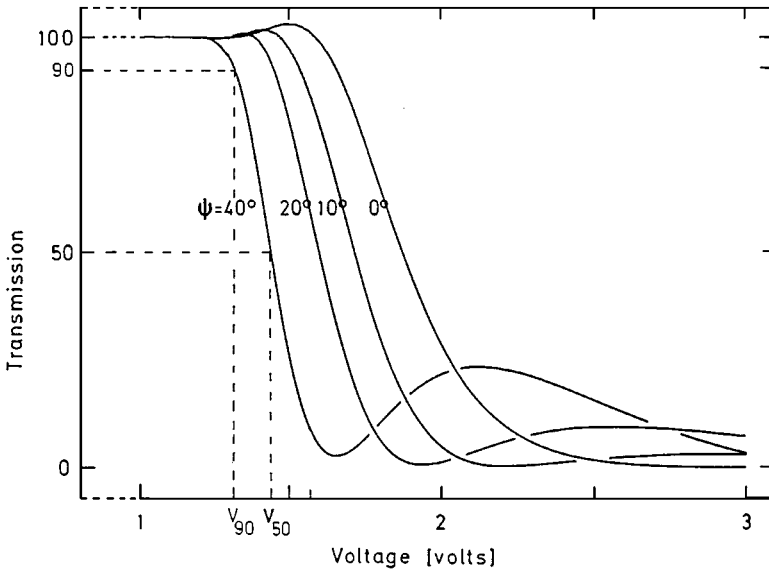


Figure 14 Static transmission-voltage characteristics of a positive contrast TN-LCD operated in its wave-guiding mode at different angles ψ of light incidence; vertical light incidence corresponds to $\psi = 0^\circ$ (70).

in Equation 30), can be approximated by an analytical expression (38)

$$V_{90} \propto V_c \left[2.04 - \frac{1.04}{1 + k_3/k_1} \right] \left\{ 1 + 0.12 \left[\left(\frac{\Delta\epsilon}{\epsilon_\perp} \right)^{0.6} - 1 \right] \right\}, \quad 31.$$

where the threshold voltage V_c for mechanical deformation of the TN helix is given by Equation 18. Equation 31 reflects the dependence of the driving voltage of a TN display on the key LC material parameters. From Equation 31 it follows that the optical threshold in the wave-guiding mode of a TN-LCD primarily depends on the dielectric anisotropy $\Delta\epsilon$ and on the splay, twist, and bend elastic constants of the liquid crystal. Large dielectric anisotropies and/or small elastic expressions $\kappa = [k_1 + (k_3 - 2k_2)/4]$ lead to low thresholds and therefore to low-operating voltages.

Like the optical threshold parameter, the slope parameter α of the transmission-voltage characteristics of TN-displays depend essentially on the dielectric and the elastic constants (38). Small κ values, which lead to steep characteristics, result from low bend/splay elastic constant ratios k_3/k_1 ; whereas flat characteristics that display a large number of gray levels require large k_3/k_1 ratios. This follows in the second transmission minimum and at vertical light incidence from Equation 16.

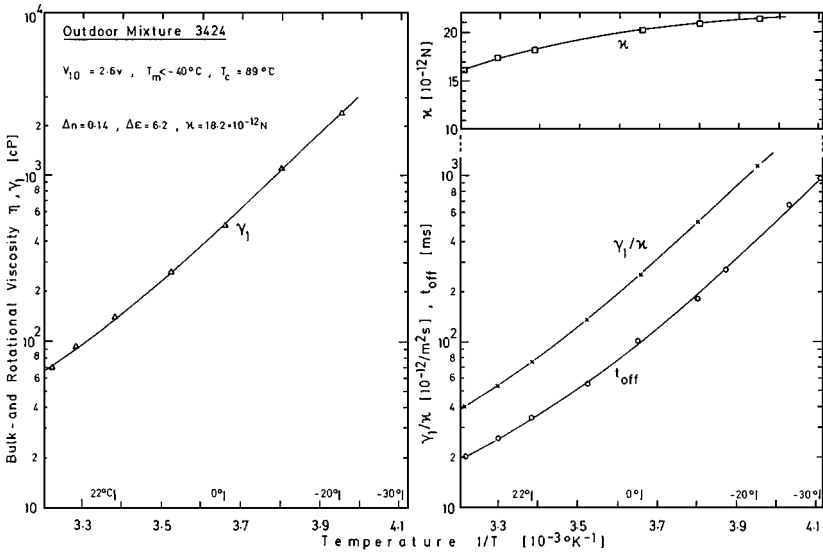


Figure 15 Temperature dependencies of the rotational viscosity γ_1 , the elastic expression $\kappa = [k_1 + (k_3 - 2k_2)/4]$, the visco-elastic ratio γ_1/κ and t_{off} of an early, broad-temperature range liquid crystal mixture 3424 from ROLIC Ltd. t_{off} = TN-LCD turn-off time (70).

Not only the static performance of TN displays, but also their dynamics depends crucially on LC material properties. In a small-angle approximation, Jakeman & Raynes (59) have shown that the turn-on (t_{on}) and the turn-off (t_{off}) times can be approximated by

$$t_{on} \propto \eta d^2 / (\Delta \epsilon E - k \pi^2); \quad t_{off} \propto \eta d^2 / k \pi^2. \quad 32.$$

We have shown that k in Equation 32 equals the elastic expression $\kappa = [k_1 + (k_3 - 2k_2)/4]$, whereas the viscosity η corresponds to the rotational viscosity γ_1 , E = applied electric field, and d = display cell gap (31, 60). Exact solutions for the dynamics of TN displays were first derived by Berreman (61) and by Van Doorn (62). In accord with Equation 32 we have shown (7) that low rotational viscosities γ_1 are not sufficient to achieve short response times in TN displays, but that low visco-elastic ratios $\gamma_1/[k + (k_3 - 2k_2)/4]$ are actually required. Because of the unique elastic properties of alkenyl liquid crystals (Figure 5) and due to their low rotational viscosities, small visco-elastic ratios can be achieved that lead to short response times (7, 16, 17).

Figure 15 shows the temperature dependencies of the LC material parameters γ_1 , κ and γ_1/κ , as well as the corresponding TN display response time t_{off} of an early, broad temperature range LC mixture from ROLIC (63). The strong temperature dependency of t_{off} is mainly due to $\gamma_1(T)$. In agreement with the

above, the temperature dependence of t_{off} in Figure 15 parallels the temperature dependence of the visco-elastic ratio $\gamma_1(T)/\kappa(T)$ of the liquid crystal.

Time-Multiplexing of Liquid Crystal Displays

With an increasing number of pixels in a display, the number of connections eventually becomes so excessively large that addressing each pixel via individual connections is no longer feasible. One way to overcome this problem is to use the steep transmission-voltage characteristics and the well-defined threshold voltage of the electro-optical effect on which the display is based. It was shown by Alt & Pleshko (45) and by Kawakami & Yoneda (46) that both properties are prerequisites for time-multiplexing a matrix type array of display electrodes whose overlapping areas of columns and rows form the pixels. Under ideal conditions, multiplexing reduces the number of connections of a matrix addressed display with N lines and M columns from $(N \times M) \rightarrow (N + M)$.

The maximum optical contrast of a pixel at a given multiplexing ratio depends on the slope of the transmission-voltage characteristics of the display, i.e. on the electro-optical effect on which the display is based and on the effect-specific properties of the liquid crystal material. This follows from the definition of the slope parameter α given above and from Equations 12 and 16. However, as seen in Figure 14 the number of multiplexible lines of a TN display depends not only on the temperature-dependent dielectric, optical, and elastic LC material parameters but also on the angular dependence of the twisted nematic helix resulting from its nonplanar partial on-state (Figure 13). Since the select and the nonselect voltages are determined by the number of multiplexed lines N and by the required pixel contrast, any angular dependence of the transmission-voltage characteristics restricts N and/or the optical quality of the display over its field of view. Prerequisites for high multiplexibility over a broad field of view are therefore displays with weak angular dependence and steep characteristics. An angle-independent slope parameter $\alpha = 0$ in Equation 12 corresponds to an ideal step function that would lead to an infinite number of multiplexable lines with an equally large contrast as a directly addressed display.

Operation of Generally Twisted Nematic Displays with Circularly Polarized Light

Recently we have shown that whereas transmissive and reflective TN displays can be operated in their conventional wave-guiding mode, i.e. with linear polarizers (1), they can also be operated in various circularly polarized modes with left- or right-handed circularly polarized input light, (64, 65). This paragraph outlines some of the interesting features that result from operating generally twisted electro-optical effects, such as parallel-, twisted nematic- and super-twisted nematic displays under circularly polarized light conditions. In combination with cholesteric filters, which act as circular polarizers, we have shown

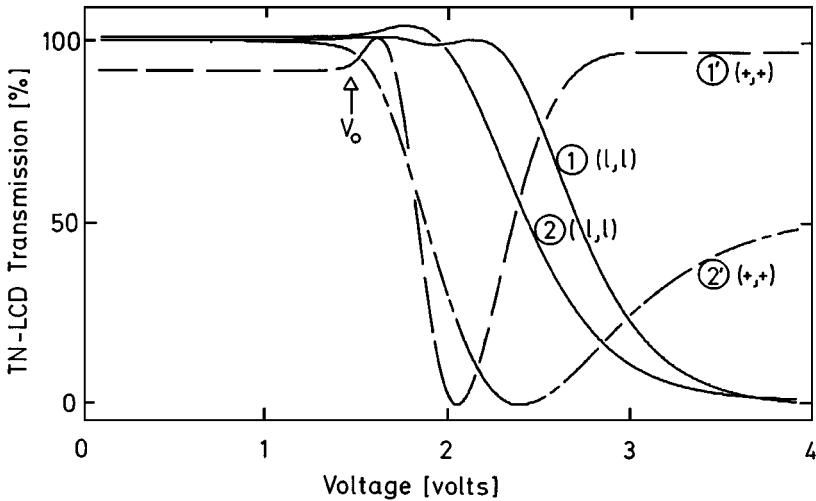


Figure 16 Transmission-voltage characteristics of two different TN-LCDs that are both operated in their wave-guiding modes (graphs 1 and 2) as well as in circularly polarized modes (graphs 1' and 2'). The respective optical retardations are $\delta(\text{TN-LCD } 1) = 1$ and $\delta(\text{TN-LCD } 2) = 0.5$ (51).

that this renders bright and compact direct view and projection configurations feasible (51, 64). Replacing the linear polarizers P_1 and P_2 in Figure 13 by either left- or right-handed circular polarizers leads to a reduction of the optical threshold and to a change of the slope of the transmission-voltage characteristics of the display. This is shown in Figure 16 for two different TN displays (64). TN-LCD(1) is operated in its second (wave-guiding) transmission minimum, whereas TN-LCD(2) is operated in its first minimum. Graph 1' and 2' in Figure 16 are the respective transmission-voltage characteristics of the same displays operated with circular input and output polarizers. The optical threshold V_0 of the circularly polarized configuration of the TN display in Figure 16 was shown to be identical to its mechanical threshold voltage V_c (cf Equation 18 and Reference 64). Figure 16 shows that a threshold reduction of more than 30% results when operating TN displays with circularly polarized light instead of in their classical wave-guiding modes. Moreover, the steepness of the transmission-voltage characteristics of TN displays strongly increases with increasing off-state retardation $\delta = \Delta nd$ under circularly polarized operating conditions, thus increasing their multiplexibility (Figure 16).

Figure 17 shows three different optical configurations of simple, parallel aligned (P)-LCDs in their off-state (51). Figure 17a depicts the conventional, linearly polarized operating mode, where the angles between the nematic

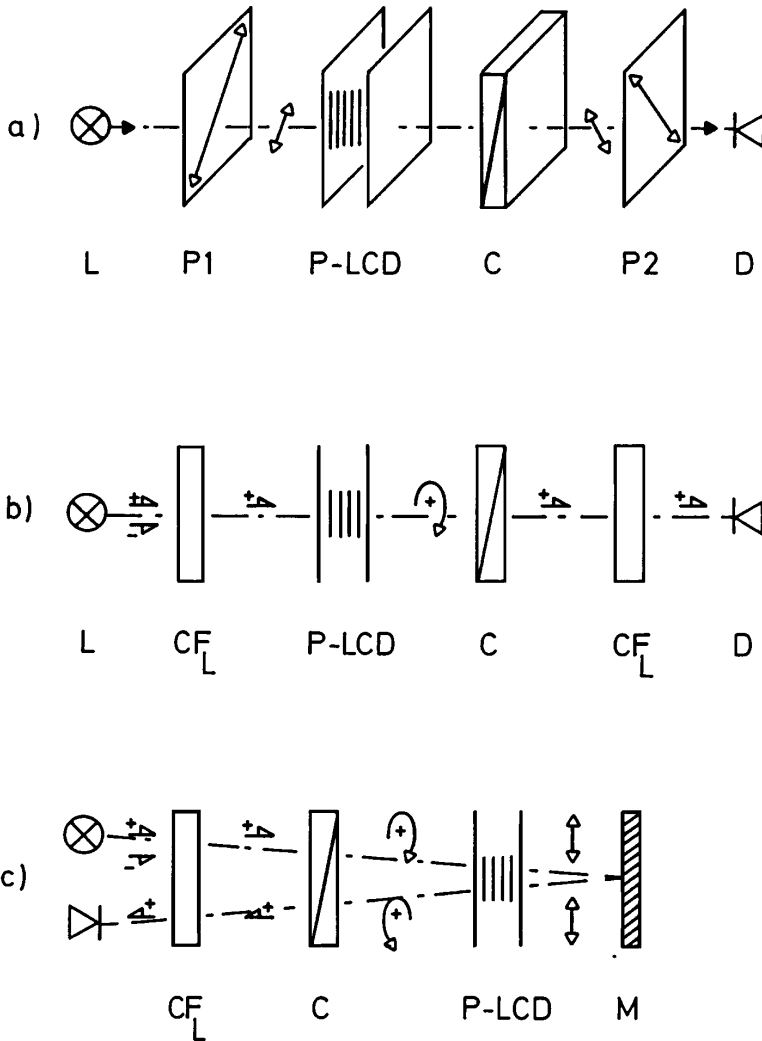


Figure 17 Three different optical configurations of a parallel (P)-LCD in its off-state. Cell gap $d = 8.2 \mu\text{m}$; mixture 7050A from ROLIC Ltd.; L = light source ($\lambda = 530 \text{ nm}$); P₁, P₂ = linear polarizers; C = variable optical retarder; D = photodetector; C_L = left-handed cholesteric filter with maximum selective transmission/reflection at $\lambda_0 = 530 \text{ nm}$; M = metallic mirror (51, 64).

director \hat{n} and the crossed linear polarizers P_1 and P_2 are 45° . To achieve full transmission in the positive contrast off-state, the optical retardation of the P-LCD is fine-tuned with the variable optical retarder C. The configuration in Figure 17*b* is also a positive contrast, transmissive configuration. However, the linear polarizers are replaced by the circular cholesteric polarizers CF_L , which transmit right-handed circularly polarized light (64, 65). The optical off-state retardation $\delta(\text{P-LCD} + \text{C}) = \delta(V = 0)$ of the combination P-LCD and compensator C is adjusted such that $\delta(V = 0) = n\lambda$, $n = 1, 2, \dots$ holds, i.e. right-handed circularly polarized input light is fully transmitted in the off-state (51).

The positive contrast, reflective, circularly polarized operating mode shown in Figure 17*c* requires only one circular polarizer CF_L . The optical off-state retardation of the P display is adjusted with compensator C such that $\delta(V = 0) = \lambda/4(2n + 1)$, with $n = 0, 1, \dots$. This converts right-handed circularly polarized input light in front of the metallic reflector M into a linearly polarized output. For symmetry reasons and because linear polarization does not change upon reflection on M, the reflective configuration (Figure 17*c*) is transmissive in the off-state. Due to the large optical anisotropy of the LC mixture in the P display and due to the rather large cell gap $d = 8.2 \mu\text{m}$ (51), large degrees of order n result for $\delta(V = 0) = \lambda/4(2n + 1)$. Therefore, small nonsymmetries in the optical retardation of incident and reflected beam already lead to deviations from $\delta(V = 0) = \lambda/4(2n + 1)$, thus reducing the contrast. Consequently, a well-collimated optics has to be used when applying this operating mode to LCD projectors (66).

Graph 2 and 3 in the upper part of Figure 18 are the respective transmission-voltage characteristics of a P display recorded in conventional (graph 2) and circularly polarized modes (graph 3) as depicted in Figure 17*a, b* (51). The dashed graph 1 in Figure 18 is a recording of the normalized voltage-induced change of capacitance $\Delta C/C_\perp \propto \Delta\varepsilon/\varepsilon_\perp$ of the P display. $\Delta C(V)/C_\perp$ is proportional to the field-induced deformation of the nematic layer. Graph 4 in the lower part of Figure 18 shows the reflection of the P display versus voltage in the configuration of Figure 17*c*. From graphs 2 and 3 in Figure 18 it follows that the circularly and the linearly polarized operating modes of Figure 17*a* and *b* lead in the case of P-LCDs, except for a difference in phase shift of $\lambda/4$, to identical characteristics. Moreover, (see Figure 17*a*) all three P display operating modes exhibit identical optical thresholds that correspond with the (capacitive) threshold for mechanical deformation of the P display of graph 1 (51). The threshold voltage for mechanical deformation of a P display is (67)

$$V_F = \pi [k_1/\varepsilon_o \Delta\varepsilon]^{1/2}. \quad 33.$$

Apart from this agreement, it is interesting to note the steep initial transmission-voltage characteristics of graphs 2 and 3 in Figure 18. They are due to the

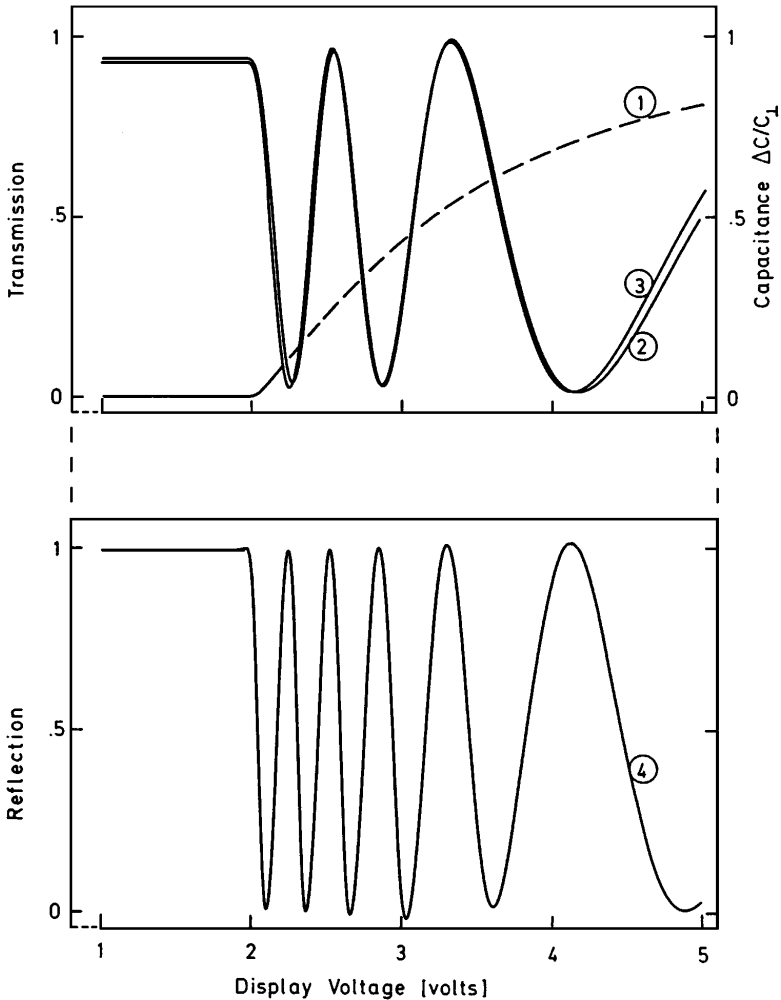


Figure 18 Transmission-voltage (graphs 2 and 3) and reflection-voltage characteristics (graph 4) of a P-LCD corresponding to the operating modes depicted in Figure 17 $\Delta C(V)/C_{\perp}$ = voltage-induced capacitance change of the P-LCD (graph 1) (51).

small elastic constant ratio $k_3/k_1 = 0.99$ and the large birefringence $\Delta n = 0.225$ of the LC mixture (51).

Operating P displays in reflection instead of transmission increases the initial slope still further (cf graph 4 in Figure 18). From graph 4 and Equation 12 we see that the steep slope allows multiplexing the reflective P display with as many as $N = 420$ lines at vertical light incidence and a contrast ratio of 5:1.

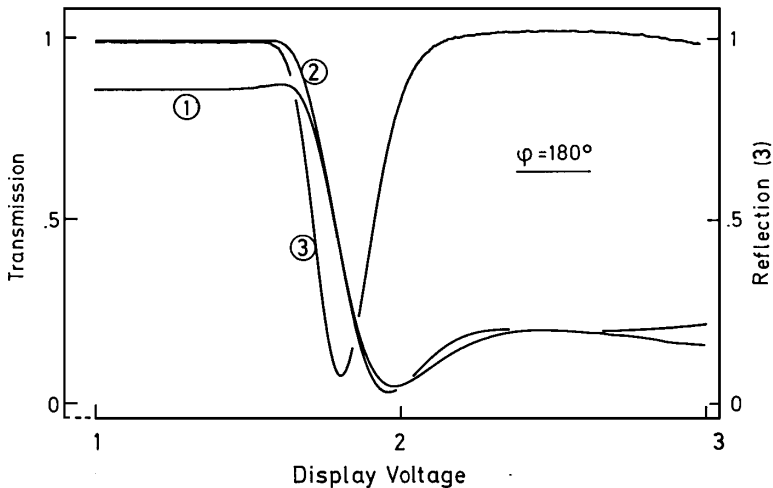


Figure 19 Electro-optical characteristics of a $\phi = 180^\circ$ super-twisted STN-LCD operated in its conventional linear transmissive mode (graph 1), as well as in a circularly polarized reflective mode analogous to Figure 17 (graph 2) and in the circularly polarized reflective mode analogous to Figure 17 (graph 3) (51).

We have shown that twisted display configurations operating with circular polarizers exhibit steeper transmission-voltage characteristics and are brighter than their conventional counterparts with linear polarizers (51). Figure 19 shows the transmission of a $\phi = 180^\circ$ twisted STN-LCD operated in its conventional mode with two linear polarizers (graph 1), in its circular mode with two circular polarizers (graph 2), and in a reflective circular mode with only one circular polarizer (graph 3) (51). The transmissive and reflective circularly polarized STN-displays are $\sim 20\%$ brighter than conventional STN-LCDs.

Except for additional reflection losses, no changes in the electro-optical characteristics occur between transmissive and reflective operation of conventional STN-LCDs, i.e. in STN displays with linear entrance and exit polarizers. Specifically the slope of the electro-optical characteristics of conventional STN displays and their multiplexibility are identical in transmission and in reflection. We have shown that this invariance can be broken by operating STN displays in a reflective circularly polarized configuration (51). In such a configuration, full use is made of the field-induced optical retardation properties of the STN helix on incident and reflected beam. The overall effective optical retardation of the super-twisted helix doubles. As a consequence, considerably steeper electro-optical characteristics and therefore two to three times improved multiplexibility result. This is shown by graph 3 of Figure 19 (64, 65).

We have shown that the optical threshold voltages of all circularly polarized operating modes are identical with the thresholds for mechanical deformation of generally twisted nematic field-effects (37, 51). From the equation that describes the threshold voltage V_c of mechanical deformation of arbitrarily twisted nematic configurations (34) the optical threshold voltage of generally twisted nematic configurations therefore follows as (51):

$$V_t = \pi \left\{ [k_1 + (k_3 - 2k_2)(\phi/\pi)^2] / \varepsilon_0 \Delta \varepsilon + 2k_2(\phi/\pi)(2d/P_0) \right\}^{1/2}, \quad 34.$$

where ϕ = twist angle, and P_0 = helical pitch of the liquid crystal. For $\phi = 0$ and $P_0 = \infty$, Equation 34 reduces Equation 33, and for $\phi = 90^\circ$, $P_0 = \infty$ Equation 34 becomes Equation 18.

LIQUID CRYSTALS FOR THIN FILM TRANSISTOR ADDRESSED TWISTED NEMATIC DISPLAYS

We have shown (7, 37) that the introduction of double bonds at specific side chain positions considerably extends the range of material properties of liquid crystals. The elastic constants, the splay/bend elastic constant ratio k_3/k_1 , the visco-elastic ratio γ_1/κ , the rotational viscosity γ_1 , the elastic expression $\kappa = [k_1 + (k_3 - 2k_2)/4]$, and the mesomorphic temperature ranges, as well as the dielectric and the optical anisotropies, are especially affected. Moreover, synergies were shown to result from combining different rigid molecular cores comprising aromatic or non-aromatic rings with alkenyl side chains (7, 37). As a consequence, the performance of TN, STN, and ferroelectric LCDs considerably improves. In the following, some thin film transistor (TFT)-compatible nematics whose properties illustrate the synergies that can be achieved between selective functional molecular elements are reviewed. The liquid crystals exhibit low viscosities, and they cover a broad range of dielectric and optical anisotropies combined with pronounced nematic phases. Moreover, the compounds exhibit large specific resistivities ρ_{LC} and low solubilities for residual ions from boundary aligning layers in displays, which lead to large holding ratios (see above). Some of the structural elements investigated in this context and their (additive) nomenclature are depicted in Figure 20 (see Reference 7).

Figure 20 depicts different halogenated TFT-alkenyl liquid crystals (developed in our laboratories; 16, 37), as well as the saturated reference compound 3CCP_FF (68). Permanent dipole moments essentially determine the desired positive dielectric anisotropies of the different molecular structures. The proper introduction of dioxane rings with their oxygen moments serves the same purpose. Medium to large optical anisotropies result from aromatic structural elements such as benzene rings and C≡C-bonds (tolanes). To render comparisons as relevant as possible, all of the (short) alkyl and alkenyl side chains in Figure 20

Nomenclature	Structure	$T_m/^\circ\text{C}$	$T_c/^\circ\text{C}$	$\Delta\varepsilon (T_c-10^\circ\text{C})$
$1d_1\text{CCPF}$ (ref)		105	194	1.76
$3\text{CCP}_F\text{F}$		46	114	3.10
$1d_1\text{CCP}_F\text{F}$		49	159	3.22
$1d_1\text{CPP}_F\text{F}$		98	134	4.04
$1d_1\text{CCP}_F\text{Cl}$		91	197	2.91
$1d_1\text{CCAP}_F\text{F}$		64	137	2.73
$1d_1\text{DCP}_F\text{Cl}$		82	144	10.0
$3\text{CP}_{FF}\text{P}_F\text{F}$		80	-2	-
$3\text{CP}_{FF}\text{TP}_F\text{F}$		71	123	6.6
$1d_1\text{DP}_{FF}\text{TP}_F\text{F}$		99	157	20.8

Figure 20 Structures of reference nematics (top three) and halogenated nematic TFT liquid crystals of ROLIC Ltd. T_m , T_c are melting and clearing temperatures. The dielectric anisotropy $\Delta\varepsilon = (\varepsilon_{\parallel} - \varepsilon_{\perp})$ is determined at the respective reduced temperature ($T_c - 10^\circ\text{C}$) constant of the individual compounds (37).

contain three carbon atoms. The systematic structural changes that lead to the desired synergies are designated from top to bottom by dashed squares (Figure 20). The three top structures, $1d_1\text{CCPF}$, $1d_1\text{CCP}_F\text{F}$, and $3\text{CCP}_F\text{F}$, serve as references. Comparison of the nematic-isotropic transition temperatures T_c of the first five, directly linked molecules at the top of Figure 20 shows that the introduction of a double bond d in 1-position from the rigid core, i.e. in position d_1 , increases T_c by $\sim 45^\circ\text{C}$. Another strong increase of $\sim 35^\circ\text{C}$ results from replacing the para fluorine F with chlorine Cl; whereas lateral fluorination depresses T_c by

$\sim 35^\circ\text{C}$. Depression of T_c also results from replacing the central cyclohexane ring C with a benzene ring P, which demonstrates that the introduction of double bonds in proper side chain positions and the replacement of para fluorine by chlorine strongly increase T_c . This synergy was used in the design of $1d_1\text{DCP}_F\text{Cl}$ (Figure 20) for compensating the T_c -depressing tendencies of its dioxane ring and its lateral F (16). As expected, the replacement of para fluorine by Cl reduces the dielectric anisotropy $\Delta\varepsilon$ only slightly (Figure 20).

We have shown that the proper distribution of molecular structural elements with rather small individual permanent dipole moments at different molecular sites leads to large dielectric anisotropies and reduces the ion solubility of liquid crystals (16). The para-chlorinated compound $1d_1\text{DCP}_F\text{Cl}$ (in Figure 20) with $\Delta\varepsilon = 10$ is an example of our design approach.

The last three compounds of Figure 20 comprise the dilaterally fluorinated benzene ring P_{FF} , whose permanent C–F-moments contribute to the positive dielectric anisotropy of the terminal ring P_FF . Sterically decoupling the two rings P_{FF} and P_FF by a tolane group leads to a pronounced nematic phase. Moreover, this leads to a strong increase of T_c by 128°C (cf $3\text{CP}_{\text{FF}}\text{P}_F\text{F}$ and $3\text{CP}_{\text{FF}}\text{TP}_F\text{F}$ in Figure 20). Compared with $1d_1\text{CPP}_F\text{F}$, the dielectric anisotropy of $3\text{CP}_{\text{FF}}\text{TP}_F\text{F}$ increases by $\sim 60\%$. Replacing the cyclohexane ring C in $3\text{CP}_{\text{FF}}\text{TP}_F\text{F}$ with an optically comparable isotropic dioxane ring D with its oxygen dipole moments further increases $\Delta\varepsilon$ by a factor of three without increasing Δn (Figure 20).

Table 2 shows the optical, dielectric (static), elastic, and viscous properties of binary mixtures comprising the compounds of Figure 20. Also depicted are the twisted nematic threshold voltages V_{10} determined in $6\ \mu\text{m}$ twisted nematic displays. A summary of the measuring techniques is given in Reference 7. In those cases where the melting temperatures are above 22°C , extrapolated values are used. Except for the rotational viscosity γ_1 and the bulk viscosity η , the material parameters and V_{10} in Table 1 scale with the nematic order parameters $S(T)$ (7). Therefore, comparisons of Δn , $\Delta\varepsilon$, k_{33} , k_{11} , κ , and V_{10} are made at constant reduced temperature $T/T_c = 0.8$; γ_1 and η are compared at 22°C . M1 and M2 in Table 2 each consist of the low-viscous, mono- and difluoro homologous alkenyls described above (cf Figure 20, Reference 16). M1 and M2 are typical representatives of their respective liquid crystal class and serve as references. M3 and M6 also are made up of homologues, whereas the other mixtures each comprise 50% of the common reference compound $\emptyset d_1\text{CCP}_F\text{F}$ used in M2.

From Table 2 we see that (a) large dielectric anisotropies and rather low elastic expressions κ are achieved with $1d_1\text{DP}_{\text{FF}}\text{TP}_F\text{F}$ (M7). Both parameters strongly reduce the threshold voltage of twisted nematic liquid crystal displays (Equation 17). (b) The low rotational viscosity γ_1 of directly linked $Xd_1\text{CCP}_F\text{F}$

Table 2 Material data for binary mixtures of the halogenated nematics depicted in Figure 20^a

LC mixture		Δn	$\Delta \varepsilon$	k_3/k_1	$\kappa/10^{-12} \text{ N}$	γ_1/cP	η/cP	V_{10}/V	$T_c/^\circ\text{C}$
($0d_1\text{CCPF}$, $1d_1\text{CCPF}$)	M1	0.095	2.44	3.2	15	25	3.6	3.5	168
50 mol 50									
($0d_1\text{CCP}_F\text{F}$, $1d_1\text{CCP}_F\text{F}$)	M2	0.093	5.34	3.0	12	53	8.1	2.2	133
50 50		0.098	6.34	3.1	14	155	23	2.1	
($0d_1\text{CCP}_F\text{Cl}$, $1d_1\text{CCP}_F\text{Cl}$)	M3	0.121	4.52	2.9	17	40	4.2	3.0	172
50 50									
($0d_1\text{CCP}_F\text{F}$, $1d_1\text{CCAP}_F\text{F}$)	M4	0.091	4.79	2.9	13	71	9.1	2.4	123
50 50		0.095	5.47	3.1	14	165	23	2.3	
($0d_1\text{CCP}_F\text{F}$, $1d_1\text{DCP}_F\text{F}$)	M5	0.091	13.4	2.4	11	138	21	1.4	103
50 50		0.092	14.0	2.4	11	178	27	1.4	
($0d_1\text{CPP}_F\text{F}$, $1d_1\text{CPP}_F\text{F}$)	M6	0.170	6.70	2.1	11	~150	~15	2.2	105
50 50		0.172	6.90	2.1	12	~210	~20	2.2	
($0d_1\text{CCP}_F\text{F}$, $1d_1\text{DP}_{FF}\text{TP}_F\text{F}$)	M7	0.167	24	2.1	10	95	14	1.1	117
50 50		0.172	27	2.2	11	207	25	1.1	

^aData in bold type were determined at $T/T_c = 0.8$, the others at $T = 22^\circ\text{C}$. Optical anisotropy $\Delta n = (n_e - n_o)$; dielectric anisotropy $\Delta \varepsilon = (\varepsilon_{\parallel} - \varepsilon_{\perp})$; splay/bend elastic ratio k_3/k_1 ; elastic expression $\kappa = [k_1 + (k_3 - 2k_2)/4]$; rotational viscosity γ_1 ; bulk viscosity η ; nematic-isotropic transition temperature T_c .

compounds hardly increases when replacing $1d_1\text{CCP}_F\text{F}$ in M2 with the ethane linked $1d_1\text{CCAP}_F\text{F}$ (M4) or with the considerably more polar $1d_1\text{DCP}_F\text{F}$ (M5). (c) Despite the fact that $1d_1\text{DP}_{FF}\text{TP}_F\text{F}$ strongly reduces the threshold voltage V_{10} , the rotational viscosity γ_1 of M7 remains surprisingly small. Both, the large dielectric anisotropy and the low γ_1 of M7 indicate that lateral difluoro-substitution leads in the case of $1d_1\text{DP}_{FF}\text{TP}_F\text{F}$ to a suppression of antiparallel molecular association (69). The same mechanism is likely to contribute to the large $\Delta \varepsilon$ and the low γ_1 of $1d_1\text{DCP}_F\text{F}$ in M5. (d) An increase of the optical anisotropy by $\sim 20\%$ results when replacing para-fluorine with chlorine (cf M2, M3). (e) The conjugated core $\text{P}_{FF}\text{TP}_F\text{F}$ in $1d_1\text{DP}_{FF}\text{TP}_F\text{F}$ strongly increases the optical anisotropy to values exceeding those of pure biphenyls (cf M6, M7; note the 100% biphenyl contribution PP in M6 and only 50% contribution in M7).

DEPENDENCE OF SUPERTWISTED NEMATIC DISPLAYS ON LIQUID CRYSTAL MATERIAL PARAMETERS

Supertwisted Nematic Displays

Even if TN displays are operated with LC materials, which exhibit ideally low bend/splay elastic ratios $k_3/k_1 = 0.5$ (Figure 5), their transmission-voltage characteristics remain rather flat (Equation 16, Reference 7), which limits the

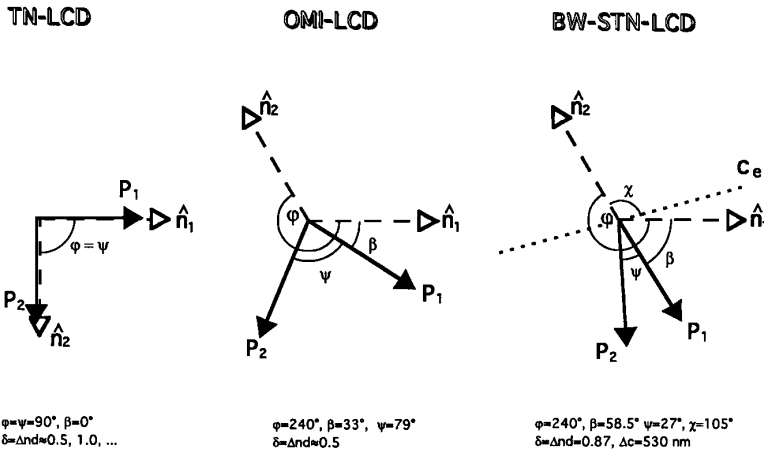


Figure 21 Geometries of twisted nematic (TN), optical mode interference (OMI) and black-white supertwisted nematic (BW-STN)-LCDs \hat{n}_1, \hat{n}_2 , boundary aligning directions on the two substrates; P_1, P_2 , linear polarizing directions; ϕ = twist angle; θ = bias tilt angle; χ , angle of the slow optical axis c_e of the compensating film c whose optical retardation is Δc (70).

multiplexibility of conventionally addressed TN displays to about 32 lines. To overcome this limitation, there are essentially three different approaches that can be pursued: (a) addressing each pixel via in situ drivers, (b) using electro-optical effects with inherently steep transmission-voltage characteristics and therefore improved multiplexibility, or (c) use of bistable electro-optical effects with inherent optical memory. The TFT-addressing approach (a) is commercially realized in high-end TN displays, whereas (b) makes use of the steep characteristics of STN-LCDs.

Figure 21 schematically shows the geometries of three black-white nematic display configurations: a TN-display (1), an optical mode interference (OMI) display (6, 71), and a BW-STN display (4, 5). BW stands for the black-white appearance of STN displays, which results from compensating the yellow off-state of the display by an optical retardation film c (72), whose slow optical axis c_e is dashed and whose optical retardation is Δc (Figure 21). The OMI and the BW display geometries depicted in Figure 21 operate with $\phi = 240^\circ$ twist and bias tilt angles $\theta = 5^\circ$ (3, 70). Instead of using an optical retarder film to compensate the yellow STN off-state, a second, non-addressed STN-LCD can be superimposed on an STN display such that the resulting double layer STN configuration appears black and white (72).

In Figure 22 the transmission-voltage characteristics of an OMI display with 180° twist and 90° twisted TN display at different angles ψ of light incidence are

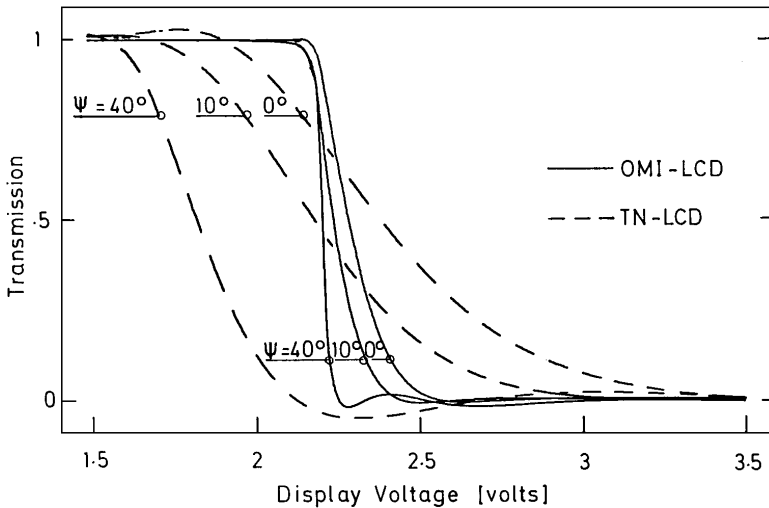


Figure 22 Transmission-voltage characteristics of a TN-LCD and an OMI-LCD at different angles ψ of incident light. At vertical light incidence $\psi = 0^\circ$. $\phi = 90^\circ$ (TN); $\phi = 180^\circ$ (OMI) (7).

compared. To exclude LC material effects, both displays have the same liquid crystal mixture (70). If another supertwisted nematic display configuration with the same twist angle had been chosen for comparison, the scaling of the slopes would have been similar. Figure 22 shows the steeper transmission-voltage characteristics and the strongly reduced angular dependence of OMI displays compared with TN displays.

Like TN displays performance, optimal electro-optical performance of supertwisted configurations requires liquid crystals whose properties are tuned to the specific electro-optical effect and its application. Figure 23 shows the influence of the elastic and dielectric properties on the slope parameter α of the transmission-voltage characteristics of two supertwist configurations with identical twist angles $\phi = 180^\circ$ (OMI and STN); also shown are the characteristics of two 90° twisted TN displays (7). The TN displays are operated in their respective first and second transmission minimum. We calculated the correlations depicted in Figure 23 for vertical light incidence and for a constant twist/splay elastic constant ratio $k_2/k_1 = 0.4$ (7). Figure 23 illustrates that both the STN- and OMI-supertwist configurations strongly reduce the slope parameters α (Equation 12). Increasing the twist further leads to a further reduction of α but also to a slower response (18) and eventually, at infinitely steep slopes, to fingerprint dislocations in supertwisted displays (18). From Figure 21 and Equation 12 it follows that supertwist configurations increase the number of

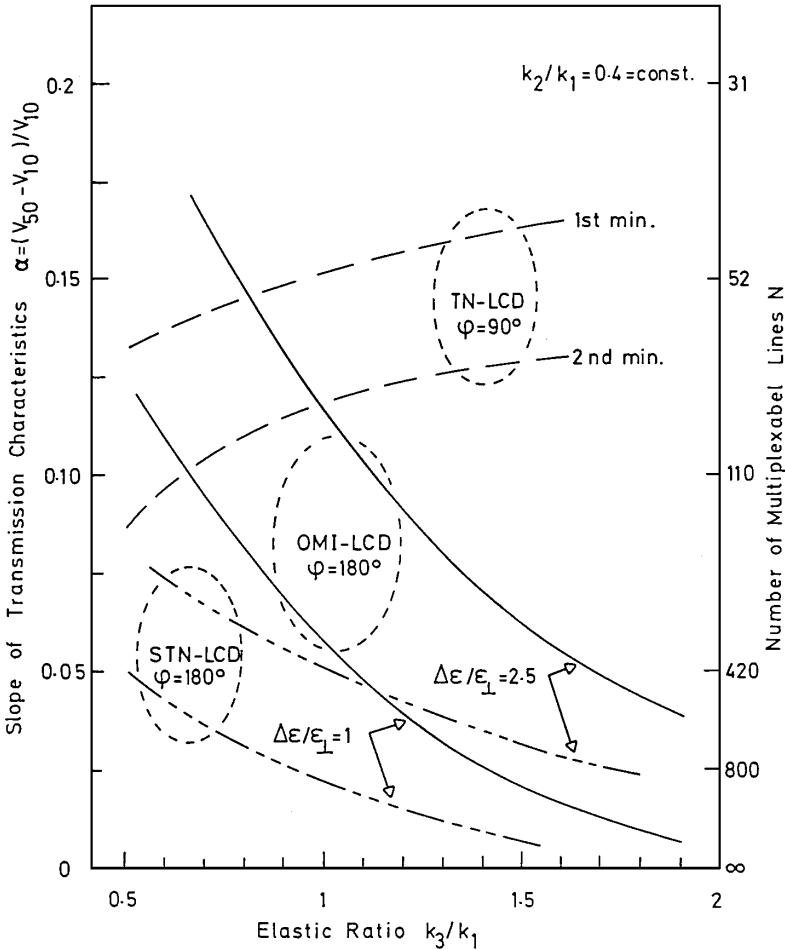


Figure 23 Calculated dependence of the slope parameter α of TN-LCDs, STN-LCDs, and OMI-LCDs versus liquid crystal material parameters k_3/k_1 and $\Delta\epsilon/\epsilon_{\perp}$ at vertical light incidence. The following parameters were used: twist angle $\phi = 180^\circ$ for STN- and OMI-LCDs; $\phi = 90^\circ$ for TN-LCDs; Δn (STN) = $0.95 \mu\text{m}$; Δn (OMI) = $0.50 \mu\text{m}$; $k_2/k_1 = 0.4 = \text{constant}$ (7).

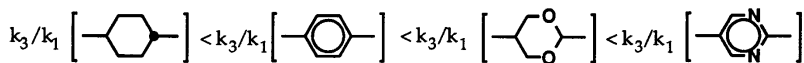
multiplexible lines by more than one order of magnitude compared with TN displays; whereas Figure 23 shows that prerequisites to achieve this performance are LC materials with large elastic constant ratios k_3/k_1 , and/or small dielectric ratios $\Delta\epsilon/\epsilon_{\perp}$. However, the combination of the two, i.e. small $\Delta\epsilon$ and high multiplexing rates, leads to an increase of the operating voltage, which at high multiplexing rates easily exceeds the capacity of display drivers. This

follows from the consequent increase of the select voltage V_s with increasing multiplexing rate N (Equation 12) and from the increase of the mechanical and the optical threshold voltage V_t of supertwist configurations with decreasing $\Delta\varepsilon$ (Equation 34).

The way out of this multiplexing dilemma is to have liquid crystals with large elastic constant ratios k_3/k_1 (the opposite is required for TN displays) and large $\Delta\varepsilon$. We have shown that polar alkenyls with their double bonds in odd side chain positions (such as Xd_3CP ; see top structure in Figure 5) ideally combine both properties (7, 17). Our alkenyls have become key components in all mixtures used today by liquid crystal manufacturers for high-information content STN and OMI displays.

Odd-Even Effects in Alkenyls: Molecular Modeling and Influence of Molecular Structural Elements on TN and STN Display Performance

Large bend/splay elastic constant ratios k_3/k_1 are prerequisite for realizing high multiplexing rates with STN displays, whereas the opposite is true for TN displays. In the early 1980s, we found k_3/k_1 of nematics to depend on the polarity of LC molecules and on the type of rings used in their rigid cores (38). Heterocyclic rings, such as those of pyrimidine or dioxane, were shown to induce small k_3/k_1 ratios, whereas cyclohexane rings increased k_3/k_1 compared with benzene rings. The following order was found (38).



Moreover, for a given rigid core, the ratio k_3/k_1 decreases with decreasing molecular polarity, i.e. with decreasing dielectric anisotropy (38). Examples for small elastic ratios that can be achieved from combining heterocyclic cores and low molecular polarity are two-ring pyrimidines or two-ring dioxanes with (nonpolar) hydrocarbon side chains (see Figure 5) (38, 63). From the definition of the elastic expression κ in Equations 17, 18, and 31, it follows that not only k_3/k_1 is affected by these synergies but also κ . Therefore, as a result of low k_3/k_1 values (Equations 12, 16), the multiplexibility of TN displays improves. Also the threshold voltage does not increase to the extent expected from the reduction of the dielectric anisotropy alone (Equations 17, 18) (38). As a result of such synergies, multiplexible LC materials with TN threshold voltages below 1 V became feasible in the early 1980s (74). Moreover, it was evident that the large variations among the elastic constants of different LCs did not justify assuming equal elastic constants $k_1 = k_2 = k_3$; an assumption often used in mean field theories. In this context, we presented the first examples of molecular structures

with identical length/width ratios (L/W) but with considerably different elastic constant ratios k_3/k_1 (17, 38). Our findings showed that hard-rod models, which imply $L/W \propto k_3/k_1$, are inadequate to describe the actual elastic properties of nematic liquid crystals.

It is obvious that a broad range of liquid crystal properties is required for realizing the often contradictory requirements of different electro-optical effects and different display applications. Alkenyl liquid crystals with their pronounced odd-even dependence of material properties on double bond position are ideally suited to cover these requirements (7, 17). Figure 24 summarizes the alkenyl position-dependent odd-even influence on the dielectric anisotropy $\Delta\epsilon$, the optical anisotropy Δn , the elastic expression κ , and the bend/splay elastic constant ratio k_3/k_1 in isothiocyanate alkenyls (75). The odd-even effects of Figure 24, which are characteristic of alkenyl liquid crystals, increase $\Delta\epsilon$, Δn , κ , and k_3/k_1 in odd double bond positions, whereas even double bond positions cause these material properties to decrease (Figure 24). An example for this strong odd-even effect is the small elastic constant ratio k_3/k_1 ($\emptyset d_4\text{CP}$) ~ 1.5 compared with k_3/k_1 ($1d_3\text{CP}$) ~ 3 in Figure 5.

From finding that the L/W ratio of individual molecules is not directly related with k_3/k_1 the question arose as to whether a correlation between k_3/k_1 and the L/W ratio of the equilibrium position of ensembles of molecules would exist. Semiquantitative investigations of molecular equilibrium configurations with interactive molecular modeling were performed based on inter- and intramolecular van der Waals interactions and conformational torsional potentials; Coulomb interactions were not taken into account (7). The results confirmed our experimental findings that the L/W ratio of individual alkenyl molecules cannot be related to the macroscopically defined elastic ratios k_3/k_1 . We then selected alkenyl structures with identical L/W ratios but with different elastic constant ratios k_3/k_1 , $1d_3\text{CP}$ and $\emptyset d_4\text{CP}$ (Figure 5) (7). The question was whether shifting the double bond from the odd $1d_3$ -position into the even $\emptyset d_4$ -position would affect the shape of the respective pairs. Figure 2 shows the calculated equilibrium configuration for two antiparallel aligned cyanophenylcyclohexane molecules $1d_3\text{CP}$ (Figure 5). As with single molecules, the L/W ratio of the equilibrium pair configuration in Figure 2 hardly changes when shifting the double bond into different side chain positions. We therefore chose a two-dimensional macroscopic molecular ensemble consisting of twelve cyano-phenylcyclohexane alkenyl molecules of the $1d_3\text{CP}$ type with a preferred starting alignment direction of the long molecular axes (7). Figure 25 shows the calculated equilibrium configurations of two different ensembles. The van der Waals radii are indicated by dots. The upper ensemble (blue) consists of $1d_3\text{CP}$ alkenyls whereas the lower ensemble (orange) consists of $\emptyset d_4\text{CP}$ alkenyls (Figure 5). It is interesting to see in Figure 25 that remarkably different L/W

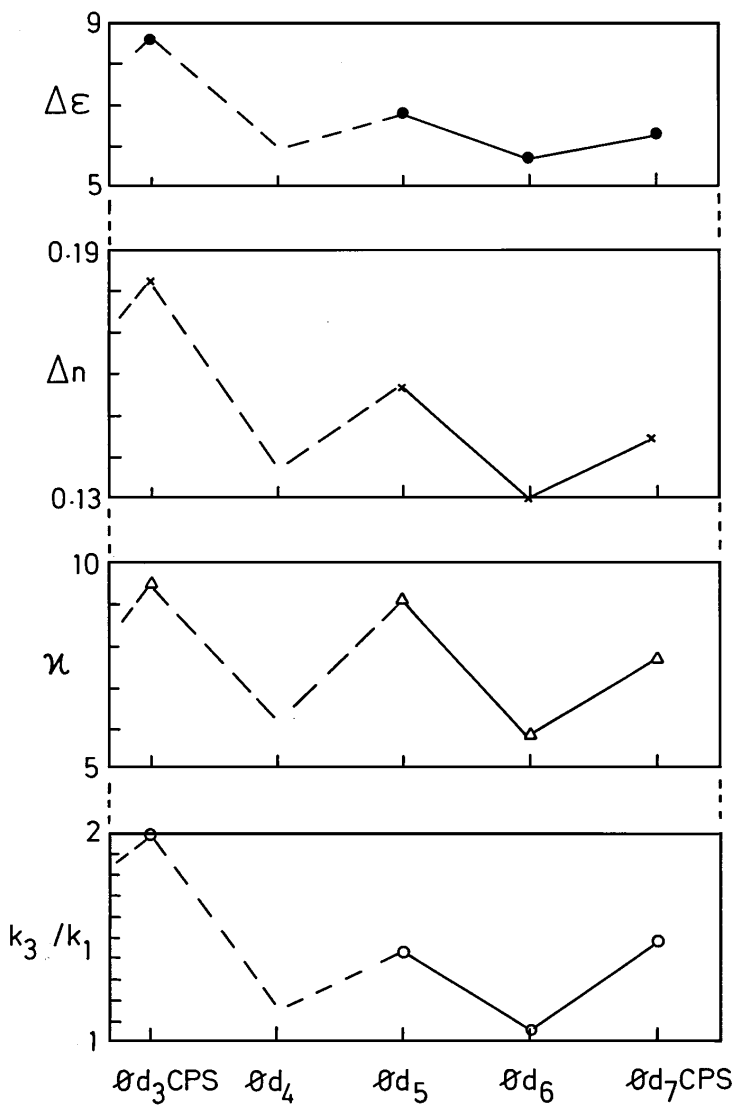


Figure 24 Alkenyl position-dependent odd-even effects within the homologous series of θd_i CPS ($i = 3, 4, 5, 6,$ and 7) for k_3/k_1 , κ , $\Delta\epsilon$, and Δn (75).

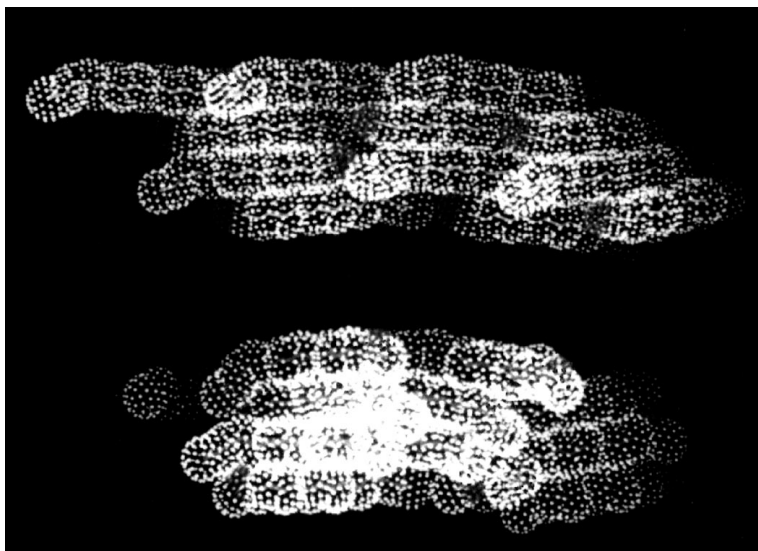


Figure 25 Calculated most probable equilibrium configurations of ensembles of alkenyl liquid crystal molecules of the type of $1d_3$ CP (blue) and $0d_4$ CP (orange). Each ensemble consists of 12 molecules (7).

ratios of the two ensembles result upon simply shifting the double bond from the 3 to 4 position. Whether similar conformational changes of molecular ensembles can be achieved by variations of other functional groups remains to be seen.

LCD PROJECTION WITH CHOLESTERIC OPTICAL ELEMENTS

Because of the yet unresolved technical problems with large area direct view flat screens, high resolution and compact video LCD projectors are interesting alternatives to display large images. For a review of conventional LCD projection optics see Reference 77.

Crucial for the performance of a projector are the means by which the three basic colors—red, green, and blue—are generated. The most straightforward and compact approach used in all laptops is the splitting of each pixel into three subpixels in series with the respective absorptive color filter. Because each filter absorbs at least two thirds of the incident white light, the spectral fill factor is at best 33%, which strongly reduces the brightness of the projector. Moreover, for a given picture resolution N , the split pixel approach requires displays with a total of $3N$ pixels. Apart from unsatisfactory spectral characteristics and high costs, dye filters tend to degrade under strong light intensities.

Spectral losses are avoided by splitting the incident white light beam into three separate beams, one for each color. Ideally, a fill factor of 1 results for a split beam configuration. To modulate the three colors, three displays with N pixels each are required; i.e. the projector resolution increases by a factor of three. The drawbacks of beam splitting are bulky, expensive, and rather heavy optical configurations.

LCD Projection with Cholesteric Color Filters and Polarizers as Optical Elements

We have shown that unpolarized light can be efficiently converted into circularly or linearly polarized light via selective reflection at cholesteric liquid crystal layers (65). Moreover, we have presented liquid crystal polarized color projection concepts whose functional parts consist not only of liquid crystal display modulators but also of cholesteric liquid crystal color filters and liquid crystal polarizers (64–66). A number of different field-effects were used as modulators (51).

Cholesteric liquid crystal color projectors convert incoherent, unpolarized white input light into the three circularly polarized basic colors, red, green, and blue. Figure 26 shows a reflective example of one stage of a projector with a twisted nematic liquid crystal display as a modulator (64). The left-handed cholesteric entrance filter CF_L in Figure 26 selectively reflects the left-handed circularly polarized (50%) portion of the unpolarized input light I_0 from

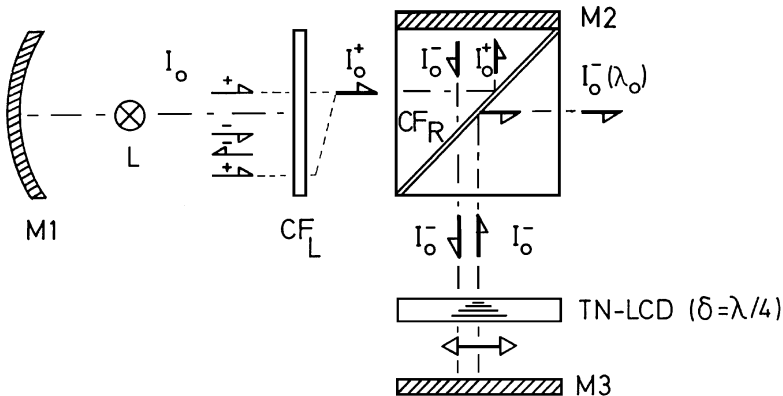
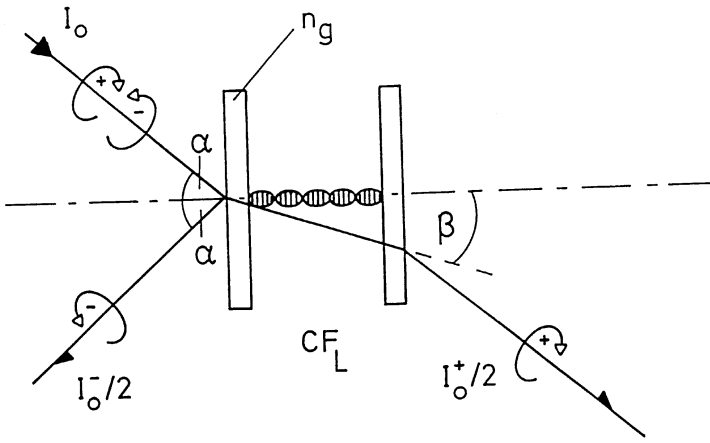


Figure 26 Principle of one stage of a liquid crystal polarized color projector operated in reflection. The optical retardation of the TN-LCD in the off-state is $\delta(V=0) = \lambda/4(2n + 1)$. The left-handed circularly polarized output intensity I_0^+ at wavelength λ_0 is selectively deflected at the right-handed cholesteric filter CF_R . M1, M2, M3 = metallic reflectors; CF_L = left-handed cholesteric filter whose wavelength of selective reflection λ_0 is tuned to that of CF_R taking the angle of light incidence on CF_R into account (64).



$$\lambda_0 = \frac{n_o + n_e}{2} p = \bar{n}p$$

$$\lambda(\alpha) = \lambda_0 \cos \left[\sin^{-1} \left(\frac{2 \sin \alpha}{n_o + n_e} \right) \right]$$

$$\Delta\lambda = \lambda_0 \Delta n / \bar{n}$$

$$\sin \alpha / \sin \beta = n_g$$

$$Y \propto \int_{vis} P_\lambda V_\lambda T_\lambda d\lambda$$

Figure 27 Optical properties of planar cholesteric filters. λ_0 = wavelength of selective reflection, p = cholesteric pitch; $\Delta\lambda$ = bandwidth of selective reflection/transmission. I_0^- and I_0^+ are the left- and right-handed circularly polarized light intensities. I_0 = unpolarized input light.

lamp L back to the metallic reflector M1. Upon reflection, the handedness changes from left to right and, as a consequence, the reflected, right-handed circularly polarized light passes CF_L . Ideally, this simple polarization converter fully converts unpolarized light I_0 into circularly polarized light I_0^+ within the selective reflection band of CF_L (Figure 26) (65).

Figure 27 shows the basic optical properties of planar cholesteric liquid crystal layers (78, 79). Within the wavelength range $\Delta\lambda$ where Bragg reflection

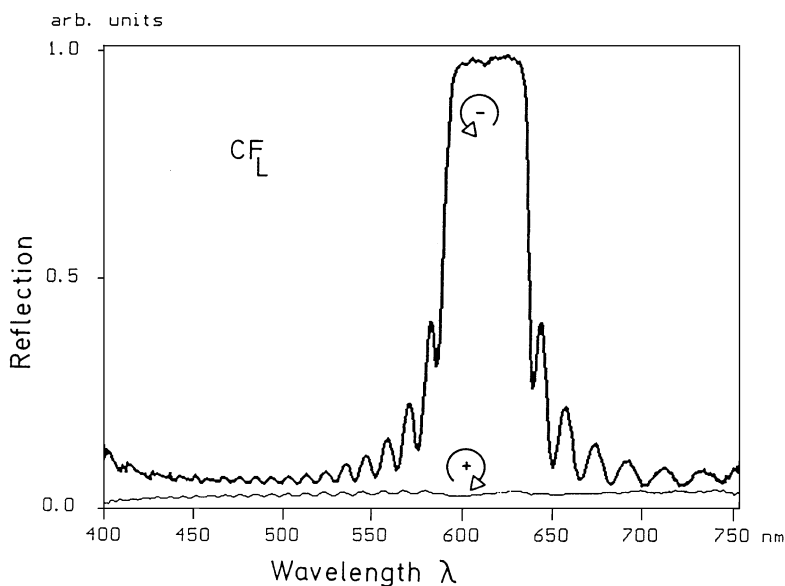


Figure 28 Wavelength dependence of selective reflection of unpolarized light at vertical incidence on a left-handed, planar cholesteric layer. The short pitch cholesteric liquid crystals are from ROLIC Ltd. (64).

occurs, incident, incoherent, and unpolarized light of intensity $I_0 = (I_0^-/2 + I_0^+/2)$ is partly reflected and partly transmitted by the left-handed cholesteric filter CF_L .

Figure 28 shows the wavelength dependence of the selective reflection of vertically incident unpolarized light of a left-handed cholesteric filter CF_L . The pitch of the filter is adjusted so that maximum selective reflection for left-handed light occurs at $\lambda_0 = 600$ nm. The right-handed polarization passes the filter unaffected over the entire visible wavelength range. The filter bandwidth is determined by the optical anisotropy Δn of the liquid crystal (Figure 27). To suppress the pronounced temperature dependence of the pitch and of the optical anisotropy of cholesteric liquid crystals (80), which both determine the filter properties (Figure 27), we have developed pairs of short-pitch cholesteric molecules with opposite temperature coefficients. By properly adjusting their composition in complex cholesteric mixtures, temperature-independent cholesteric filter mixtures were achieved whose selective reflection in the visible wavelength range changes less than 2 nm over 80°C (11, 64).

Different authors have shown that the temperature-dependent increase of the pitch of chiral nematic mixtures can be reduced by doping them with left- and

right-handed chiral additives (80, 81). We have shown that a similar approach can be used to compensate the temperature dependence of the center wavelength $\lambda_0(T)$ of short-pitch cholesteric mixtures (64). However, to maintain the short pitch, the chiral dopants required for our purpose must be designed such that at least two of the dopants exhibit opposite linear temperature coefficients of their helical twisting power $1/p$ in a nematic mixture doped with n chiral additives of concentration c_i (64).

$$1/p(T) = \sum_{i=1}^n c_i [A_i + B_i(T - 22^\circ\text{C}) + C_i(T - 22^\circ\text{C})^2 + \dots]. \quad 35.$$

The linear coefficients B_i in the expansion of Equation 35 essentially determine the temperature dependence of the helical twisting power of the mixture. From Equation 35 and from the central wavelength λ_0 of selective reflection of a planar-aligned cholesteric layer at vertical light incidence (Figure 27),

$$\lambda_0 = \frac{n_o + n_e}{2} = \bar{n}p, \quad 36.$$

the temperature dependence $\lambda_0(T)$ of the layer becomes (64)

$$1/\lambda_0(T) = \sum_{i=1}^n c_i [A_i + B_i(T - 22^\circ\text{C}) + C_i(T - 22^\circ\text{C})^2] [a + b(T - 22^\circ\text{C})], \quad 37.$$

where c_1 – c_n are the concentrations of the chiral dopants, and A_i , B_i , and C_i are chiral expansion coefficients. The expansion coefficients a and b in Equation 37 follow from the expansion of the average refractive index n of the cholesteric mixture (Figure 27):

$$\frac{1}{\bar{n}} = a + b(T - 22^\circ\text{C}). \quad 38.$$

In the case of two chiral dopants (Equation 37), temperature-independent selective reflection results if the chiral dopants meet the following condition (64):

$$a(c_1B_1 + c_2B_2) = -b(c_1A_1 + c_2A_2). \quad 39.$$

Equation 39 shows that temperature-independent selective reflection can be achieved with at least two chiral dopants with additive short pitches (required for selective reflection in the visible) and opposite temperature coefficients (64).

Figure 29 shows three temperature-independent right-handed cholesteric filter mixtures whose center wavelengths are tuned to red, green and blue. Over their entire operating temperature range from 0 to 80°C, a small temperature dependence $d\lambda_0/dT < 0.1 \text{ nm}/^\circ\text{C}$ results. Virtually temperature-independent,

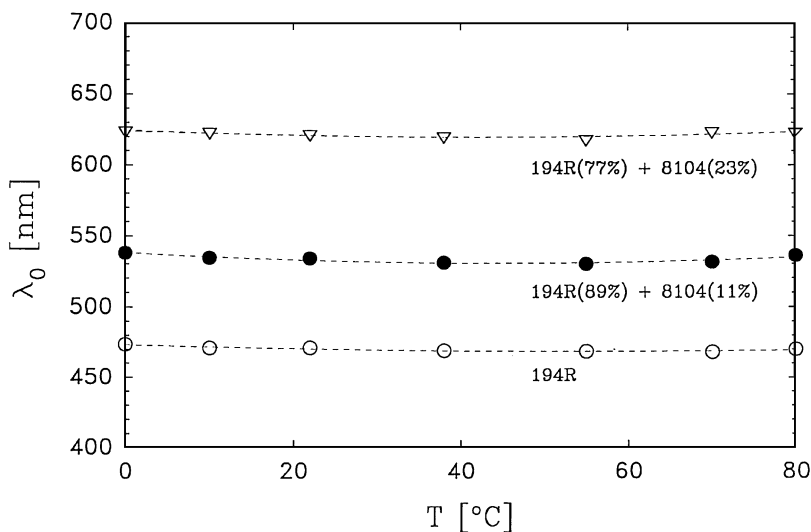


Figure 29 Temperature-independent selective reflection λ_0 of three right-handed cholesteric mixtures of ROLIC Ltd which are tuned to the basic colors red, green, and blue.

left- and right-handed monomeric cholesteric mixtures can be achieved according to the above design rules. Applications for such mixtures are not only cholesteric optical filters (64) but also cholesteric phase-change displays (83, 84) and displays making use of the strong flexo-electricity of short-pitch chiral nematics (85, 86). Still broader operating temperature ranges were shown to result from cross-linking cholesteric liquid crystal side chain polymers (82). For examples of short-pitch chiral nematic molecules that satisfy Equation 39, see Reference 87.

Subtractive Video Color Projection with Cholesteric Band Modulation Filters

Recent progress made in monomeric and polymeric cholesteric materials and in cholesteric optical configurations has spurred interest in cholesteric LCDs and LCD projection optics (11, 64–66, 82, 84, 86). By making use of the unique wavelength selective transmission and polarization properties of stacked cholesteric layers, optical retarders, and LCD-modulators, Fünfschilling & Schadt have recently presented an unusually compact LCD projection concept that renders pixel-by-pixel subtractive color modulation feasible (11). This is reviewed in the following.

Figure 30 shows the geometry and the state of polarization of a single cholesteric band modulation filter (BMF) tuned to one of the three basic colors

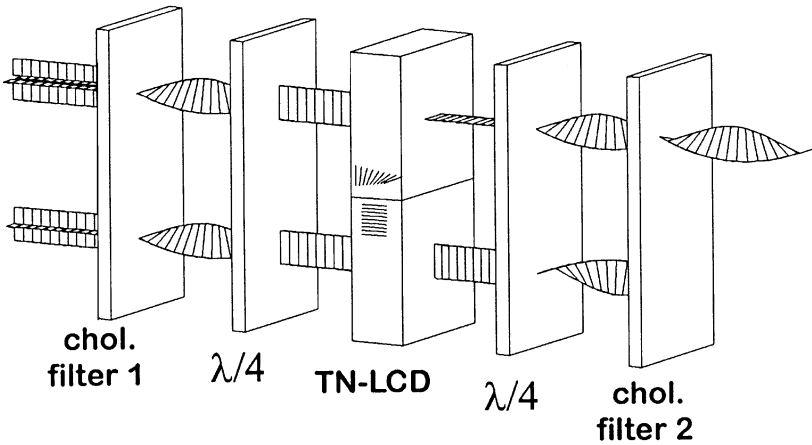


Figure 30 Band modulation filter (BMF) consisting of two identical cholesteric filters, two quarter-wave plates and a TN-LCD modulator; on-state (*top*) and homeotropic off-state (*bottom*). Shown are the polarization states of unpolarized incident light with wavelength within the selective-reflection band of the cholesteric filters. The illustration of the different polarization states is self-explanatory. When much faster switching speeds than those of TFT-TN-LCDs are required, TN displays can be replaced by DHF-LCDs, which also continuously rotate the polarization by 90° (11).

to be projected by the BMF-LCD projector (11). The BMF in Figure 30 consists of two identical cholesteric filters, two lambda quarter waveplates, and a liquid crystal display with N pixels. The schematic shows a TN display with two pixels, the upper pixel in its off-state and the lower pixel turned-on. The TN display acts as a phase modulator; it can be replaced by another type of LCD, for instance by a much faster responding DHF-LCD (10). Within the selective reflection band of the two cholesteric filters the transmission of the BMF is controlled by the optical retardation of the TN display (Figure 30). For wavelengths outside the selective reflection band, the BMF is fully transmissive and virtually does not affect the state of polarization of the transmitted light (11, 64); i.e. unpolarized input light leaves the BMF unattenuated and unpolarized. Figure 30 shows the two extreme transmission states of a BMF, namely maximum transmission (*top*) and no transmission (*bottom*). Intermediate driving voltages, which are applied to the TN display, lead to intermediate transmission levels (gray scale or color hue). Because BMFs electrically control the transmission within a selective wavelength band, band modulation filters are ideally suited for generating subtractive colors. We achieved this by stacking three BMFs of the type shown in Figure 30 in series; each filter was tuned to one of the three basic colors (11). This allows for modulation of the intensity and the color of

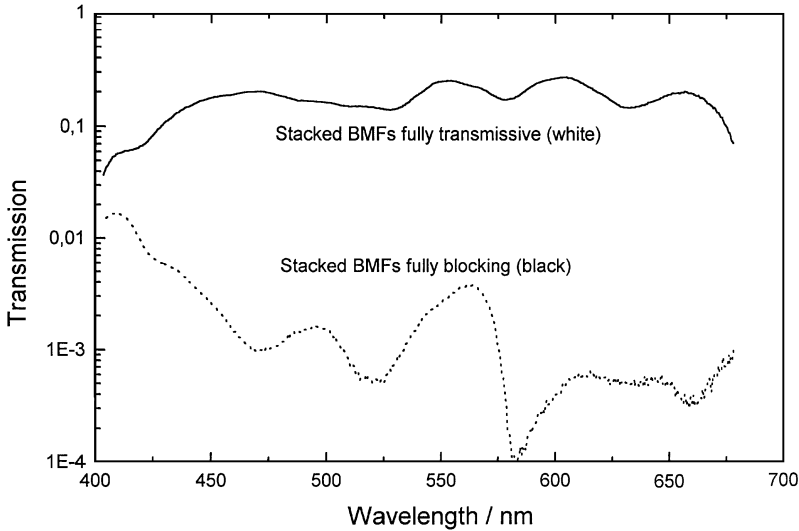


Figure 31 Measured transmission for unpolarized, white incident light of a BMF stack consisting of three BMFs in series according to Figure 30. Upper graph: BMF stack fully transmissive; lower graph: fully blocking. Note the logarithmic transmission scale (11).

the transmitted light over a large dynamic range and with a high degree of color purity (11).

Figure 31 shows the spectral response of the transmission of three band modulation filters in series in their respective fully transmissive and fully blocking states (11). There is a contrast $>100:1$ over the entire visible range. The brightness of the video-compatible BMF projector considerably exceeds the brightness of split-pixel projectors, and it combines high contrast and excellent color saturation with extremely flat design (<4 mm when using solid-state cholesteric filters and integrated LPP/LCP retarders) and low weight (11).

OPTICAL ALIGNMENT OF LIQUID CRYSTALS

The successful operation of twisted nematic or any other field-effect display requires control of molecular alignment, which is currently achieved by confining the liquid crystal layer between two mechanically rubbed surfaces (88). Alternatively, to uniaxially buffing polyimide-coated substrates, angular evaporation of S_iO_x was shown by Janning to lead to a grooved surface topology, which uniformly aligns the nematic director over the entire display area (89). Alignment between microscopically grooved surfaces was shown by Berreman to occur via minimizing the splay and bend elastic deformation energy of the liquid

crystal layer (90). Possible competing anchoring forces from intermolecular interactions were neglected (90).

Virtually all liquid crystal molecules designed for field-effect LCDs comprise permanent dipole moments, such as lateral or longitudinal cyano groups (Figure 3). Therefore, their alignment may be affected by dipolar interactions with the substrate. However, since little is known about electric fields on free surfaces, the dipolar contribution to the surface energy, which aligns the effective dipoles along the field, is difficult to estimate. For methoxy benzyldiene-butyl aniline (MBBA), Prost & Ter-Minassian-Saraga have experimentally determined the dipolar part of the surface energy of a surfactant-coated surface (91). They attribute 25% of the total surface energy to dipolar interactions, whereas 75% is attributed to dispersive forces. The substrate coatings consist of monomolecular layers of a polar surfactant with a (nonpolar) hydrocarbon side chain. Surfactant layers of different density were administered by Langmuir Blodgett techniques. In their evaluation the authors (91) did not consider possible steric contributions to the alignment via the hydrocarbon side chains of the surfactant. Possible chain reorientation and increasing chain rigidity with increasing surfactant density and/or the induction of flow alignment in the side chains during film preparation were also neglected.

Because of the simplicity in manufacturing buffed polyimide aligning layers, virtually all of today's LCDs are aligned by this process. However, in contrast to the simplicity of the process, the microscopic mechanisms responsible for the alignment of liquid crystals on buffed substrates are complex and have scarcely been investigated. This partly explains the often ambiguous interpretation of experimental results on buffed polymer layers. While some authors propose that the buffing process stretches the polymer chains, thus aligning the liquid crystal director parallel to the direction of buffing (92) others—such as Ishihara et al (93)—have shown that the director orientation need not be parallel to the buffing direction. However, by scanning electron microscopy, the same authors (93) showed that buffing creates microgrooves on polymer films that do not topologically dominate the alignment.

In addition to the drawbacks associated with rubbing, such as the generation of dust and electrostatic charges that are detrimental, especially for manufacturing TFT displays, the result of mechanical alignment is primarily macroscopic. Therefore, mechanical processes are suitable for aligning displays uniaxially over entire display areas; however, they are inadequate for generating high-resolution azimuthal aligning patterns. An exception is the recently described mechanical alignment of liquid crystals on substrates that were grooved by the stylus of an atomic force microscope (94). Because of the uniaxial nature of conventional mechanical aligning processes, TN displays suffer significantly from restricted viewing angles (8, 95, 96). This problem can be circumvented if

molecular alignment is varied, in a controlled manner, within individual pixels (97–102). Schadt et al have recently shown that this can be achieved effectively by photo-alignment of liquid crystals (8). In the following, their linear photopolymerization (LPP) technology is reviewed.

Optical Patterning of Multidomain LCDs with Wide Viewing Angles

Exposure of functional substrates to polarized light offers a means of achieving high-resolution patterns in the plane of the display (9, 103, 104). But to ensure that the alignment pattern imposed on the liquid crystal layer sandwiched between the two display substrates is free of orientational defects, the tilt angle between the long molecular axes and the substrates must be precisely controlled (105). Recently, we have shown that our earlier linear photo-alignment strategy (9, 103) can be extended to obtain such control and thereby fabricate stable, multidomain pixel displays with markedly improved fields of view (8).

Underlying the electro-optical properties of all liquid crystal displays is the requirement that, in their off state (no applied electric field), the directors of the liquid crystal layer are aligned uniaxially at the two display boundaries. Moreover, to achieve stable electro-optical characteristics, the non-zero bias tilt angle θ between \hat{n} and the display substrate(s) must be well defined. We have shown that anisotropic van der Waals forces are primarily responsible for the alignment of liquid crystals on substrates treated with our linear photopolymerization (LPP) technology (9, 103). In the case of poly(vinyl 4-methoxy-cinnamate) photopolymers, these forces were shown to align \hat{n} perpendicular to the electric field vector \hat{E} of the incident linearly polarized ultraviolet radiation, which leads to anisotropic depletion of LPP prepolymer molecules and simultaneously generates uniaxially aligned photo products via anisotropic cross-linking (9, 103). Because of the cylinder symmetry with respect to \hat{E} of this LPP process, the probabilities are equal for photo-generating the mirror symmetrical bias tilt angles $\theta(x) = -\theta(-x)$ on a microscopic scale, where x, y are the substrate coordinates. Macroscopically, this leads to zero bias tilt (103). Although attempts were made to break the symmetry of our LPP process by exposing LPP substrates sequentially under different directions of light incidence, the resulting angles $\theta < 0.3^\circ$ were very small (101) and not stable for practical purposes (9). From these considerations it follows that the photo cross-linking and aligning symmetries of the LPP process had to be changed. We achieved this with a modified LPP process schematically depicted in Figure 32 such that liquid crystal alignment occurs not perpendicular to \hat{E} as before (9, 103), but within the plane defined by \hat{E} and \hat{k} of the incident cross-linking ultraviolet radiation. As a consequence of the new symmetry and by changing the angle of incidence of \hat{k} , stable, photo-induced bias tilt angles θ , which can be adjusted over the

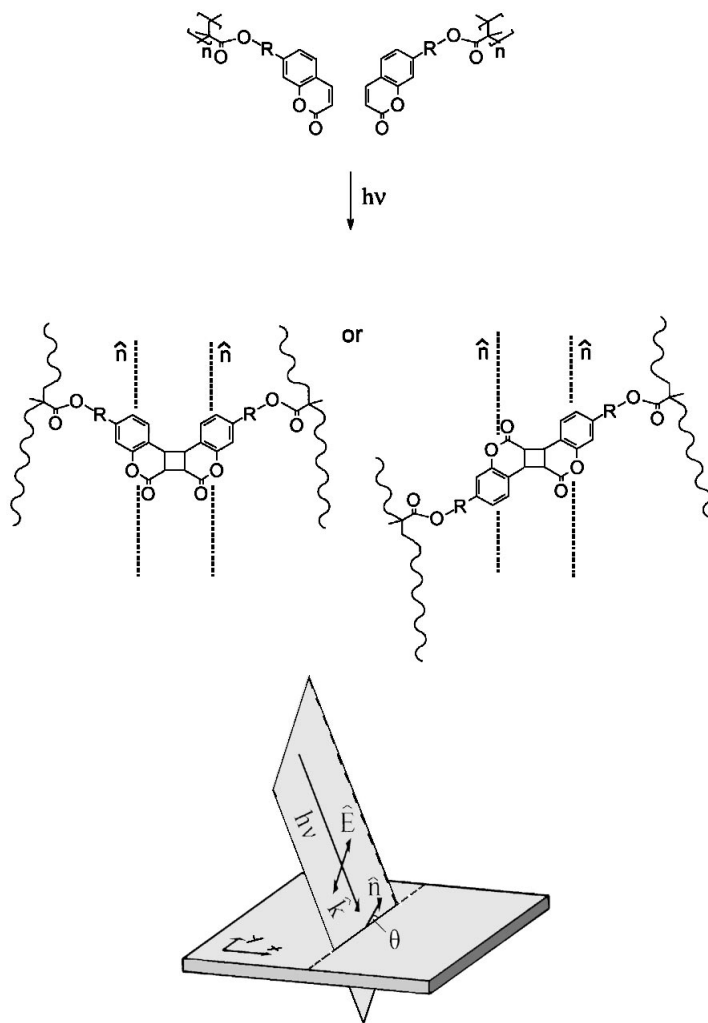


Figure 32 A pair of isotropically distributed prepolymer coumarin side chain molecules for use in the LPP process. The directional LPP photoreaction is parallel to the direction of the electric field vector \hat{E} of the incident linearly polarized UV radiation; R_1 = side-chain spacer. The photoinduced bias tilt angles $\hat{n}(\theta)$ are adjustable from $\theta = 0-90^\circ$. The photo alignment is optically and thermally stable up to temperatures $>200^\circ\text{C}$. The diagram at the bottom of the figure schematically depicts the photo-generation and the symmetry of the LPP process (8).

entire range $\theta = 0 \cdots 90^\circ$, have become possible (8). As an example, Figure 32 (*top*) schematically depicts two coumarin photo-prepolymer molecules that we designed to exhibit the desired LPP symmetry. Also shown in Figure 32 (*center*) are two of the four possible in-plane configurations of the anisotropically aligned coumarin photo products generated by the $(2 + 2)$ -cyclo addition of the LPP process. Analogous to our earlier LPP model (9, 103), we assume that liquid crystal alignment \hat{n} in the y -direction occurs (*a*) via anisotropic van der Waals interactions of the rigid cores of the anisotropically cross-linked photo products, (*b*) via anisotropic steric interactions with their partly aligned (in the y -direction) hydrocarbon polymer chains, and (*c*) via anisotropically depleted prepolymer molecules (not shown in Figure 32). The photo-aligned displays below are based on the new LPP symmetry shown in Figure 32. The LPP photo-processing steps have been described elsewhere (9, 103).

Figure 33 depicts schematically, a partially switched individual pixel of a four-domain TN display configuration (8). As in the photo-aligning patterning process described recently (106), we used a single photo mask to generate the LPP-aligning patterns of Figure 33. The different bias tilt directions θ on each substrate determine the appropriate twist sense of the four sub-TN-LCDs.

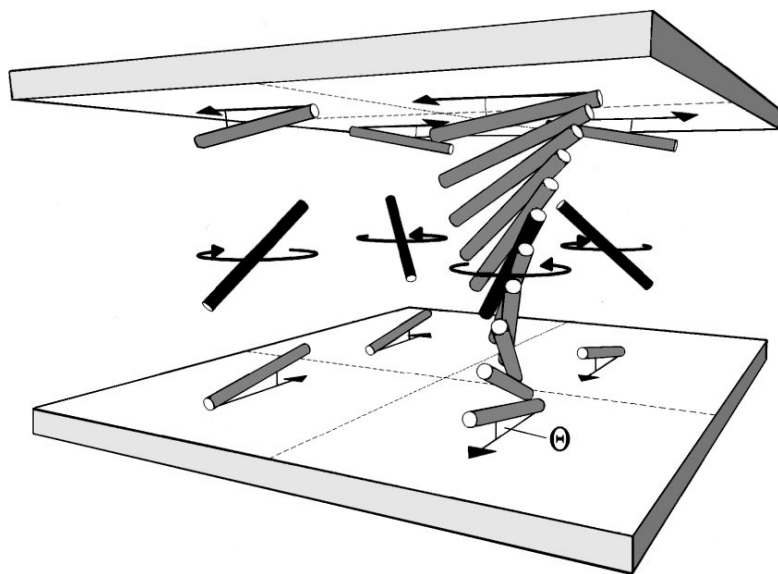


Figure 33 A single pixel of a four-domain twisted nematic TN-LCD configuration in its partly switched-on state (80% transmission between crossed polarizers). Three of the four (differently twisted) subtisted nematic helices are indicated by their respective boundary and central directors (8).

Different bias tilt angles were achieved by changing the angle of incidence of the wavevector \hat{k} (Figure 32). On a macroscopic scale, the optical anisotropies of the differently aligned central directors \hat{n} of the four sub-helices in Figure 33 compensate each other. Therefore, the angular dependence of four-domain displays is strongly reduced compared with the single-domain display in Figure 13. In Figure 33 this is indicated by the emphasized central directors of the four differently aligned, single-domain subhelices.

Figure 34 demonstrates the remarkably improved field of view of a photo-aligned four-domain TN display with crossed polarizers (*top*) compared with the strongly angle-dependent brightness of a conventionally brushed, single-domain display (*bottom*) (8). The angular dependence of the brightness of the two partially switched-on displays in Figure 34 was measured in all four quadrants between vertical light incidence and 60° off-axis. The gray levels at vertical light incidence are identical for both displays and correspond to 50% transmission at vertical light incidence. Figure 34 shows that, instead of remaining constant, the brightness of the conventional display changes by nine gray levels (out of ten) within its first and third quadrant, whereas the brightness of the photo-aligned four-domain display changes by only three gray levels within any of its four quadrants.

The remarkably improved viewing performance of LPP-aligned multidomain displays is further illustrated by the photographs in Figure 35, which show the angular dependence of the gray level of a large single pixel at 70% vertical transmission of an LPP-aligned four-domain display (*top*) and of a PI-aligned single-domain display (*bottom*) (8). The large single pixel of the four-domain display is composed of one hundred $100\text{-}\mu\text{m}$ sub-TN pixels. The center pictures were taken at vertical light incidence, the others at 40° in the four quadrants. The comparison is self explanatory. Also shown in Figure 35 (*circled*) is an enlarged view of an individual four-domain display pixel viewed at 40° in the first quadrant. The magnification shows the four photo-patterned and differently aligned TN subpixels whose macroscopically averaged transmissions account for the improved angular view of the photo-aligned four-domain display. The maximum contrast of the two displays in Figure 34 is identical at vertical light incidence. It is interesting to note the black border lines between the subpixels in the higher-magnification picture (*circled*) of Figure 34. Because of the black appearance of the dislocations between crossed polarizers, there is no need to disguise the borders by a black matrix, nor does subpixelation reduce the maximum display contrast.

Recently, Kim et al have demonstrated the first 10-inch color TFT-TN-LCD made up of one LPP-aligned four-domain TFT substrate and one conventionally brushed polyimide countersubstrate (107). Because their LPP process exhibits the same cylinder symmetry as used in our original work (103), zero bias tilt would have resulted (103). To break the cylinder symmetry and to obtain a

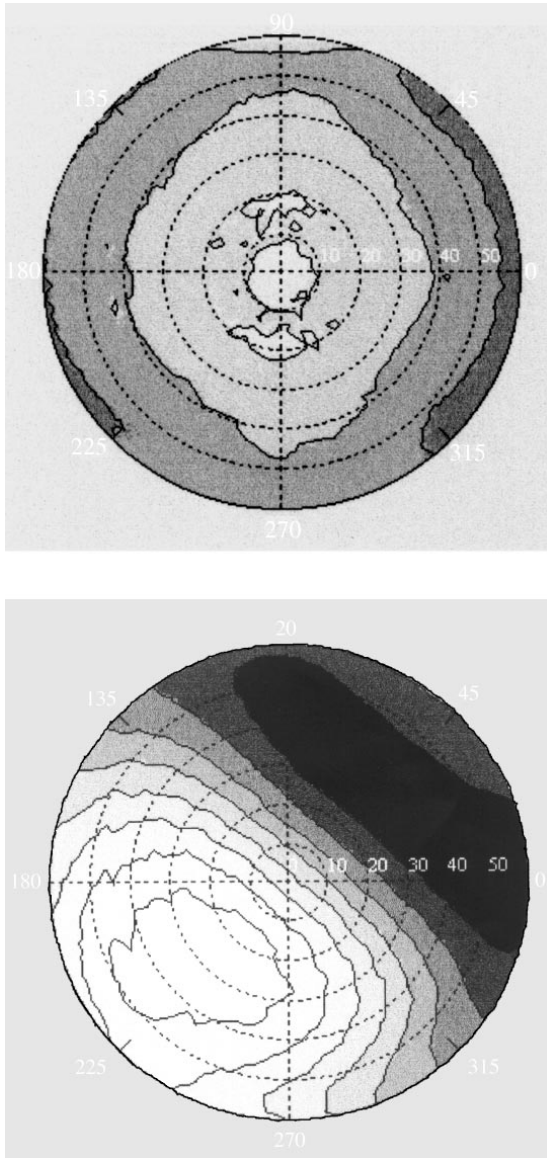


Figure 34 Viewing-angle dependence of the brightness at 50% vertical transmission of LPP-aligned four-domain TN-LCD (*top*) and brushed PI single-domain TN-LCD (*bottom*). The intensity of shadings, which are separated by azimuthal angular contours, correspond to the (ten) levels of intensity transmitted by the displays at different angles of light incidence in the four quadrants. The maximum display transmission range is divided into ten intensity levels; black corresponds to minimum display transmission (8).

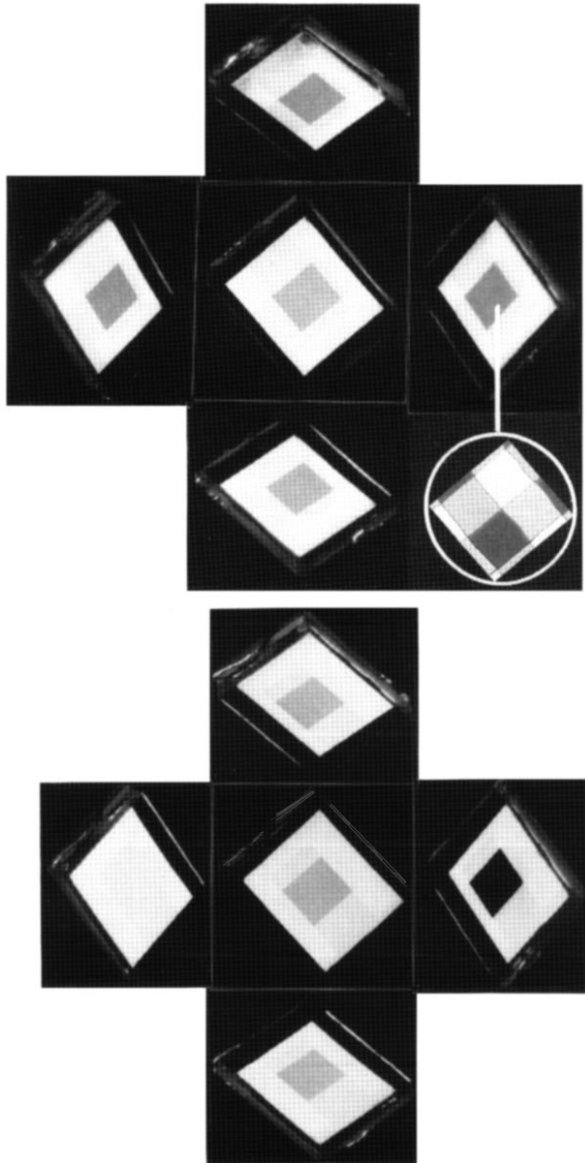


Figure 35 Viewing-angle dependence of an LPP-aligned four-domain TN display (*top*) and of a PI-aligned single-domain display (*bottom*). The pixel area of both displays is 1 cm^2 . The subpixel size of the four-domain display is $100 \mu\text{m}$. At vertical incidence (middle) both displays exhibit identical gray levels corresponding to 70% transmission. (See text for discussion of circled, higher-magnification picture). The four pictures around each central picture show the displays when viewed at 40° (with respect to the vertical) in each of the four quadrants (8).

defined bias tilt angle, Kim et al sequentially, obliquely illuminated their LPP substrate (101, 107).

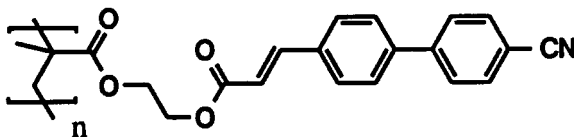
Optical Alignment and Patterning of Liquid Crystal Polymers on Single LPP Substrates

Apart from liquid crystal alignment, we have shown that linear photopolymerization also induces optical anisotropy in LPP films (103). However, because of their thus far weak optical anisotropy $\Delta n = (n_e - n_o)$, unduly thick LPP films would be required to generate significant optical retardations ($\delta = \Delta n \cdot d$) such as those required for optical retarders. Moreover, because the slow optical axis n_e of the refractive index ellipsoids of a LPP film is parallel to its LC-aligning direction \hat{n} (103, Figure 32), the azimuthal angle between n_e and \hat{n} cannot be varied. Thus it is not possible to independently adjust optical retarder properties and LC-aligning direction.

Recently, we found that the LPP process not only induces alignment in adjacent monomeric liquid crystal layers but also in liquid crystal polymer (LCP) layers deposited on single LPP substrates (9, 106). This made it possible to separate aligning and optical functions in photo-patterned multilayer LPP films. Our high-resolution hybrid LPP configurations exhibit excellent optical and thermal stability as well as tunable optical retardations with index ellipsoids whose axes are pixel-by-pixel independently adjustable (9, 106). The underlying molecular mechanisms and the operating principles of some new optical devices, such as photo-patternable optical retarders, polarization interference filters, or copy-proof phase retarder images, which are visible only in polarized light, are reviewed in the following.

For cinnamic acid PVMA LPP materials we have shown that dispersive anisotropies result from anisotropically cross-linking and aligning LPP photopolymers with linearly polarized UV light. This induces uniaxial alignment in adjacent liquid crystals and optical anisotropy in the LPP film (9, 103). Because the anisotropic photo reactions induced by the LPP process strongly affect the spectra of LPP films, UV spectroscopy and UV dichroism were shown to be efficient tools for elucidating surface-aligning processes (9, 103).

Figure 36 shows the isotropic UV absorption spectra of a 120 nm thin, spin-coated cyano biphenyl LPP film on a quartz substrate recorded at different times of film exposure to linearly polarized UV light of $\lambda \approx 310$ nm (9). The structure of the LPP prepolymer has a cinnamic acid photoreactive group in its cyano biphenyl side chain (9):



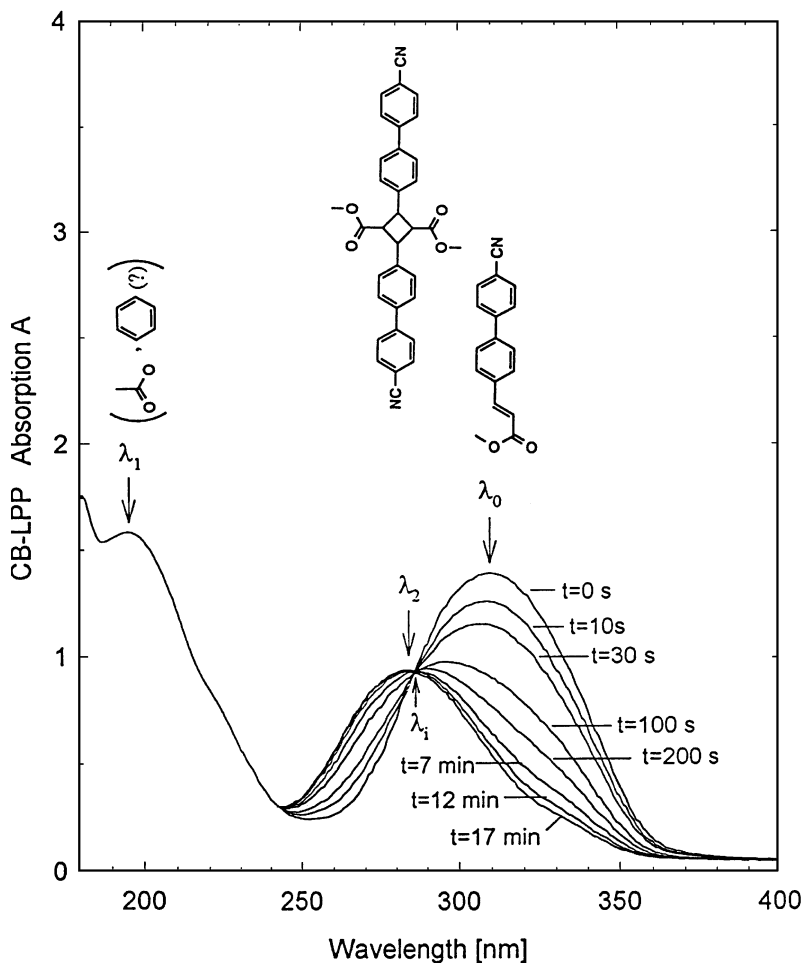


Figure 36 Isotropic absorption spectra and corresponding molecular moieties of 120 nm thin CB-LPP film recorded at different times of LPP film exposure to linearly polarized UV light of $\lambda = 310$ nm (9).

Before starting exposure at the time $t = 0$, two peaks occur at $\lambda_0 = 310$ nm and $\lambda_1 = 195$ nm (Figure 36). With progressing linear photo cross-linking, the peak at λ_0 decreases, a new peak develops at $\lambda_2 = 280$ nm, while the short-wavelength peak at λ_1 remains essentially unchanged. Figure 36 also shows an isosbestic intercept point occurring at λ_i indicating that a single photo process dominates the generation of the absorption peak at λ_2 . In analogy to our earlier proposed LPP model (103), it follows from Figure 36 that the cinnamoyl groups

of adjacent cyano-biphenyl (CB) LPP precursor polymer molecules undergo unidirectional (2 + 2) cyclo addition and alignment upon cross-linking with linearly polarized UV light (9). Figure 36 depicts the molecular structural moieties we found to correlate with the respective absorption peaks of the CB-LPP film. The peak at λ_1 seems to be caused by π - π^* and/or n - π^* transitions of molecular submoieties, such as individual benzene rings of keto groups that we could not unambiguously identify.

To detect the dispersion anisotropies generated by the LPP process and to correlate them with the orientational anisotropies of the molecular moieties of Figure 36 and the induction of uniaxial LC alignment by these moieties, we determined the dichroism of the CB-LPP film after different LPP-exposure times (9). The LPP film dichroism $\Delta A = (A_{\parallel} - A_{\perp})$ versus wavelength is depicted in Figure 37a (9), where A_{\parallel} is the absorption parallel to the direction of linearly polarized UV cross-linking light P_{UV} (Figure 36). As expected, the film is optically isotropic before starting the LPP process ($t = 0$ in Figure 37a). With increasing length of polarized UV exposure, symmetrical negative dichroic peaks occur at 200 nm, whereas asymmetrical, negative dichroic peaks occur between 250 and 360 nm (Figure 37a). From the negative sign of the peaks in Figure 37a, it follows that the long molecular axes of the dichroic molecules align perpendicular to P_{UV} . Moreover, the asymmetry of the graphs $\Delta A(\lambda)$ in Figure 37a becomes more pronounced with increasing exposure time, while the amplitude of the peak at 310 nm reaches a maximum after about 3 min of UV exposure followed by a decrease. We assume this asymmetry to be the overlap of two symmetrical dichroic peaks. To resolve the spectrum between 250 and 360 nm, we fitted graph c in Figure 37a with the two symmetrical graphs (Fit 1 and Fit 2, Figure 37b). Comparison of the peak wavelengths λ_0 and λ_2 of Fit 1 and Fit 2 with the peaks of the absorption spectra of Figure 36 shows that the same molecular moieties causing the absorption spectra of Figure 36 undergo anisotropic orientation during the LPP photo process. From their negative dichroism, the conjugated long axes of these moieties align perpendicular to P_{UV} .

Figure 38 summarizes our model of the anisotropic photoreactions and azimuthal molecular orientation induced by the linear photopolymerization process in CB-LPP (see Figures 36, 37) (9, 103): (a) The cyano-biphenyl cinnamoyl side chains of the precursor photopolymers are depleted by the LPP process parallel to P_{UV} . (b) With increasing P_{UV} exposure, the depletion first leads to negative dichroism, then the dichroic peak amplitude at λ_0 decreases. (c) The decrease of the peak amplitude at λ_0 with increasing exposure time is due to the increasing probability that pairs of adjacent cinnamoyl double bonds with off-axis orientations with respect to P_{UV} undergo cross-linking. (d) The dichroic peaks developing at λ_2 are due to the (2 + 2)-cyclo-added cyano-biphenyls aligning essentially perpendicular to P_{UV} . The weak positive

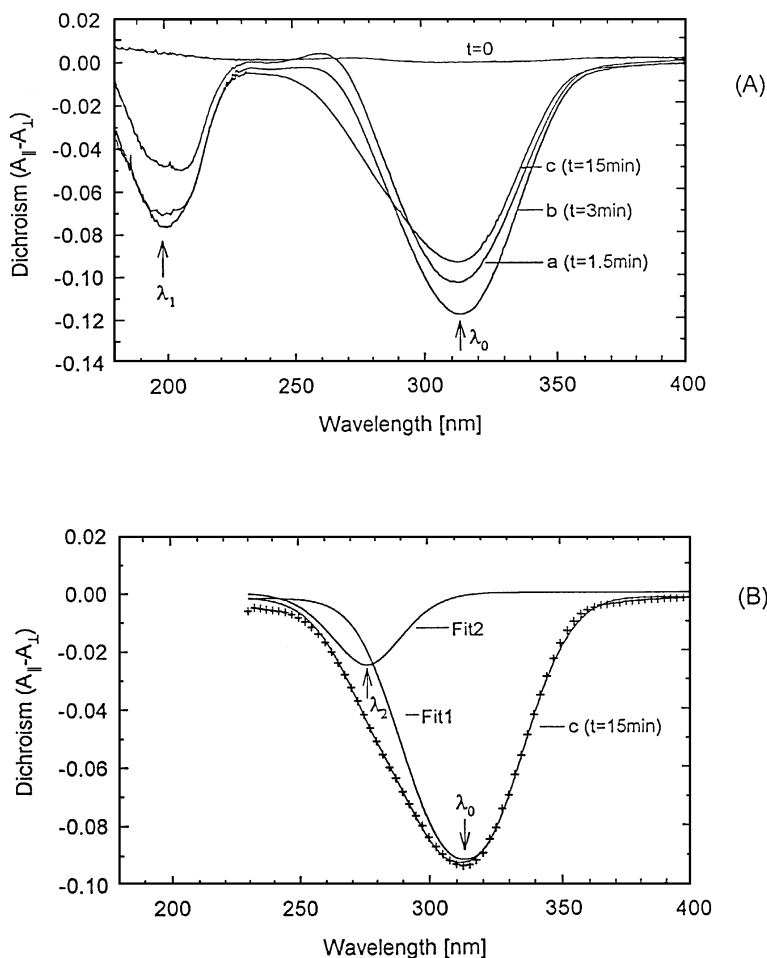


Figure 37 (a) CB-LPP dichroism $\Delta A = (A_{||} - A_{\perp})$ versus wavelength at different times t of LPP film exposure to linearly polarized UV curing light. (b) Superposition of Fit 1 and Fit 2 fitting the experimentally determined graph c of Figure 37 (top). Crosses show the fitting accuracy with graph c (9).

dichroism at λ_2 at the beginning of the LPP process (graph a in Figure 37a) is indicative of an initial reorientation of the long axes of the cyclo-added cyano-biphenyls from parallel to perpendicular during the LPP process. This requires further investigation. (e) The cause for the negative dichroism at λ_1 is not yet clear. It is likely due to reorientation of molecular submoieties, such as phenyl rings or keto groups by the LPP process. Contrary to the noncylinder

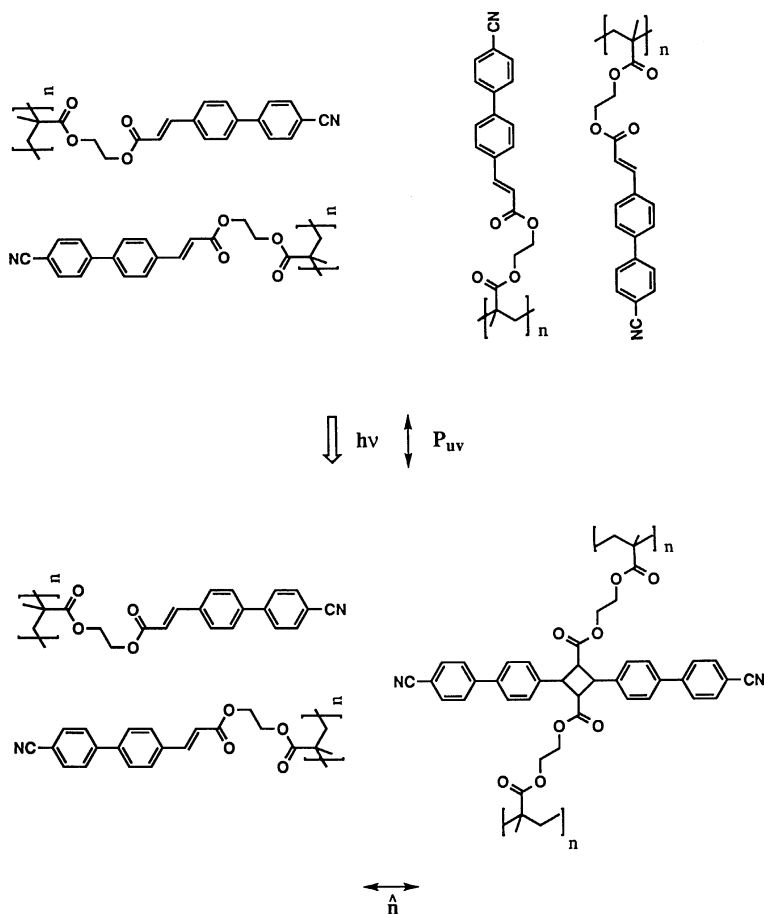
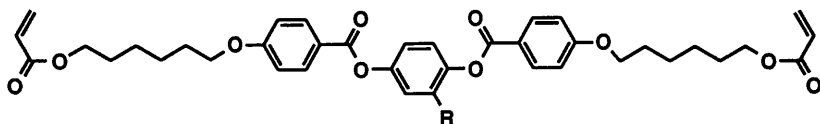


Figure 38 Model of the anisotropic molecular configuration and photoreactions caused by linear photopolymerization in CB-LPP. P_{UV} = direction of linearly polarized UV light of $\lambda = 310$ nm, \hat{n} = cylinder symmetrical preferred direction of LPP-induced LC alignment (9).

symmetrical LPP configuration of Figure 32, the photo cross-linking and the LC-aligning symmetries of the LPP configuration in Figure 38 are cylinder symmetrical and lead basically to zero bias tilt (9, 103, 107).

Prerequisites for transferring photo-generated aligning patterns from an LPP-coated substrate into the monomeric liquid crystalline phase of an adjacent liquid crystal polymer (LCP) film are LCP materials whose mesomorphic and surface wetting properties are LPP-compatible in the monomeric state. We achieved this (9) with a room-temperature nematic mixture comprising three

liquid crystalline diacrylate monomers similar to those described by Broer et al (108):



with different substituents R attached to the central phenyl ring. The LPP-LCP sample preparation, the experimental configurations for determining UV dichroism, optical anisotropy, film thickness, LC-aligning properties, and LCD performance of LPP substrates and related electro-optical devices are described elsewhere (9, 103).

Figure 39 illustrates our concept for generating hybrid stacks of photo-aligned and photo-patterned LPP/LCP films: The LPP layer transfers its aligning information a_1 into the adjacent liquid crystal polymer layer of thickness d (9, 106). The LCP layer contains the optical information, i.e. the direction n_{ei} of the i -th slow optical axes and the optical retardation $\delta_i = \Delta n_i \cdot d$ of the solid state LCP pixels, where the effective optical anisotropy is determined by the design of the LCP molecules and by the LCP bias tilt. The two pixels of the example in Figure 39 exhibit two slow optical axes n_{e1} and n_{e2} on a single glass substrate S. In Figure 39 the linear polarizers P_1, P_2 visualizing the phase retarder image are external; however, they can also be integrated by the LPP technology (9).

The optical retardation δ of the LCP film in Figure 39 was chosen $\delta = \Delta n \cdot d = 230$ nm; where $d = \text{LCP layer thickness}$ and $\Delta n = \text{LCP-birefringence}$ (9). The (adjustable) angle $\alpha = 45^\circ$ between a_1, a_2 and the nematic director orientations n_{e1}, n_{e2} was achieved by aligning and cross-linking the LPP film via a photo mask with linearly polarized UV light such that in a first step the aligning direction a_1 results, and in a second step, after rotation of the direction of linear polarization by 45° , the aligning direction a_2 follows. Because the polarization direction parallels a_2 and the extraordinary refractive index n_{e2} , the state of polarization of incident linearly polarized light transmitted by P_1 is not affected by the left segment of the LPP retarder pattern. Therefore, the left segment is nontransmissive in the crossed polarizer configuration of Figure 39, whereas due to $\alpha = 45^\circ$ and $\delta(\text{LCP}) = 230$ nm, the transmissive right segment acts essentially as a half wave-plate that rotates the incident polarization direction P_1 by 90° (negative contrast mode). Rotation of either P_1 or P_2 by 90° reverses the contrast from negative to positive.

The photo-patterned LPP/LCP-configuration with one fully transmissive and one nontransmissive pixel shown in Figure 39 represents a binary phase retarder. In analogy to Figure 39, digital LPP/LCP configurations can be used for generating more complex retarder images of pictures with not only black and white information but also gray tones. Figure 40 schematically depicts the three optical processing steps used for generating a digital LPP-LCP phase

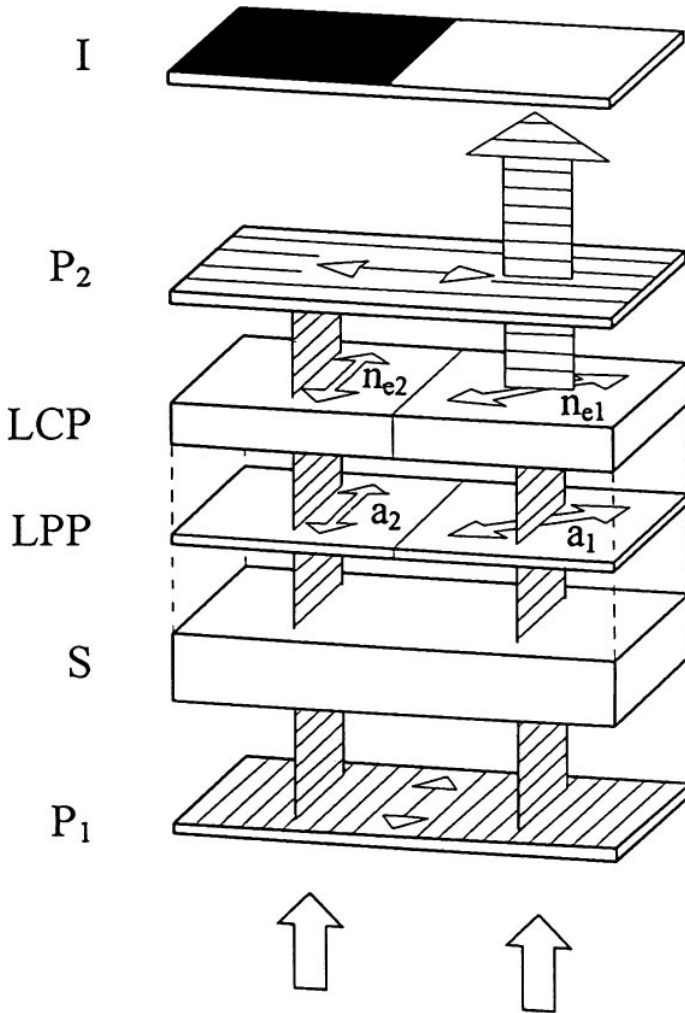


Figure 39 Optically patterned LPP/LCP retarder configuration on a single glass substrate S between external crossed polarizers P₁, P₂. The LC-aligning directions of the 120 nm thin LPP film, a₁, a₂ are parallel to the slow optical axes, n_{e1}, n_{e2}, of the 2 μm thick pixelated LCP film on top; optical retardation δ(LCP) = 230 nm (106).

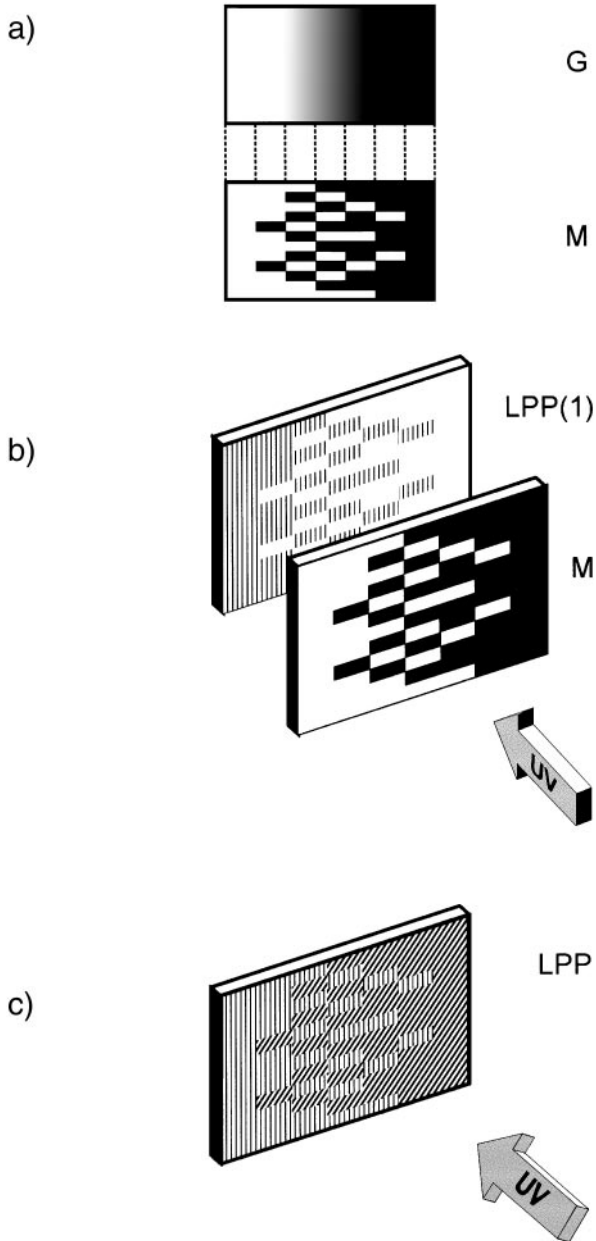


Figure 40 Illustration of the three processing steps for generating a digital LPP-aligning pattern of the gray scale G on top. M = digital photo mask (106).

retarder pattern of the gray scale G of Figure 40a (106). First, a digital photo mask is made of the gray scale that is projected onto the LPP-coated glass substrate, using vertically polarized UV light. This leads to the vertically aligned and cross-linked partially solid state substrate LPP(1) depicted in Figure 40b. Next, the photo mask is removed, and the linear UV-polarization is rotated by 45° , thus aligning and cross-linking the so far unexposed LPP sample area under 45° (Figure 40c). Finally, the completely photo-aligned and -patterned solid state LPP substrate is spin coated with a $2\ \mu\text{m}$ thin precursor LCP layer. After (instantaneous) alignment by the LPP substrate, the photo-patterned and -aligned LCP layer is conventionally photo cross-linked with unpolarized UV light, thus transferring the LCP retarder pattern into the solid state and completing the hybrid LPP/LCP process. The two sequential, anisotropic photo-patterning processing steps shown in Figure 40 make possible the generation of high information content phase retarder patterns on single substrates (106, 109).

Figure 41 shows a photograph of an LPP/LCP phase retarder image on a single glass substrate (made analogously to Figures 39, 40). To visualize the phase



Figure 41 Photograph of a complex LPP/LCP retarder image on a single glass substrate visualized in transmission in white light between crossed polarizers. Only the part of the image confined between the crossed polarizers is visible, whereas the phase information outside remains invisible (white).

information, the photograph in Figure 41 was taken with part of the substrate placed between crossed polarizers. The white area in Figure 41, where the phase image is not visible, is outside the crossed polarizers. The optical configuration of the LPP/LCP retarder in Figure 41 is identical to the configuration of Figure 39. Its black-white image is the result of the optical retardation $\delta = 230 \text{ nm} \approx \lambda/2$ (106, 109). The $6 \times 6 \text{ cm}$ digital LPP/LCP image in Figure 41 consists of 480×480 pixels. The photograph illustrates the high resolution of the LPP technology, which is better than one micrometer.

Apart from integratable and photo-patternable low-loss polarization interference filters, polarizers, and color compensators for liquid crystal displays, LPP/LCP retarders open up the possibility of generating copy-proof images visible only in polarized light (9, 106, 109). The phase information is detectable with polarization sensitive detectors in automatic safety control equipment or by visual observation through polarization filters. Aside from optically anisotropic multilayers, we have shown that additional functions such as photo-patternable LPP layers for aligning monomeric liquid crystals in LCDs, or electrode layers for addressing LCDs can be integrated into LPP/LCP configurations (9). LPP-LCP configurations operate in transmission as well as in reflection; they present a plethora of new applications.

Visit the *Annual Reviews* home page at
<http://www.annurev.org>

Literature Cited

1. Schadt M, Helfrich W. 1971. *Appl. Phys. Lett.* 18:127
2. Boller A, Scherrer H, Schadt M, Wild P. 1972. *Proc. IEEE* 60:1002
3. Schadt M. 1994. *Topics in Physical Chemistry*, ed. H Stegemeyer, 3:195. Darmstadt: Steinkopff; New York: Springer
4. Scheffer TJ, Nehring J. 1984. *Appl. Phys. Lett.* 45:1021
5. Kando YT, Nakagomi T, Hasegawa S. 1985. *Ger. Patent DE. 3503259 A1*
6. Schadt M, Leenhouts F. 1987. *Appl. Phys. Lett.* 50:236
7. Schadt M, Buchecker R, Müller K. 1989. *Liq. Cryst.* 5:293
8. Schadt M, Seiberle H, Schuster A. 1996. *Nature* 381:212
9. Schadt M, Seiberle H, Schuster A, Kelly S. 1995. *Jpn. J. Appl. Phys.* 34:3240
10. Fünfschilling J, Schadt M. 1996. *Jpn. J. Appl. Phys.* 35:84
11. Fünfschilling J, Schadt M, Seiberle H. 1996. *J. Soc. Inf. Disp. SID 4, Nr. 1:41*
12. Maier W, Saupe A. 1959. *Z. Naturforsch. Teil A* 14:882
13. Priest RG. 1973. *Phys. Rev.* 7A:720
14. Luckhurst GR. 1973. *Mol. Cryst. Liq. Cryst.* 21:125
15. de Gennes PG. 1974. *The Physics of Liquid Crystals*. ed. J Birman, SF Edwards. Oxford: Clarendon
16. Schadt M, Buchecker R, Villiger A. 1990. *Liq. Cryst.* 7:519
17. Schadt M, Petrzilka M, Gerber PR, Villiger A. 1985. *Mol. Cryst. Liq. Cryst.* 122:241
18. Moia F, Schadt M. 1991. *Proc. SID* 32:361
19. Schadt M, Helfrich W. 1972. *Mol. Cryst. Liq. Cryst.* 17:355
20. Schadt M. 1977. *J. Chem. Phys.* 67:210
21. Schadt M. 1972. *J. Chem. Phys.* 56:1494
22. Kresse H. 1982. *Fortschr. Phys.* 30:507
23. Hill NE, Vaughan WE, Price AH, Davies M. 1969. *Dielectric Properties and Molecular Behaviour*. London: Van Nostrand Reinhold

24. Maier W, Meier G. 1961. *Z. Naturforsch. Teil A* 16:262
25. Klingbiel RT, Genova DJ, Criswell TR, Van Meter JP. 1974. *J. Am. Chem. Soc.* 96:7651
26. Gray GW, Harrison KJ, Nash JA. 1974. *Electron. Lett.* 9:98
27. Eidenschink R, Erdmann D, Krause J, Pohl L. 1977. *Angew. Chem.* 89:103
28. Boller A, Cereghetti M, Schadt M, Scherrer H. 1977. *Mol. Cryst. Liq. Cryst.* 42:215
29. de Jeu WH. 1980. *Physical Properties of Liquid Crystalline Materials*. New York: Gordon & Breach
30. Gähwiler Ch. 1972. *J. Phys. Rev. Lett.* 28:1554
31. Gerber PR, Schadt M. 1982. *Z. Naturforsch. Teil A* 37:179
32. Gerber PR. 1981. *Appl. Phys.* 26A:139
33. Oseen CW. 1933. *Trans. Faraday Soc.* 29:883
34. Ericksen JL. 1960. *Arch. Ration. Mech. Anal.* 4:231
35. Leslie FM. 1966. *Q. Mech. Appl. Math.* 19:357
36. Gerber PR, Schadt M. 1980. *Z. Naturforsch. Teil A* 35:1036
37. Schadt M. 1993. *Liq. Cryst.* 14:73
38. Schadt M, Gerber PR. 1982. *Z. Naturforsch. Teil A* 37:165
39. Meier G, Saupe A. 1966. *Mol. Cryst. Liq. Cryst.* 1:515
40. Schadt M. 1977. *J. Chem. Phys.* 67:210
41. Seiberle H, Schadt M. 1994. *Mol. Cryst. Liq. Cryst.* 239:229
42. Schadt M. 1982. *Mol. Cryst. Liq. Cryst.* 89:77
43. Schadt M. 1981. *Mol. Cryst. Liq. Cryst.* 66:319
44. Buzak TS, Ilcisin K. 1992. *Dig. SID Jpn. Disp.* 92:647
45. Alt PM, Pleshko P. 1974. *IEEE Trans. Electron. Devices* ED21:146
46. Kawakami H, Yoneda Y. 1974. *Jpn. Inst. Electron. Inf. Eng.* 73:25
47. van Doorn CZ, de Klerk JJMJ. 1979. *J. Appl. Phys.* 50:1066
48. Nagata M, Nakamura H. 1986. *Mol. Cryst. Liq. Cryst.* 139:143
49. Debye P. 1929. *Polar Molecules*. Mineola, NY: Dover
50. Gruler H, Cheung L. 1975. *J. Appl. Phys.* 46:5097
51. Schadt M. 1991. *Proc. SPIE/SPSE* 1455:214
52. Katoh K, Endo Y, Akatsuka M, Ohgawara M, Sawada K. 1987. *Jpn. J. Appl. Phys.* 26:L1784
53. Okumura O, Nagata M, Wada K. 1987. *ITEJ Tech. Rep.* II:27
54. Berreman DW. 1974. *J. Opt. Soc. Am.* 63:1374
55. Gooch CH, Tarry HA. 1975. *J. Phys. D* 8:1575
56. Meyerhofer D. 1977. *J. Appl. Phys.* 48:1179
57. Pohl L, Weber G, Eidenschink R, Baur G, Fehrenbach W. 1981. *Appl. Phys. Lett.* 38:497
58. Pohl L, Eidenschink R, Krause G, Erdmann D. 1977. *Phys. Lett.* 60A:421
59. Jakeman E, Raynes EP. 1972. *Phys. Lett.* 39:69
60. Schadt M, Mueller F. 1978. *IEEE Trans. Electron Devices* ED-25:1125
61. Berreman DW. 1975. *J. Appl. Phys.* 46:3746
62. Van Doorn CZ. 1975. *J. Appl. Phys.* 46:3738
63. Schadt M, Petrzilka M. 1985. *Proc. SID Eurodisplay '84*, 26:117
64. Schadt M, Fünfschilling J. 1990. *Jpn. J. Appl. Phys.* 29:1974
65. Belayev SV, Schadt M, Barnik MI, Fünfschilling J, Malimoneko NV, Schmitt K. 1990. *Jpn. J. Appl. Phys.* 29:L634
66. Fünfschilling J, Schadt M. 1992. *Optoelectron. Devices Technol.* 7:263
67. Fredeeriks V, Zsvetkov V. 1935. *Dokl. Akad. Nauk SSSR* 2:528
68. Sugimori S. 1990. *Ger. Offenlegungsschr. DE*. 3102017C2
69. Leadbetter AJ, Richardson AJ, Colling J. 1975. *J. Phys. Colloq.* 36:37
70. Schadt M. 1993. *Ber. Bunsenges. Phys. Chem.* 97:213
71. Kawazaki K, Yamada K, Mizunoya K. 1987. *Dig. SID* 87:391
72. Okumura O, Nagata M, Wada K. 1987. *ITEJ Tech. Rep.* II:27
73. Katoh K, Endo Y, Akatsuka M, Ogawara M, Sawada K. 1987. *Jpn. J. Appl. Phys.* 26:L1784
74. Schadt M, Gerber PR. 1982. *Proc. SID* 23, 1:29
75. Buchecker R, Schadt M. 1987. *Mol. Cryst. Liq. Cryst.* 149:359
76. Schadt M. 1988. *Mol. Cryst. Liq. Cryst.* 165:405
77. Shields SE, Bleha WP. 1991. *Liquid Crystals and Applications*, ed. B Bahadur, 1:143. River Edge, NJ: World Sci.
78. de Vries H. 1951. *Acta Cryst.* 4:219
79. Blinov LM, Chigrinov VG. 1994. *Electrooptic Effects in Liquid Crystal Materials*. New York: Springer-Verlag
80. Göbl-Wunsch A, Heppke G. 1979. *Z. Naturforsch. Teil A* 34:594
81. Gerber PR. 1980. *Phys. Lett.* 78A:285
82. Häberle N, Leigerber H, Maurer R, Miller A, Stohrer J, et al. 1991. *Dig. SID* 91:57

83. Yang DK, Chien LC, Doane JW. 1991. *Proc. IRDC* 49 p. 44
84. St. John WD, Lu ZJ, Doane JW. 1995. *J. Appl. Phys.* 78:5253
85. Komitov L, Lagerwall ST, Stebler B, Strigazzi A. 1994. *J. Appl. Phys.* 76:3762
86. Patel JS, Meyer RB. 1987. *Phys. Rev. Lett.* 58:1538
87. Kelly SM, Schadt M, Seiberle H. 1992. *Liq. Cryst.* 11:761
88. Cognard J. 1982. *Mol. Cryst. Liq. Cryst. Suppl.* 1:1-74
89. Janning L. 1972. *Appl. Phys. Lett.* 21:173
90. Berremann DW. 1972. *Phys. Rev. Lett.* 28:1683
91. Prost JE, Ter-Minassian-Saraga L. 1975. *J. Phys.* 36:C1-C77
92. Geary JM, Goodby JW, Kmetz AR, Patel JS. 1987. *J. Appl. Phys.* 62:4100
93. Ishihara S, Wakemoto H, Nakazima K, Matsuo Y. 1989. *Liq. Cryst.* 4:669
94. Ruetschi M, Grütter P, Fünfschilling J. 1994. *Science* 265:512
95. Meyerhofer D. 1977. *J. Appl. Phys.* 48:1179
96. Luo FC. 1990. *Liquid Crystals*, ed. B Bahadur, Vol. 1. Singapore: World Sci.
97. Sumita T. 1977. *Jpn. Patent Appl. No.* 5269960
98. Yang KH. 1992. *Jpn. J. Appl. Phys. Lett.* 31:1603
99. Sumiyoshi K, Takatori K, Hirai Y, Kaneko S. 1994. *J. SID* 2/1:31
100. Kawata Y, Takatoh K, Hasegawa M, Sakamoto M. 1994. *Liq. Cryst.* 16:1027
101. Hashimoto T, Sugiyama T, Katoh K, Saitoh T, Suzuki H, et al. 1995. *Dig. SID* 95:877
102. Chen J, Bos PJ, Bryant DR, Johnson DL, Jamal SH, Kelly JR. 1995. *Appl. Phys. Lett.* 67:1990
103. Schadt M, Schmitt K, Kozinkov V, Chigrinov V. 1992. *Jpn. J. Appl. Phys.* 31:2155
104. Gibbons WM, Shannon PJ, Sun ST, Sweetlin BJ. 1991. *Nature* 351:49
105. Raynes EP. 1974. *Electron. Lett.* 10:141
106. Schadt M, Seiberle H, Schuster A, Kelly SM. 1995. *Jpn. J. Appl. Phys. Lett.* 34:764
107. Kim JH, Yoon KH, Wu JW, Choi YJ, Nam MS, et al. 1996. *Dig. SID* 96:646
108. Broer DJ, Hikmet RAM, Challa G. 1989. *Makromol. Chem.* 190:3201
109. Schadt M. 1996. *Mol. Cryst. Liq. Cryst.* 292:235
110. Schiekel MF, Fahrenschon K. 1971. *Appl. Phys. Lett.* 19:391
111. White DL, Taylor GN. 1974. *J. Appl. Phys.* 45:4718
112. Clark NA, Lagerwall ST. 1980. *Appl. Phys. Lett.* 36:899
113. Bos PH, Koehler T. 1983. *Proc. Jpn. Dis.* p. 478
114. Doane JW, et al. 1986. *Appl. Phys. Lett.* 48:269
115. Ferguson JL. 1985. *SID* 16:88
116. Beresnev LA, Chigrinov VG, Dergachev V, Pozhidaev A, Fünfschilling J, Schadt M. 1988. *Liq. Cryst.* 5:1171
117. Chandani AD, Hagiwara T, Suzuki Y, Ouchi Y, Takezoe H, Fukuda A. 1988. *Jpn. J. Appl. Phys.* 27:L729
118. Barberi R, Boix R, Durand D. 1989. *Appl. Phys. Lett.* 55:2506
119. Fünfschilling J, Schadt M. 1990. *SID Dig.* p. 106
120. Patel JS. 1992. *Appl. Phys. Lett.* 60:280
121. Kiefer W, Weber G, Windscheidt M, Baur G. 1992. *Proc. IDRC* p. 547



CONTENTS

FUTURE DIRECTIONS IN CARBON SCIENCE, <i>M. S. Dresselhaus</i>	1
THE NEW GENERATION HIGH-TEMPERATURE SUPERCONDUCTORS, <i>Z. Fisk, J. L. Sarrao</i>	35
CERAMIC SCINTILLATORS, <i>C. Greskovich, S. Duclos</i>	69
CLAYS AND CLAY INTERCALATION COMPOUNDS: Properties and Physical Phenomena, <i>S. A. Solin</i>	89
BISTABLE CHOLESTERIC REFLECTIVE DISPLAYS: Materials and Drive Schemes, <i>Deng-Ke Yang, Xiao-Yang Huang, Yang-Ming Zhu</i>	117
BINDER REMOVAL FROM CERAMICS, <i>Jennifer A. Lewis</i>	147
CHARACTERIZATION OF POLYMER SURFACES WITH ATOMIC FORCE MICROSCOPY, <i>Sergei N. Magonov, Darrell H. Reneker</i>	175
ELECTRICAL CHARACTERIZATION OF THIN-FILM ELECTROLUMINESCENT DEVICES, <i>J. F. Wager, P. D. Keir</i>	223
LAYERED CERAMICS: Processing and Mechanical Behavior, <i>Helen M. Chan</i>	249
MATERIALS FOR FULL-COLOR ELECTROLUMINESCENT DISPLAYS, <i>Yoshimasa A. Ono</i>	283
LIQUID CRYSTAL MATERIALS AND LIQUID CRYSTAL DISPLAYS, <i>Martin Schadt</i>	305
CHEMICAL FORCE MICROSCOPY, <i>Aleksandr Noy, Dmitri V. Vezenov, Charles M. Lieber</i>	381
RECENT LIQUID CRYSTAL MATERIAL DEVELOPMENT FOR ACTIVE MATRIX DISPLAYS, <i>K. Tarumi, M. Bremer, T. Geelhaar</i>	423
CERAMICS IN RESTORATIVE AND PROSTHETIC DENTISTRY, <i>J. Robert Kelly</i>	443
LOCALIZED OPTICAL PHENOMENA AND THE CHARACTERIZATION OF MATERIALS INTERFACES, <i>Paul W. Bohn</i>	469
CERAMIC COMPOSITE INTERFACES: Properties and Design, <i>K. T. Faber</i>	499
AN ATOMISTIC VIEW OF Si(001) HOMOEPITAXY, <i>Zhenyu Zhang, Fang Wu, Max G. Lagally</i>	525
SUPERTWISTED NEMATIC (STN) LIQUID CRYSTAL DISPLAYS, <i>Terry Scheffer, Jürgen Nehring</i>	555
PHOTOREFRACTIVE POLYMERS, <i>W. E. Moerner, A. Grunnet- Jepsen, C. L. Thompson</i>	585
POLYCRYSTALLINE THIN FILM SOLAR CELLS: Present Status and Future Potential, <i>Robert W. Birkmire, Erten Eser</i>	625